

**Direct Galvanic Metallization of insulating Substrates:  
Mechanism and Applications for Microstructuring**

Inaugural - Dissertation  
zur  
Erlangung des Doktorgrades der  
Mathematischen-Naturwissenschaftlichen Fakultät  
der Heinrich-Heine-Universität Düsseldorf

**Thanh Tung Mai**

aus Hanoi

Düsseldorf 2003

Gedruckt mit Genehmigung der Mathematisch-Naturwissenschaftlichen Fakultät der Heinrich-Heine-Universität Düsseldorf

Erster Gutachter: Prof. Dr. J. W. Schultze  
Zweiter Gutachter: PD. Dr. G. Staikov  
Dritter Gutachter: Prof. Dr. K. Schierbaum

Tag der mündlichen Prüfung: 18.06.2003

***“Đi một ngày đàng, học một sàng khôn”***

(Tục ngữ Việt nam)



This work was performed at the Institute für Physikalische Chemie und Elektrochemie at the Heinrich-Heine-Universität Düsseldorf under the supervision of Prof. Dr. J.W. Schultze. Research of the PLATO technique is carried out in the frame of the project “Elektroschemische Mikro- und Nanosysteme”(ELMiNoS) of the state Nordrhein Westfalen (Germany), in cooperation with the company ENTHONE GmbH (Langenfeld). Research of the composite material phosphate/PEDT was supported by the Gottlieb-Daimler und Karl Benz Stiftung. Financial and technological supports of those organizations are acknowledged.

During the years that I have worked with this thesis, I have had the opportunity to work with a quite large number of people to whom I would like to express my deepest gratitude. I would also like to thank them not just for their work, but also for their support and company during my stay in Germany.

I am specially thankful to my supervisor Prof. Dr. J.W. Schultze for his guidance throughout my PhD study, his precious supports in difficult phases, for the freedom in working with many topics and methods as well as chances to publicize and present my works in scientific conferences.

I am also grateful to PD. Dr. G. Staikov for a lot of exciting discussions and motivations, and his acceptance to reference my work.

I appreciate my colleges C. Stromberg and A. Kurowski, not only for our together working and interesting scientific discussions, but also for their helpful supports at any time I need them, for the wonderful atmosphere, table tennis and café.

I would like to give my special thanks to Frau Hofmann, who always helped me kindly and remembered my birthdays, which I always forgot.

I would like to thank all institute members for the warm atmosphere, and for their helpful and joyful activities.

I want to thank my parents, my brothers and sisters for the remote support during my stay in Germany.

Last, but not least, I am grateful to my beloved wife, Ky, for all the love I have been privileged from you, your patience and understanding. You have been wonderful and I would not change you for anything.



## LIST OF PUBLICATIONS

?? **T.T. Mai, J.W. Schultze, G. Staikov**

*“Relation between Surface Preconditioning and Metal Deposition in Direct Galvanic Metallization of Insulating Surfaces“*

Solid State Electrochemistry, printed

?? **T.T. Mai, J.W. Schultze, G. Staikov**

*“Microstructured Metallization of insulating polymers “*

Electrochimica Acta, printed

?? **T.T. Mai, J.W. Schultze, G. Staikov**

*”Deposition Mechanism of Metals in Direct Galvanic Metallization of Insulating Substrates using metal sulphide”*

in preparation

and further publications

## ORAL PRESENTATIONS

?? **T.T. Mai, N. Müller und J.W. Schultze**

*„Influence of Electrolyte on the Formation of Phosphate Layer and Formation of Composite Phosphate-Conducting Polymers“*

INTERFINISH 2000, 13.-15. September 2000, Garmisch-Partenkirchen

?? **T.T. Mai, G. Staikov, J.W. Schultze**

*“Microstructuring and Metallization of insulating Polymers by PLATO-Technique”*

Joint Meeting of International Society of Electrochemistry (ISE) and The Electrochemical Society (ESC), 1.-9. September 2001, San Francisco (USA)

?? **T.T. Mai, G. Staikov, J.W. Schultze**

*“Application of PLATO-Technique for Microstructured Metallization of Polymers in Electronics”*

European Academy of Surface Technology Forum (EAST), 10.-13. October 2001, Chalkidiki (Greece)

## *Further presentations*

?? **T.T. Mai, J.W. Schultze, G. Staikov**

*“Mechanismus der Metallisierung von Kunststoffen nach dem PLATO-Verfahren”*

75. AGEF-Seminar Elektrochemische Oberflächen-, Mikro- und Nanotechnology, 6.Juni 2003, Fa. Enthone-OMI, Langenfeld

?? **T.T. Mai, J.W. Schultze, G. Staikov**

*“Direct metallization of insulating polymers using metal sulphide and applications for microstructuring”*

Oberflächentage 2003, 17. - 19. September 2003, Bremen

?? **T.T. Mai, J.W. Schultze, G. Staikov**

*“Direkt Metallisierung isolierender Kunststoffe mittels PLATO-Verfahren und Anwendung zur Mikrostrukturierung“*

Jahrestagung der Gesellschaft Deutscher Chemiker (GDCh), 6.-11. October 2003, München

## **POSTER PRESENTATIONS**

?? **T.T.Mai, J.W.Schultze**

*„ Composite Phosphate-Conducting Polymers for Corrosion Protection“*

EMT( Electrochemical Microsystem Technologies) 2000, 11.-13. September 2000, Garmisch-Partenkirchen

?? **T.T.Mai, G. Staikov, J.W. Schultze**

*„Metallisierung und Mikrostrukturierung insolierender Kunststoffe mittels PLATO-Verfahren“*

Jahrestagung der Gesellschaft Deutscher Chemiker (GDCh), 27.-29. September 2001, Würzburg

**(Prize for second best Poster)**

?? **T.T. Mai, G. Staikov, J.W. Schultze**

*“ Direct Metallization of Insulating Polymers by PLATO technique”*

53<sup>rd</sup> Annual Meeting of the International Society of Electrochemistry (ISE), 15.-20. September 2002, Düsseldorf

?? **T.T. Mai, A. Kurowski, J.W. Schultze, M.J. Schönning, H. Lüth**

*“Negative Mikrostrukturierung”*

70<sup>th</sup> AGEF Seminar, Düsseldorf, 26 April 2002



# CONTENTS

## PREFACE

<b>1. INTRODUCTION</b> .....	1
<b>2. BACKGROUND</b> .....	3
2.1. PLATO technique .....	3
2.2. Microstructured metallization of insulating substrates .....	13
<b>3. EXPERIMENTAL</b> .....	15
3.1. Materials and Chemicals .....	15
3.2. Methods .....	19
<b>4. MECHANISMS OF PRETREATMENT (ETCHING AND ACTIVATION)</b> .....	28
4.1. Etching .....	30
4.1.1. Roughness (AFM) .....	30
4.1.2. Surface groups (XPS) .....	35
4.1.3. Surface energy .....	41
4.2. Activation .....	43
4.2.1. Surface characterization .....	43
4.2.2. Influence of activation cycle on the coverage .....	46
<b>5. MECHANISMS OF METAL DEPOSITION</b> .....	49
5.1. Electrochemistry of cobalt sulphide .....	50
5.1.1. Electrochemistry of cobalt sulphide in Ni free solution .....	50
5.1.2. Electrochemistry of cobalt sulphide in Ni containing solution .....	57
5.2. Kinetics of metal deposition .....	58
5.2.1. Formation of Ni layer .....	58
5.2.2. Influence of potential, coverage and Ni concentration .....	72
5.3. Deposition mechanism .....	77
5.3.1. Formation of primary layer .....	77
5.3.2. Formation of secondary layer .....	79
<b>6. APPLICATIONS</b> .....	81
6.1. PLATO technique with different substrates and metals .....	81
6.2. Microstructured metallization .....	85
<b>7. CONCLUSIONS</b> .....	90
<b>8. APPENDICES</b> .....	93
<b>REFERENCES</b> .....	100



# 1. Introduction

Metallization of insulating polymers is of great importance for numerous applications in electronics and car industries. The most frequently used processes for metallization are physical vapor deposition (PVD), chemical vapor deposition (CVD) and electroless metal deposition. Due to the importance in industry, those processes were intensively studied and reviewed in a number of publications [Sach90][Bren63][Osul90]. Nevertheless, a lot of effort has been made to obtain a method to metallize modified insulating substrates by direct metal electrodeposition (direct galvanic metallization) [Urib93][Scha97]. The principle of this method is a formation of a non-metal layer (seed layer), so that metal deposition can be induced on this layer. The process of direct electrodeposition offers a number of advantages which apply to: simple control of metallization by current density and electrode potential, achievement of high deposition rates at relatively low operating temperatures, high selectivity and possibilities for metallization of surfaces and microstructures with complicated surface profiles.

Recently, modern methods for direct galvanic metallization are proposed using sulphide metals as the seed layer [Pily97][Vink98][Bur93]. Although the method was successfully applied, it is always carried out in a “black box” without understanding the mechanism of the process. Some important aspects of the methods found from empirical experiences: (i) suitable metals for these methods are some metals of Group IB (Cu, Ag), IVA (Sn, Pb), or Group VIII (Co, Ni); (ii) surfaces with higher amounts of the sulphide metal are easier to be metallized [Gul89][Bla90][Sche93][Burr93]. The PLATO technique (Möbius et. al.-ETHONE Germany), which will be focused in this work, is a method for direct metallization using cobalt sulphide as the seed layer [Möb00a][Möb00b][Möb00c]. From a technical point of view, the PLATO technique solves an important problem: it enhances the amount of metal sulphides by the use of oxygen-complexes, which strongly interact with the polymer surfaces.

Unlike metal electrodeposition on a metal substrate, direct metallization using metal sulphide has some interesting characteristics: overpotential  $\eta$  varies with position  $x$  and time  $t$  on the deposited layer during metal deposition; and the primary nucleation of the metal on the MeS layer is decided not only by  $\eta$ , but also by the number of MeS particles, which is in turn related to the properties of the polymer surface e.g. pre-treatment of the surface. Therefore, the system can be only understood when several factors and the relation among them are investigated, including: polymer surface, activation process and metal deposition.

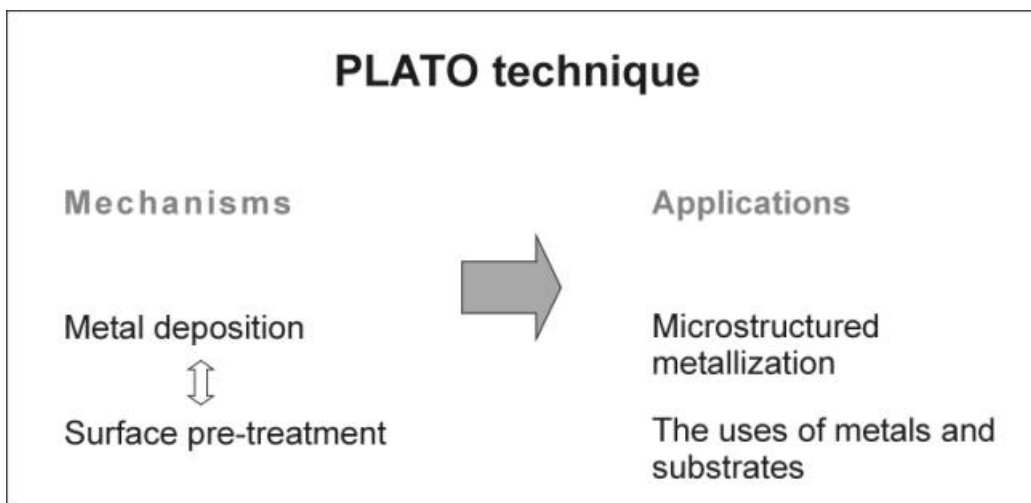
Goals of this work, which are summarized in Fig.1.1, consist of two parts:

**Study mechanisms of the processes**

- ?? Investigation the role of pre-treatment (etching and activation) and its influence to metal deposition;
- ?? Mechanisms of metal deposition on metal sulphide, with the representative system: Ni on cobalt sulphide.

**Applications**

- ?? Application of the method for microstructured metallization of insulating substrates;
- ?? Reviewing some applications of the technique for different insulating substrates and metals (alloys).



**Figure 1.1** Schematic description for the structure and the goals of this work.

## 2. Background

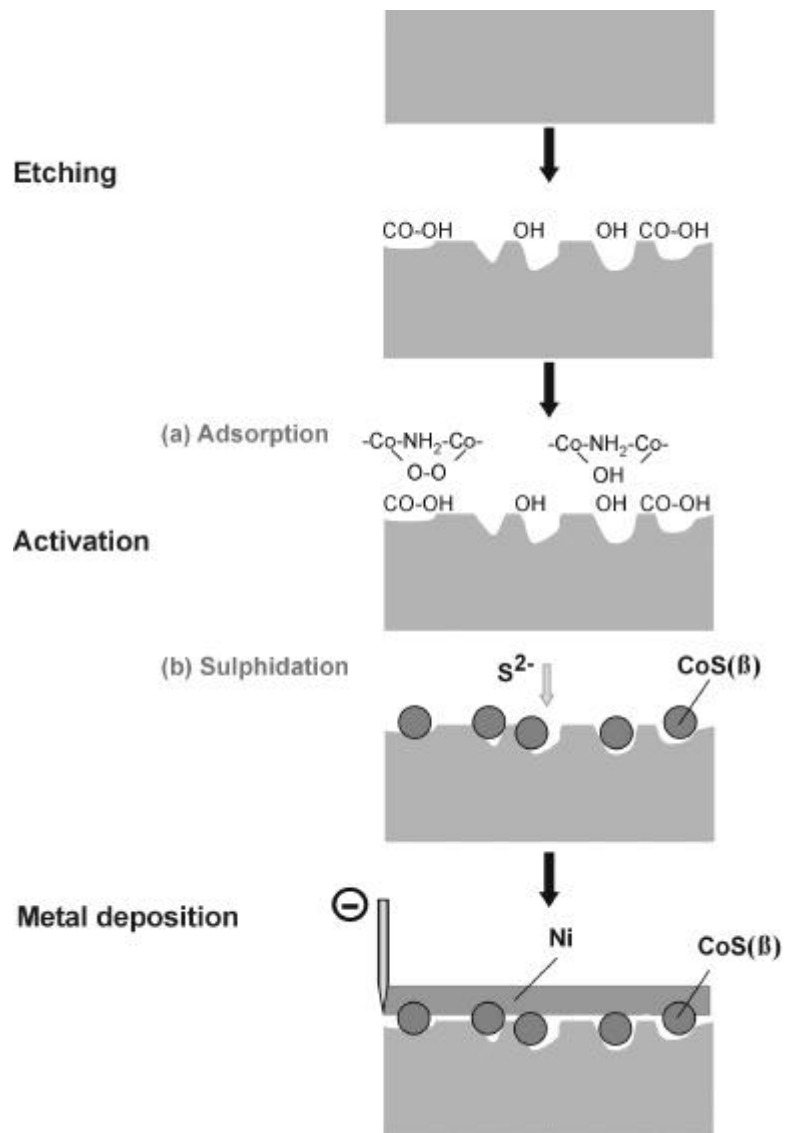
### 2.1. PLATO technique

The PLATO technique for direct galvanic metallization of polymers is schematically described in Fig. 2.1. In principle, the process consists of three steps:

?? Surface treatment: etching in strong oxidation media e.g.  $\text{CrO}_3/\text{H}_2\text{SO}_4$

?? Activation: formation of a cobalt sulphide layer. The activation process consists of 2 steps: (a) adsorption of cobalt-oxygen-complex and (b) sulphidation.

?? Metal deposition (galvanic direct metallization on the seed layer)



**Figure 2.1** Schematic description of the PLATO technique.

### 2.1.1. Surface treatment

Surface treatment is an important step, which influences the activation process and the adhesion of the metal layer. Frequently applied techniques for surface treatment are: chemical etching, plasma or excimer laser [Chan92]. In this work, the surface treatment is a chemical etching process in a standard etching solution  $\text{CrO}_3/\text{H}_2\text{SO}_4$  ( $65^\circ\text{C}$ ). Generally, modification of polymer surfaces is characterized by the possible change of the roughness, the surface group and the surface energy.

#### *Roughness*

The surface treatment usually leads to an increase of roughness. Correlation between roughness and adhesion between metal layers on substrates was investigated in several works using techniques which allow producing roughness precisely (excimer laser), combined with exact adhesion measurements. Generally, a higher roughness of the polymer surface results in a better adhesion of the metal layer after metallization [Mann93][Mey93][Schro95].

In the PLATO technique, the roughness is also related to the adsorption of the cobalt-complex. After the chemical etching, the roughness obtained corresponds to the formation of pores on the polymer surface. The sum-volume of pores decides the volume of cobalt-complex solution filled in them, which is in turn proportional to the amount of cobalt sulphide. The critical pore radius, which allows liquid to fill the pores, is described by the Washburn's equation [Wash31]:

$$r_{crit} = \frac{2d \cdot \cos \alpha}{p} \quad (2.1)$$

Where  $\gamma$  is the surface tension,  $p$  is the pressure. For aqueous solutions ( $\gamma = 72.8 \cdot 10^{-3} \text{ N/m}$ ), atmosphere pressure ( $p_{atm} = 10^5 \text{ N/m}^2$ ), the critical pore radius is  $0.5\text{-}0.7 \mu\text{m}$ , which is smaller than the size of most pores on pretreated polymer surfaces.

Thus, a large number of pores can be filled by the cobalt-complex solution during the adsorption process and the amount of adsorbed solution is decided by sum volume of pores. Bearing in mind that this cobalt-complex will be converted to cobalt sulphide after sulphidation, we consider roughness as an important factor influencing the activation process.

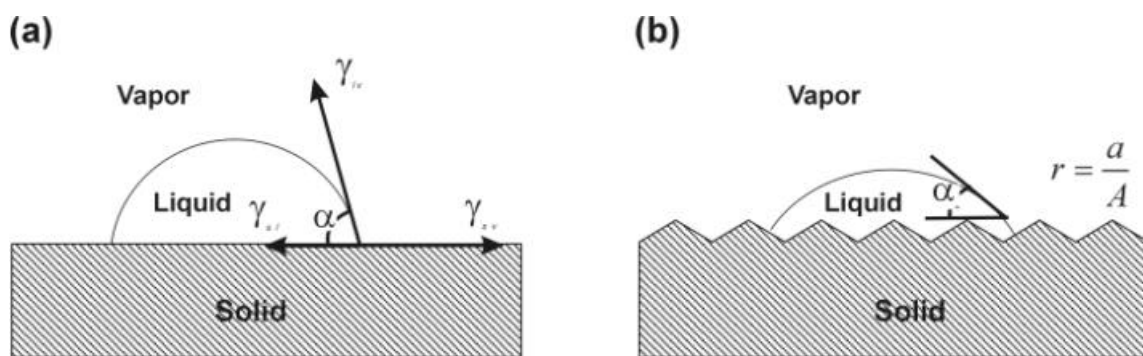
*Surface groups*

Depending on the nature of the polymers and the modification method (chemical, laser, plasma), the surface groups after pretreatment can be different.

*Surface energy*

Other important parameters characterizing the modification of surfaces are the contact angle and the corresponding surface energy. The contact angle on polymers is typically influenced by following factors:

- (i) Roughness of the surfaces;
- (ii) Nature of the polymer e.g. hydrophilic group of the polymer, crystallinity, surface phases;
- (iii) Measurement conditions: liquid used (water, ethanol..), temperature, atmosphere (air, saturated vapour) and drop size.



**Figure 2.2** (a) Equilibrium contact angle.  
 (b) Influence of the roughness on the equilibrium contact angle.

The contact angle at equilibrium, as shown in Fig. 2.2, is governed by the force balance at the three – phase boundary and is defined by Young’s equation [Chan92]:

$$\gamma_{lv} \cos \alpha = \gamma_{sv} - \gamma_{sl} \tag{2.2}$$

where  $\gamma_{lv}$  is the surface tension of the liquid in equilibrium with its saturated vapor,  $\gamma_{sv}$  is the surface tension of the solid in equilibrium with the saturated vapor of the liquid, and  $\gamma_{sl}$  is the interfacial tension between the solid and the liquid. This equation is valid only for smooth surfaces with roughness below 0.1-0.5  $\mu\text{m}$ .

For the rough solid surface, the contact angle is also dependent on the roughness and this relation can be described by the Wenzel's equation [Chan92][Veer97]

$$\cos \alpha' = r \cos \alpha \quad (2.3)$$

where  $\alpha$  is the intrinsic (equilibrium) contact angle,  $r$  is the roughness factor, which is the roughness ratio ( $r = \frac{a}{A} = \frac{da}{dA} \geq 1$ ),  $\alpha'$  is the apparent contact angle (measured through a microscope),  $a$  is the actual area of the surface,  $A$  is the apparent area, or geometrical area of the surface.

For the system: water drop (l), water vapor (v) and solid (s), the surface energy  $\gamma$  (or the surface tension  $\gamma_{sl}$ ) can be determined through the Young-Dupre equation [Duca98]:

$$\gamma = \gamma_{sl} + \frac{\gamma_w}{4} (1 - \cos \alpha_a)^2 \quad (2.4)$$

where  $\gamma_w = 73 \text{ mJ/m}^2$  is the surface energy of liquid water.

### 2.1.2. Activation

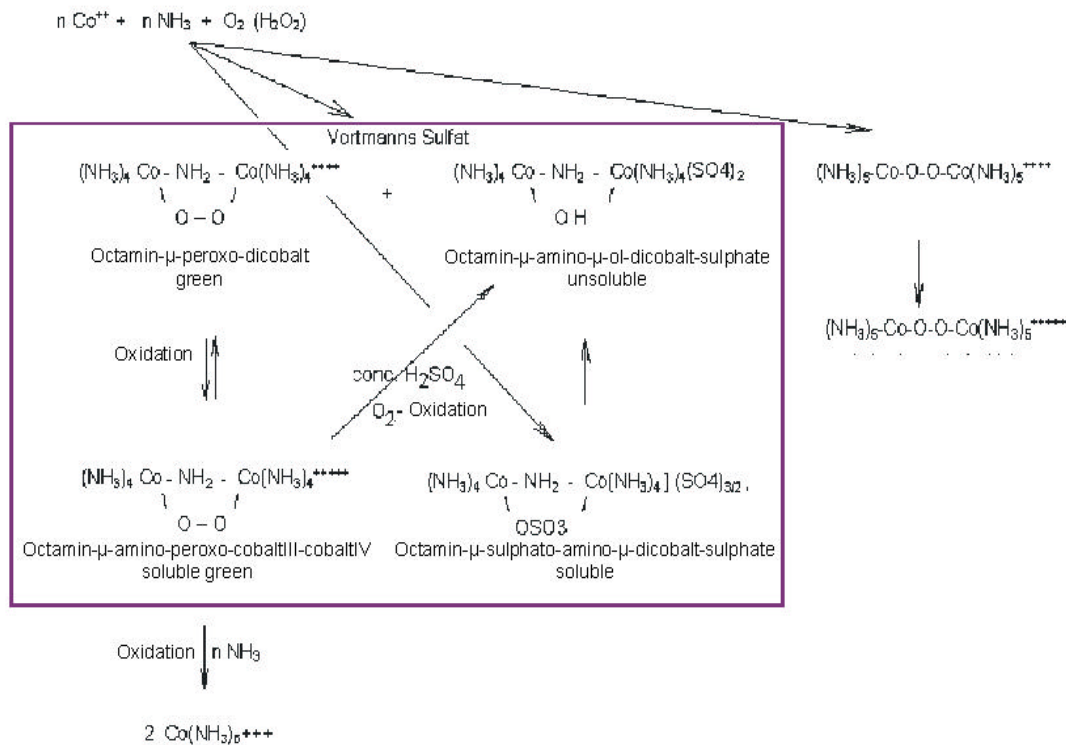
The activation process consists of two steps:

- (a) "Adsorption" of the cobalt-complex  $\text{Co[Lig]}_x$ ;
- (b) Sulphidation through a reaction between  $\text{Co[Lig]}_x$  and the sulphide cation  $\text{S}^{2-}$ .

The "adsorption" of the cobalt-complex  $\text{Co[Lig]}_x$  here is understood as a localization of the cobalt-complex solution on the polymer surface. The amount of "adsorbed" cobalt-complex on the surface is influenced by:

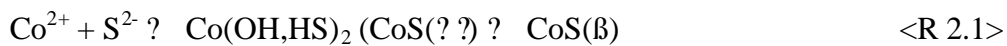
- ?? the roughness  $r$  of the surface (or the sum volume of pores - see 2.1.1).
- ?? the physical adsorption (physisorption enthalpy  $< 20 \text{ kJ/mol}$ ) of the cobalt-complex on the polymer. In order to enhance the physical adsorption, cobalt-oxygen-complexes with (–O–O–) or (–O–H) groups are produced, since those complexes may show higher interactions with polymer surfaces, which typically carry –COOH and –COH groups. The cobalt-oxygen-complexes are formed by bubbling oxygen in the  $\text{Co}(\text{NH}_3)_4^{2+}$  solution. However, the oxidation of the cobalt-complex is a complex process and products are a mixture of different cobalt-oxy-complexes (–Co–O–O–Co– or Co–OH–Co–) [Syke69][Davi98]. The possible products with different oxidation degree are shown in Fig. 2.3 [Fuhr00].



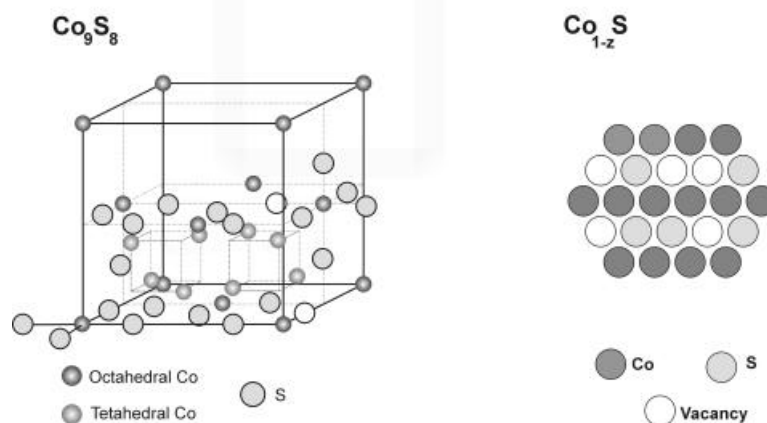


**Figure 2.3** Schema illustrating possible products of cobalt-oxygen-complex depending on the oxidation grade as oxygen reacts with  $\text{Co}(\text{NH}_3)_4^{2+}$  [Fuhr00].

The sulphidation is carried out by dipping the polymer surface with the adsorbed cobalt-oxygen-complexes in a solution containing  $\text{S}^{2-}$ . The reaction that takes place is:



$\text{CoS}(\text{? ?})$  exists only in aqueous media and it converts quickly to  $\text{CoS}(\beta)$  in the atmosphere. Thus, the product formed on the polymers after the activation process is  $\text{CoS}(\beta)$ , which is a mixture of  $\text{Co}_9\text{S}_8$  and  $\text{CoS}_{1-z}$  (~70% wt.  $\text{CoS}_{1-z}$ ) [Nick68]. The solubility product of  $\text{CoS}(\beta)$  is  $K_{sp} = -25$ . The crystal structures of  $\text{Co}_9\text{S}_8$  and  $\text{CoS}_{1-z}$  are shown in Fig. 2.4.



**Figure 2.4** Structures of  $\text{Co}_9\text{S}_8$  (eight of Co atom occupy tetrahedral holes and the ninth S atom is octahedrally surrounded) and  $\text{Co}_{1-z}\text{S}$  (closed packed, vacancies are occupied by S atoms. The structure shown in the figure has  $z=0.5$ ) [Nick68].

### 2.1.3. Metal electrodeposition

The process metal electrodeposition in galvanic direct galvanic metallization of insulating substrates has all characteristics of conventional metal electrodeposition on a conducting substrates. However, an important specific feature of the metal deposition on a low conductivity substrate is the uneven potential distribution due to the potential drop on the substrate. In the following, fundamentals of metal electrodeposition and the potential distribution on a low conductivity substrate will be shortly reviewed.

#### 2.1.3.1. Thermodynamics and kinetic aspects

The overall reaction describing the metal deposition or dissolution of a bulk metal Me can be expressed by equation



where  $\text{Me}_{\text{sol}}^{z+}$  are solvated metal ions in the electrolyte phase and Me is a metal in the bulk phase. The Nernst equilibrium potential  $E_{\text{Me}/\text{Me}^{z+}}$  of the Me/Me<sup>z+</sup> metal ion electrode is given by:

$$E_{\text{Me}/\text{Me}^{z+}} = E_{\text{Me}/\text{Me}^{z+}}^{\circ} + \frac{RT}{zF} \ln \frac{a_{\text{Me}^{z+}}}{a_{\text{Me}}} \quad (\text{Nernst's equation}) \quad (2.5)$$

in which  $E_{\text{Me}/\text{Me}^{z+}}^{\circ}$  denotes the standard potential of the Me/Me<sup>z+</sup>,  $a_{\text{Me}^{z+}}$  is the activity of  $\text{Me}_{\text{sol}}^{z+}$  ions in the electrolyte (for a pure 3D Me bulk phase,  $a_{\text{Me}}$  is equal to unity).

At the Nernst potential  $E_{\text{Me}/\text{Me}^{z+}}$ , the electrochemical reaction (R 2.2) is in equilibrium and  $\tilde{\mu}_{\text{Me}^{z+}}^{(\text{El})} = \tilde{\mu}_{\text{Me}^{z+}}^{(\text{Me})}$  ( $\tilde{\mu}_{\text{Me}^{z+}}^{(\text{El})}$  and  $\tilde{\mu}_{\text{Me}^{z+}}^{(\text{Me})}$  are the electrochemical potentials of the metal ions in the electrolyte and in the bulk phase). The deviation from equilibrium  $\eta = \tilde{\mu} - \tilde{\mu}_{\text{Me}^{z+}}^{(\text{El})} = \tilde{\mu}_{\text{Me}^{z+}}^{(\text{Me})} - \tilde{\mu}_{\text{Me}^{z+}}^{(\text{El})}$  is related to the actual electrode potential  $E$  by:

$$\eta = \tilde{\mu} - \tilde{\mu}_{\text{Me}^{z+}}^{(\text{El})} = zF(E - E_{\text{Me}/\text{Me}^{z+}}) \quad (2.6)$$

where  $\eta = E - E_{\text{Me}/\text{Me}^{z+}}$  is the overpotential. Generally, the electrodeposition process includes various rate determining steps such as the electrocrystallization ( $\eta_{\text{crys}}$ ), charge transfer ( $\eta_{\text{ct}}$ ), diffusion ( $\eta_{\text{d}}$ ) and chemical reactions ( $\eta_{\text{chem}}$ ). The total overpotential  $\eta$  can be expressed by equation:

$$\eta = \eta_{\text{crys}} + \eta_{\text{ct}} + \eta_{\text{d}} + \eta_{\text{chem}} \quad (2.7)$$

where  $\eta_{crys}$ ,  $\eta_{ct}$ ,  $\eta_d$ ,  $\eta_{chem}$  are electrocrystallization, charge transfer, diffusion and chemical reactions overpotentials, respectively.

If the kinetics of metal deposition and dissolution are not controlled by charge transfer, ion diffusion and migration or additional chemical reaction steps ( $\eta_{ct}$ ,  $\eta_d$ ,  $\eta_{chem}$  is low), the overpotential represents the crystallization overpotential ( $\eta_{crys}$ ). Thus:

$$\eta_{crys} = E - E_{Me/Me^{z+}} - \frac{RT}{zF} \ln \frac{a_{Me_{ads}}}{a_{0,Me_{ads}}} \quad (2.8)$$

where  $a_{Me_{ads}}$  and  $a_{0,Me_{ads}}$  denote the activities of  $Me_{ads}$  at  $E = E_{Me/Me^{z+}}$  and  $E = E_{Me/Me^{z+}}$ , respectively.

### 2.1.3.2. Deposition mechanisms

#### *Interaction between deposited metal and substrate*

For electrodeposition of a metal on a foreign substrate, electrocrystallization can occur at  $\eta_{\tilde{\mu}} < 0$  and  $\eta < 0$  (overpotential deposition) and  $\eta_{\tilde{\mu}} > 0$  and  $\eta > 0$  (underpotential deposition). The parameter determining if overpotential deposition (OPD) or underpotential deposition (UPD) can take place is the interaction between deposited metal and substrate. Two growth modes can be distinguished [Bud96]:

- (I) In systems with weak deposit-substrate interaction (weak adhesion) the metal deposition starts at supersaturations ( $\eta_{\tilde{\mu}} > 0$ ) in the overpotential deposition (OPD) range  $E = E_{Me/Me^{z+}}$  following a 3D island growth mode (Volmer-Weber growth mode).
- (II) In the case of a strong deposit-substrate interaction (strong adhesion), the metal deposition can start even at undersaturations ( $\eta_{\tilde{\mu}} < 0$ ) in the underpotential deposition (UPD) range  $E = E_{Me/Me^{z+}}$ . Depending on the deposit-substrate lattice misfit, the deposition at low overpotentials usually follows a Frank-van der Merwe growth mode (layer-by-layer growth mode) or a Stranski-Krastanov growth mode (3D Me island formation and growth on top of predeposited 2D Me overlayers)

*Nucleation and growth of metals*

In case overpotential deposition takes place, the driving force for electrocrystallization is the overpotential  $\eta$ , or in general, the supersaturation  $\ln \tilde{\mu}$  (equation (2.8)). The phase formation of a metal from the electrolyte during metal deposition consists of two processes: nucleation and growth of the metal.

In the nucleation process, stable metal clusters are formed. These clusters are called nuclei and the sizes of the nuclei are described by the number of metal atoms in a cluster  $N$ . At a supersaturation  $\ln \tilde{\mu} > 0$ , clusters exist as a result of thermal fluctuations in the sense of statistical thermodynamics. However, only the clusters with the size  $N > N_{crit}$  are stable and continue to grow. The critical size  $N_{crit}$  is a function of the supersaturation and can be expressed by equation:

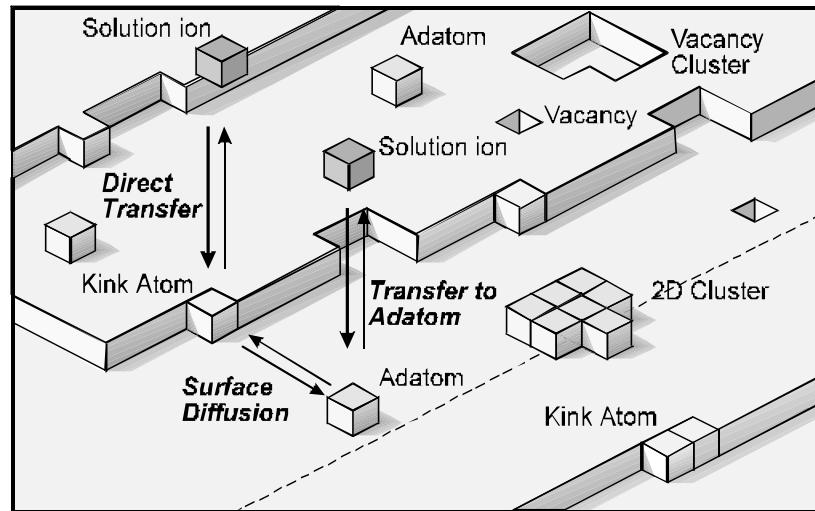
$$N_{crit} \approx \frac{8BN_A V_m^2 \sigma^3}{27(\ln \tilde{\mu})^3} \quad (2.9)$$

where  $\sigma_i$  are the specific surface energies of the crystal faces,  $V_m$  is the molar volume of the condensed new phase and  $B$  is a factor depending on the geometrical form of the nucleus. The rate of nucleation is defined by the net flux  $J$  of clusters through the critical size of the nucleus. The dependence of the nucleation rate on supersaturation  $\ln \tilde{\mu}$  can be described by equation:

$$\frac{d \ln J}{d \ln \tilde{\mu}} \approx \frac{N_{crit}}{RT} \quad (2.10)$$

Thus, with a higher the supersaturation  $\ln \tilde{\mu}$ , nucleation will occur with a higher rate and smaller size of nuclei is obtained.

The growth rate of a crystal depends on its size, degree of perfection and surface structure. On metal substrates, the incorporation of monomer particles in the crystal lattice occurs at the so-called “kink positions” (half crystal positions) on monoatomic steps. Two mechanisms of incorporation are generally possible: (I) a mechanism of direct incorporation (direct transfer from the ambient phase to a kink) and (II) a surface diffusion mechanism, i.e. formation of adatoms (adsorbed monomer particles) followed by surface diffusion to the steps (Fig. 2.5).



**Figure 2.5** Model of electrocrystallization: (I) direct transfer mechanism and (II) adatom and surface deposition mechanism [Bud96].

Based on the fundamental theories of metal phase formation, the theories of nucleation and growth for metal deposition on metal substrates have been intensively studied. Because of the limitation of the thesis, the theories of metal deposition will not be described in details. The contents of those theories can be found in references [Bud96][Stai02][Harr92].

In technical metal deposition with typical current density  $|i| > 10 \text{ mA/cm}^2$ , kinetics are controlled by charge transfer and  $i_{ct}$ . Therefore current density is given by the Butler-Volmer equation:

$$i = i_{ct} = i_0 \exp\left(\frac{\alpha_a F}{RT} \eta\right) - \frac{c_s}{c_b} \exp\left(-\frac{\alpha_c F}{RT} \eta\right) \quad (2.11)$$

where  $i_0$  is the exchange current,  $\alpha_a$  and  $\alpha_c$  are anodic and cathodic charge transfer coefficients,  $F$  is the Faraday constant (96500 C/mol),  $R$  is gas constant (8.314 J/K.mol) and  $T$  is the absolute temperature.

In the case of metal electrodeposition on an insulating substrate presented in this work, nucleation involves deposition on activated particles. Nucleation and growth are not only influenced by supersaturation (overpotential), but they are also related to electrochemical processes occurring during deposition.

### 2.1.3.3. Potential distribution on a low conductivity substrate

Modelling of potential distribution on low conductivity substrates has been introduced in several studies of Alkire and Landolt [Alk73][Land90][Matl99]. Fig. 2.6 shows a physical model, in which a seed metal layer A (thickness  $a$ , conductivity  $\sigma_a$ ) is pre-formed on an insulating polymer and metal B (conductivity  $\sigma_b$ , thickness  $b(x,t)$  varying with position  $x$  and time  $t$ ) is deposited on the layer A. The conductivity of the metal layer  $s(x,t)$ , which consists of the conductivity of the seed layer (A) and the conductivity of the deposited metal (B), is:

$$s(x,t) = a\sigma_a + b(x,t)\sigma_b \quad (2.12)$$

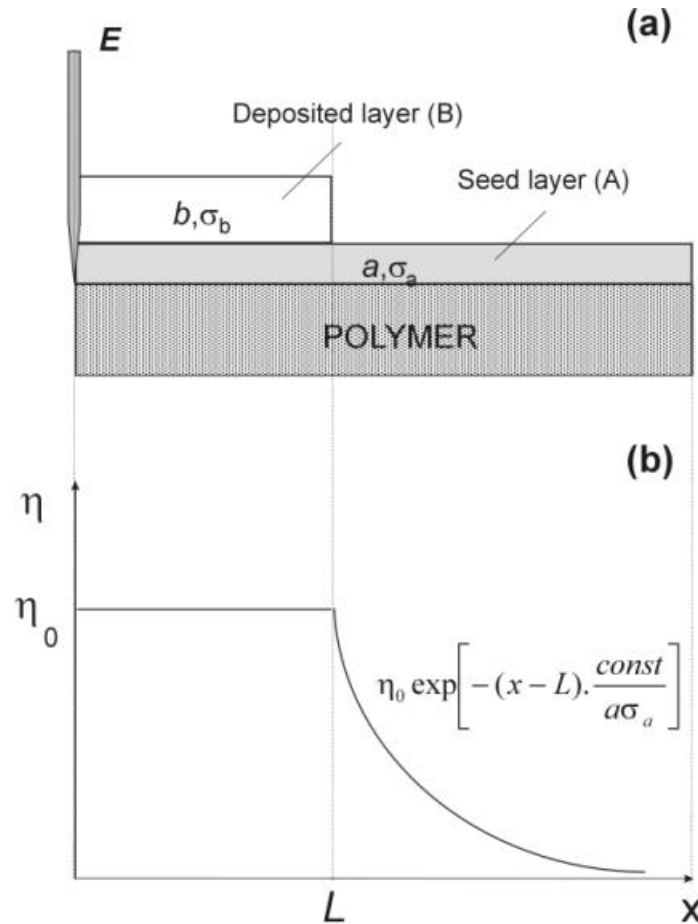
The general equation for potential distribution on the metal phase is:

$$a s(x,t) \frac{d^2 \phi}{dx^2} = i_o \exp\left(\frac{\phi}{RT}\right) - \frac{c_s(x,t)}{c_b} \exp\left(-\frac{\phi}{RT}\right) \quad (2.13)$$

In order to solve the equation (2.12), numerical methods must be applied. However, an algebraic formula of the equation can be obtained with several crude simplifications: (i) The conductivity on the already deposited metal B is high so that the potential drop on this layer are neglected (ii) linearization of the Butler-Volmer equation. The equation in these conditions at an arbitrary time  $t$  is [deLe94]:

$$\phi(x) = \begin{cases} \phi_0 & \text{If } x < L \\ \phi_0 \exp\left(-\frac{(x-L) \cdot \text{const}}{a\sigma_a}\right) & \text{If } x > L \end{cases} \quad (2.14)$$

With  $L(t)$  is the length of the deposited metal layer (B) (Fig 2.6)



**Figure 2.6** Schematic drawing of the metallization process (a) and the corresponding overpotential distribution as a function of  $x$  at an arbitrary time  $t$  (b).

## 2.2. Microstructured metallization of insulating substrates

The PLATO technique is proposed in this work as a method for producing a microsystem Metal/Insulator (M/I) and metal/Insulator/semiconductor (M/I/S). In principle, the technique allows producing different types of M/I and M/I/S microstructures e.g. statistic, irregular, periodic or single (classification by order); 0-dimension, 1-dimension, 2-dimension (classification by symmetry); positive, negative, flat (classification by aspect ratio) (microstructure classification by Schultze [Schu01]).

Generally, microstructured metallization can be carried out following two concepts: pre-structuring and post-structuring [Schu99][Schu01]. Pre-structuring mentions the processes where the final step metal deposition forms metal microstructures. Post-structuring denotes processes, where metal is deposited overall, following by the microstructuring step. Thus, in

pre-structuring concepts, the microstructuring is related to selective modification of polymer or localization of activation. Meanwhile, microstructuring in post-structuring is carried out by microetching of the metal.

Technical possibilities corresponding to pre- and post-structuring are summarized as follows:

Pre-structuring:

Selective modification of polymers:

?? Laser (continuous wave, excimer);

?? Chemical etching, plasma using masks;

Localization of the activation:

?? Masks (photoresist, movable mask);

Post-structuring (metal etching):

?? Chemical etching using mask;

?? Excimer laser.



### 3. Experimental

#### 3.1. Materials and Chemicals

##### 3.1.1. Polymer substrates

Different substrates were used in this work in order to study the influence of the nature of the polymer on the process: ABS (Acrylonitrile-Butadiene-Styrene), PC (Polycarbonate), ABS/PC (blend polymer of ABS and PC), PEEK (Poly-Ether-Ether-Ketone), PI (Polyimide). Formulas and technical informations of the polymers are listed in table 3.1.

##### 3.1.2. Process

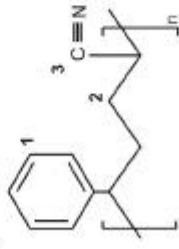

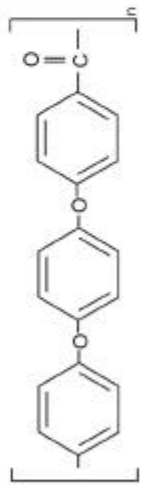
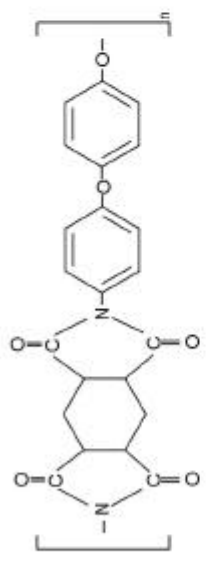
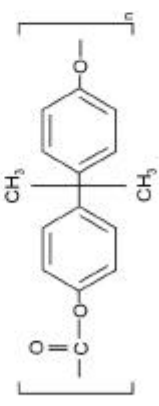
Process Step Parameter	Surface treatment				Activation			Metal deposition
	Etching (CrO <sub>3</sub> /H <sub>2</sub> SO <sub>4</sub> )	Rinsing	Cr <sup>6+</sup> reduction	Rinsing	Co-complex Adsorption	Sulphidation	Rinsing	
T/°C	60-65							45
		25	25	25	25	25		
pH			8		10	9		4
	<0	7		7			7	

**Figure 3.1** Process diagram of the PLATO technique.

Fig. 3.1 shows the process diagram of the PLATO technique with process steps and corresponding pH and temperature values.

Etching is carried out at 65°C in a solution containing 400g/l CrO<sub>3</sub>, 400g/l H<sub>2</sub>SO<sub>4</sub>. Etching time varies from 5-10 min. After etching, the polymer surface is rinsed carefully with distilled water in order to remove Cr<sup>6+</sup> and oxidation products from the etching reactions.

**Table 3.1** Formulas, phase compositions, technical description of the polymer substrates

<b>Polymers</b>	<b>Formula</b>	<b>Phase composition</b>	<b>Technical description</b>	<b>Company</b>
<b>ABS</b> (Acrylonitrile-Butadiene-Styrene)	<p>Styrene Acrylonitrile (SAN)</p>  <p>Polybutadiene (PB)</p> 	two phases (SAN and PB)	<ul style="list-style-type: none"> <li>➤ Good mechanical property</li> <li>➤ Material for car and electrical industry</li> </ul>	<i>Good Fellow</i>
<b>PEEK</b> (Poly-Ether-Ether-Ketone)		semi-crystalline phase	<ul style="list-style-type: none"> <li>➤ High-T Performance</li> <li>➤ Strength &amp; Toughness</li> <li>➤ Wear Resistant</li> <li>➤ Materials for Microtechnology</li> </ul>	<i>Victrix</i>
<b>PI</b> (Polyimide) ( <i>Kapton™</i> )		amorphous phase	<ul style="list-style-type: none"> <li>➤ High-T Performance (high melting point)</li> <li>➤ High dielectric constant <math>\epsilon</math></li> <li>➤ Materials for microtechnology</li> <li>➤ Materials for electronics</li> </ul>	<i>Du Pont</i>
<b>PC</b> (Polycarbonate) ( <i>Makrolon™</i> )		amorphous phase	<ul style="list-style-type: none"> <li>➤ Material for Microtechnology</li> </ul>	<i>Fa. Röhm</i>
<b>ABS/PC 45</b> (Blend co-polymer)	Blend co-polymer of ABS and PC (45% mass of PC)	two phases (SAN/PC and PB)	<ul style="list-style-type: none"> <li>➤ Easy processing</li> <li>➤ Material for car and electrical industry</li> </ul>	<i>Bayer</i>

Activation includes 2 steps: (a) adsorption of the cobalt-complex on the surface and (b) sulphidation (section 2.2). The cobalt-complex solution (*Aktivierung<sup>mm</sup>-Enthone*) is prepared from 0.1M CoSO<sub>4</sub>·7H<sub>2</sub>O, NH<sub>3</sub> and an oxidizer (H<sub>2</sub>O<sub>2</sub>). The solution is bubbled with an air flow 15-30 minutes before use in order to produce oxygen-complexes. The sulphidation solution used is *Vernetzung<sup>mm</sup>-Enthone*, which contains 0.05M Na<sub>2</sub>S. Activation is carried out by dipping samples in the cobalt-complex solution and subsequently in the sulphidation solution. The sulphidation reaction can be followed optically, since the formation of cobalt sulphide changes the surface from its original colour to dark brown one. After activation, the polymer surface is rinsed carefully with a flow of distilled water.

Metal deposition is carried out in different electrolytes. Solutions and anode materials for metal deposition, and chemicals used to make solutions are listed in table 3.2. Solutions for Ni, Co and Ni-Co alloy deposition were of the type: Watt's bath, containing sulphate and chloride of the metals [LPW88][DiBari00]. The Ni-P deposition solution is a Brenner's bath with the composition shown in table 3.2 [Bren63].

**Table 3.2** Composition of the electrodeposition baths

<b>Bath</b>	<b>Composition</b>			
Ni-deposition (Watt's bath)	<i>Ni solution</i>	NiSO <sub>4</sub> ·6H <sub>2</sub> O	0.9M	p.a.99% Aldrich
	(T=45°C, pH=4)	NiCl <sub>2</sub> ·6H <sub>2</sub> O	0.1M	p.a.98% Merck
		H <sub>3</sub> BO <sub>3</sub>	30g/l	
	<i>Anode</i>	Ni metal		99.9% Good Fellows
Co-deposition (Watt's bath)	<i>Co solution</i>	CoSO <sub>4</sub> ·7H <sub>2</sub> O	0.9M	
	(T=45°C, pH=4)	CoCl <sub>2</sub> ·6H <sub>2</sub> O	0.1M	
		H <sub>3</sub> BO <sub>3</sub>	30g/l	
	<i>Anode</i>	Co metal		99.9% Good Fellows

**Table 3.2 (cont.)** Composition of the electrodeposition baths

<b>Bath</b>	<b>Composition</b>			
Co-Ni deposition (Watt's bath)	<i>Co Ni solution</i> (T=45°C, pH=4)	NiSO <sub>4</sub> ·6H <sub>2</sub> O	0.9M	
		NiCl <sub>2</sub> ·6H <sub>2</sub> O	0.1M	
		CoSO <sub>4</sub> ·7H <sub>2</sub> O	0.1M	
		H <sub>3</sub> BO <sub>3</sub>		p.a. 99.8% Merck
	<i>Anode</i>	Ni metal		99.9% Good Fellows
Ni-P deposition (Brenner's bath)	<i>NiP solution</i> (T=50°C, pH=1.8)	NiSO <sub>4</sub> ·6H <sub>2</sub> O	150g/l	p.a.99% Aldrich
		NiCl <sub>2</sub> ·6H <sub>2</sub> O	45g/l	p.a.98% Merck
		NiCO <sub>3</sub>	40g/l	
		H <sub>3</sub> PO <sub>4</sub>	50g/l	
		H <sub>3</sub> PO <sub>3</sub>	50g/l	
	<i>Anode</i>	Ni metal		99.9% Good Fellows

## 3.2. Methods

A combination of different methods was used in order to study the PLATO technique. The informations required and the analytical methods are summarized in table 3.3.

**Table 3.3** Informations required and analytical methods

<b>Polymer surface</b>	<b>Activation</b>	<b>Metal deposition</b>
??Surface morphology of polymers (SEM, AFM)	??Chemical bindings (XPS)	??Deposition mechanisms (electrochemical methods, AFM, cross section)
??Chemical bindings (XPS)	??Electrochemistry of CoS( $\beta$ ) (CV, potentiostatic)	
??Surface energy (contact angle measurement)		??Microstructuring (AFM, laser profilometer)

### 3.2.1. Electrochemical methods

#### 3.2.1.1. Instruments

For the electrochemical measurements, home-built potentiostats (Martin Schramm) were used. The main components of the potentiostats are:

?? Potentiostat	Rising time ? $10^6$ V/s, Output current 1 A Potential ? 10 V
?? Triangle generator	adjustable scanning rate
?? Pulse generator	Rising time ? $10^6$ V/s
?? Logarithmic timer	Band width $10^{-3}$ Hz – $10^6$ Hz
?? Current measurement	Measurement resistance 5 ? - 30,5 G? , automatic adjust (switching time ? 1 $\mu$ s), external switcher 50 Hz-Filter
?? Lock-In Amplifier	HMS-Elektronik/ Dynatrac 502

Electrochemical methods used in this work were

?? Cyclic Voltammetry (CV)

?? Potentiostatic

The obtained data were acquired by a home-built software developed by Thies (1988).

Analysis of the data was carried out by the software Microcal Origin™.

### 3.2.1.2. Electrochemical cell

#### *Potentiostatic metallization*

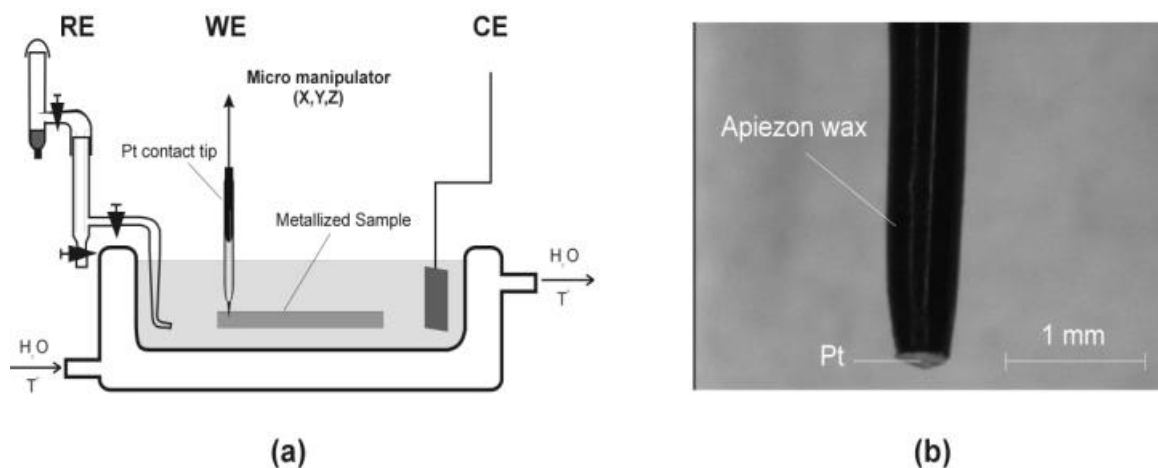
The electrochemical cell for the potentiostatic metallization and current transient measurements consists of (Fig. 3.2):

?? Working electrodes (WE): the working electrode is a system consisting of a Pt contact tip and a metallized sample. When a certain potential is applied on the contact tip, the metal deposition is first induced at the contact-tip and then the metal layer propagates on the surface of the sample. In order to exclude the current signal from the contact tip and obtain only the signals of the metal deposition, the contact tip is shielded by Apiezon-wax so that only the tip area is exposed (Fig. 3.2b). The contact tip is fixed on a micromanipulator and can be positioned exactly.

?? Counter electrode (CE): depending on the deposition process (Ni deposition, Co deposition etc.), the materials used are: Au (Good Fellows 99.9%, ) Ni-metal (Good Fellows 99.5%), Co-metal (Good Fellows 99.5%)

?? Reference electrode (RE): Hg/Hg<sub>2</sub>SO<sub>4</sub>/Na<sub>2</sub>SO<sub>4</sub> ( $E = 0.68\text{V vs SHE}$ )

WE, RE and CE were connected to the potentiostat (described in 3.2.1.1) in order to control the potential and record the current transients.



**Figure 3.2** (a) Electrochemical cell for electrodeposition (b) Pt contact tip

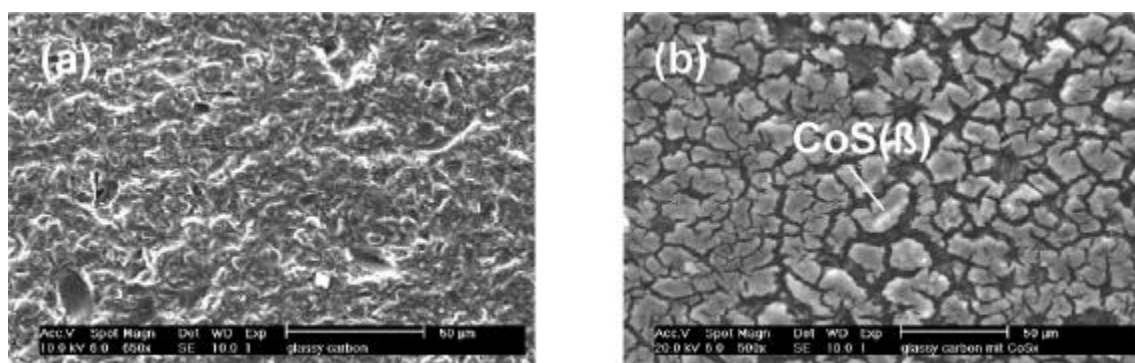
### Characterization of $\text{CoS}(\beta)$

The cell used for characterization of the  $\text{CoS}(\beta)$  includes:

?? Working electrode:  $\text{CoS}(\beta)$  adsorbed on glassy carbon (GC/ $\text{CoS}(\beta)$  electrode). The major part of electrode surface is covered with isolating plastic so that only a bare circle-shaped surface with a diameter of 5mm is exposed.  $\text{CoS}(\beta)$  is formed by dropping 1ml of the solution *Aktivierung*<sup>TM</sup> and 5 ml *Vernetzung*<sup>TM</sup>, subsequently. The electrode is then dried for 24h at room temperature. Fig. 3.3 shows SEM images of bare GC substrate and the GC/ $\text{CoS}(\beta)$  electrode.

?? Counter electrode: Au (Good Fellows 99.9% )

?? Reference electrode:  $\text{Hg}/\text{Hg}_2\text{SO}_4/\text{Na}_2\text{SO}_4$  ( $E = 0.68\text{V}$  vs SHE)



**Figure 3.3** (a) bare GC substrate (b) Electrode GC/ $\text{CoS}(\beta)$

### 3.2.2. X-ray Photoelectron Spectroscopy (XPS)

#### 3.2.2.1. Principle

When a X-ray with energy  $h\nu$  irradiates on the surface of a sample, X-ray photons interact with the inner-shell electrons of the atoms. The interaction causes an energy transfer from the photons to the electrons which then have enough energy to leave the atom and leave the surface of the sample. These electrons, which are called photoelectrons, have a kinetic energy described by the relation:

$$E_{kin} = h\nu - E_b - \phi \quad (3.1)$$

Where  $E_B$  is the binding energy and  $\phi$  is the work function of the spectrometer. The binding energy  $E_B$  is characteristic for an element and can be used to characterize the oxidation states of that element. Since the photoelectron signals come from a depth of about 10-30nm, XPS is an effective method for surface analysis. The concentration  $X_a$  of a component a can be calculated by equation [Sco76]:

$$X_a = \frac{A_a/S_a}{\sum A_i/S_i} \quad (3.2)$$

Where the ratio  $A_i/S_i$  is proportional to the surface concentration of the element  $i$ , and  $A_i$  and  $S_i$  represent the corresponding XPS peak areas and sensitivity factors, respectively.

#### 3.2.2.2. Analyzing procedures

The XPS measurements were carried out using an instrument ESCALAB V(VG). The pressure in the measuring chamber was kept  $p < 10^{-9}$  bar. The X-ray source used was Al-K $\alpha$  ( $h\nu = 1468.6\text{eV}$ , FWHM 0.85eV, 300W) in analyser mode CAE 20eV for detailed spectra and CAE 50eV for survey spectra. The high resolution spectra obtained were acquired using the software UNIFIT<sup>TM</sup>. In order to fit XPS curves, modified curves were obtained e.g. background was subtracted with the Shirley procedure, a defined binding energy was limited (fitted zone). In order to obtain the depth-profile information of the surface, argon sputter with 4eVAr<sup>+</sup> was applied. The sputter rate for polymer surface was 6nm/min [Chan92]. For a metal surface, a relevant sputter rate for TaO<sub>5</sub> ( $\nu = 1.6\text{nm/min}$ ) was used to calculate the thickness of the sputtered layer.



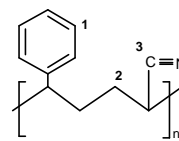
### 3.2.2.3. XPS measurement of polymer surfaces

#### *Surface charging*

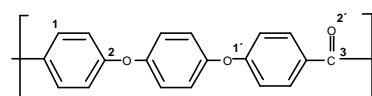
An important problem during XPS measurement of insulating polymer substrates is surface charging. The XP process causes the ejection of electrons from the surface, and thereby results a positive charging of the surface, leading to a shift of the binding energy to higher values. This phenomenon is not observed on metal surface, since electrons on the metal surface are abundant and the ejection does not cause a lack of electron on this surface. The method for correction of the binding energy shift is the calibration of C1s [Chan92][Beam92]. Since most polymers contain large amounts of C in the aromatic ring (i.e. C-C and C-H), the signal for C1s is predominant in these types of binding. Adjustment of the binding energy can be done so that binding energy of aromatic ring C-C and C-H is positioned at 284.5eV. Sputtering also causes a charging phenomenon on the polymer surface, but it results in an increase of the binding energy direction since the Ar<sup>+</sup> sputter flow causes the ejection of positive particles.

#### *Fitting informations*

The standard binding energies, FWHM (full width at maximum intensity), Lorenz for fitting of the polymers are given in table 3.4-3.7.

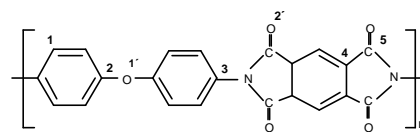
**Table 3.4** Binding energies, FWHM, Lorenz of the species for fitting of the SAN matrix (ABS)  
[Broc95][Chan92][Möb00a]

Element	Binding States	Binding Energy (eV)	FWHM (eV)	Lorenz
C	C-C <sub>arom</sub> (1)	284.5 ? 0.1	2.3	0
	C-C <sub>ali</sub> (2)	285 ? 0.1	1.7	0
	C=N (3)	286.4 ? 0.3	2.1	0.3
	-COOH and/or -COH	284.5 ? 0.1	2.0	0
O	H <sub>2</sub> O <sub>ad</sub>	535.0 ? 0.1	2.3	0
	O-C	533.9 ? 0.1	2.4	0
	O=C	532.5 ? 0.1	1.7	0
	O <sup>2-</sup>	530.5 ? 0.1	1.0	0
N	N= C	398.0 ? 0.2	2.3	0

**Table 3.5** Binding energies, FWHM, Lorenz of the species for fitting of the polymer PEEK  
[Comy96][Ha97][Lau98][Chan92]

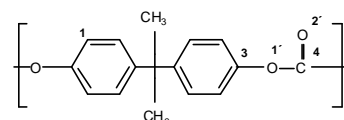
Element	Binding States	Binding Energy (eV)	FWHM (eV)	Lorenz
C	C-C <sub>arom</sub>	284.5 ? 0.1	2.4	0
	C <sub>arom</sub> -O	286.7 ? 0.2	2.0	0
	C <sub>arom</sub> =O	288.3 ? 0.2	1.7	0
	-COOH and/or -COH	288.2 ? 0.3	1.3	0
O	O-C	534.0 ? 0.1	1.8	0.2
	O=C	532.5 ? 0.1	2.3	0.3
	O <sup>2-</sup>	530.5 ? 0.2	1.0	0

**Table 3.6** Binding energies, FWHM, Lorenz of the species for fitting of the polymer PI  
[Ekte00][Wei97][Yan01][Chan92]



Element	Binding States	Binding Energy (eV)	FWHM (eV)	Lorenz
C	C-C <sub>arom</sub>	284.5 ? 0.1	2.2	0.1
	C-O,C-N,C-CO	285.8 ? 0.4	1.7	0
	C <sub>arom</sub> =O	288.6 ? 0.3	2.3	0
	-COOH and/or -COH	288.6 ? 0.2	2.3	0
O	O-C	534.0 ? 0.1	2.5	0.4
	O=C	532.4 ? 0.1	2	0
	O <sup>2-</sup>	530.4 ? 0.2	1	0
N	N-C <sub>arom</sub>	401.0 ? 0.2	2.7	0

**Table 3.7** Binding energies, FWHM, Lorenz of the species for fitting of the PC surface  
[Seid99][Char97][Pat99][Lau00][Chan92]



Element	Binding States	Binding Energy (eV)	FWHM (eV)	Lorenz
C	C-C <sub>arom</sub> (1)	284.5 ? 0.1	2.3	0.1
	C-C <sub>ali</sub> (2)	285.0 ? 0.1	2.1	0
	C <sub>arom</sub> -O (3)	286.2 ? 0.3	1.8	0
	COO (4), -COOH and/or -COH	290.4 ? 0.1	1.5	0
	? ? ?* ?	291.6 ? 0.1	1.0	0
O	O-C	533.9 ? 0.1	2.3	0.4
	O=C	532.3 ? 0.1	1.7	0
	O <sup>2-</sup>	530.7 ? 0.2	0.9	0

### **3.2.3. Microscopes**

Microscopic methods used in this study consist of: optical microscope, Laser profilometry, SEM (Scanning Electron Microscopy) and AFM (Atomic Force Microscopy). Depending on the dimension of the structure, a suitable method should be chosen.

#### **3.2.3.1. Atomic Force Microscopy (AFM)**

Three AFM instruments were used in this work:

1. Topometrix Discoverer TMX 2000
  - Software Topometrix <sup>TM</sup>
2. PicoScan
  - MI SPM-Controller with MI PicoSPM instrument
  - Software PicoScan <sup>TM</sup>
3. DI Nanoscope
  - E Controller with MI PicoSPM instrument
  - Software Nanoscope II5.12r3

Contact mode and Si-cantilever are used in all measurements.

#### **3.2.3.2. SEM, laser profilometer, optical microscope**

SEM imaging and EDAX analyses were carried out using a Environmental Scanning Electron Microscope XL 30 ESEM (Philips)(H<sub>2</sub>O pressure from 0.4-2.6 Torr) with an EDX-analysis component Phoenix Pro (EDAX). More details about the principles and the instruments are introduced elsewhere [w1]. The optical microscope used in this work is a SUSS instrument with a resolution up to x200. The microscope is connected to a digital camera. Samples for cross-section studies were prepared following the procedure described in table 3.8.

**Table 3.8** Preparation of samples for cross-section measurements

<b>Processes</b>	<b>Technical informations</b>
Moulding by epoxy resin	?? Low viscosity epoxy (EPO-THIN, Buehler USA) ?? Hardener (EPO-THIN, Buehler USA) ?? Room temperature
Grinding	?? Sand paper SiC down to 4000 ?? Aluminium oxide down to 1 $\mu$ m
Metallographical etching	?? Etching solution [Petz76] 50ml CH <sub>3</sub> COOH+50ml HNO <sub>3</sub> +10ml H <sub>2</sub> O ?? Room temperature

### 3.2.4. Contact angle measurements

Contact angle measurements were performed at room temperature in a glass chamber using the so-called sessile drop technique with Millipore<sup>®</sup> water as a liquid. Water drops (with a diameter of about 2 mm) were placed onto the substrate surface through a microsyringe taking special care to avoid vibrations of the system. The time required for achieving equilibrium was 3 minutes.

### 3.2.5. Conductivity measurements

4-point conductivity measurements were used in this study with following parameters:

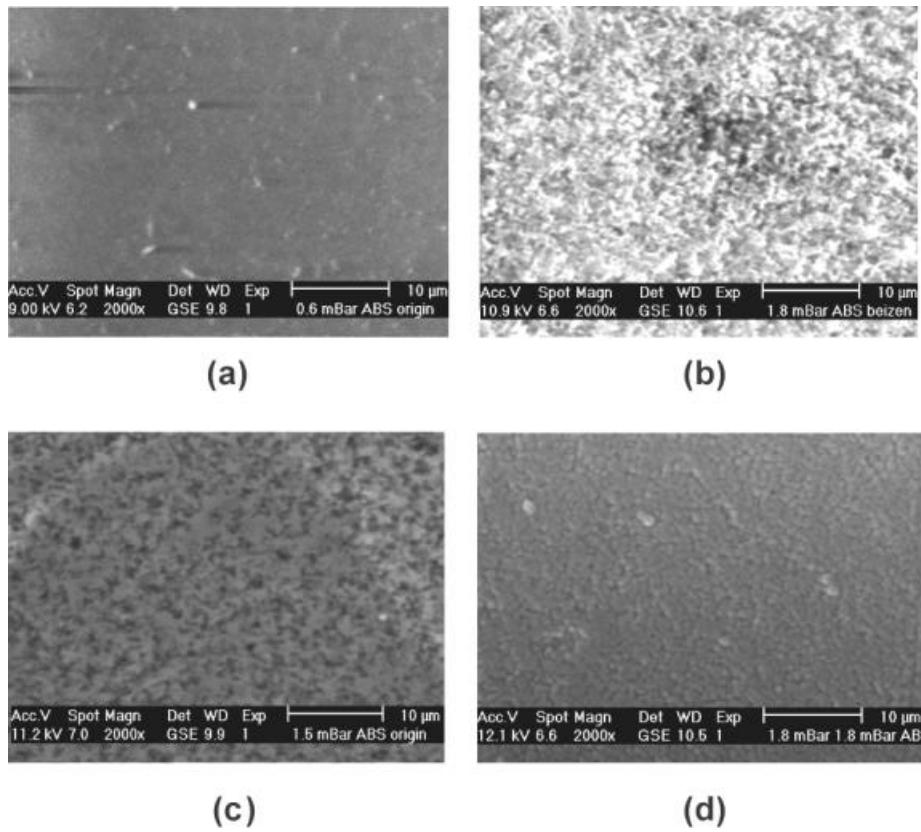
?? Distance between contact tip	1cm
?? Press	7N
?? Applied voltage	10V
?? Amperometer	>10pA

## 4. Pre-treatment (etching and activation)

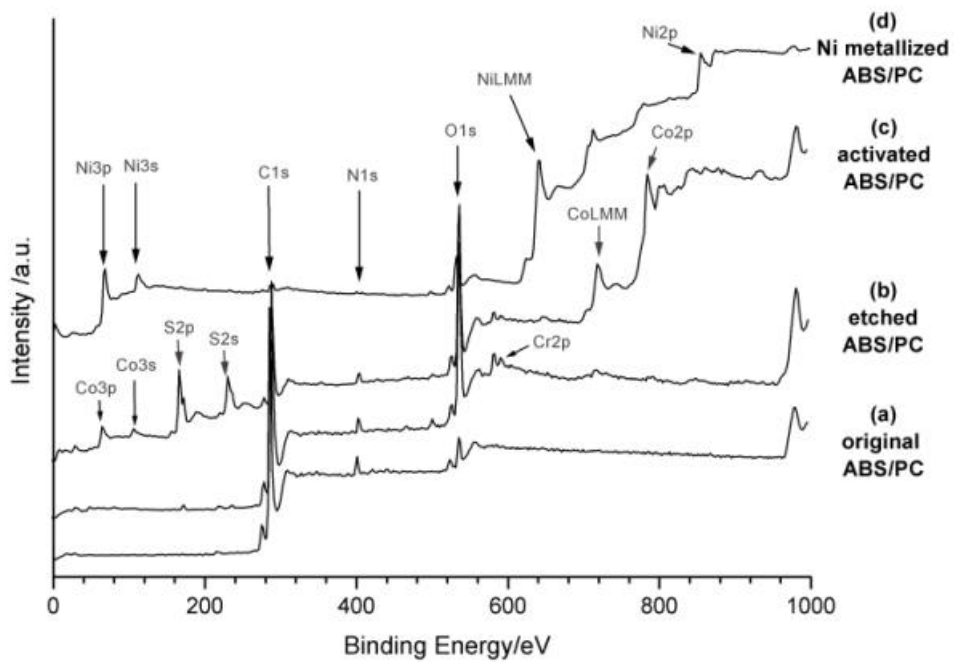
As described in chapter 2.1, the PLATO process consists of three steps: etching, activation by  $\text{CoS}(\beta)$  and metal deposition. Fig. 4.1-4.2 show SEM images and XP survey spectra of an ABS/PC polymer surface after each step as a representative case:

- ?? The etched surface is characterized by a formation of pores (cf. 4.1.b) and high intensity oxygen peaks due to the oxidation during etching (4.2.b). The Cr signal is also observed since the chromate etching solution cannot be removed completely after rinsing.
- ?? The activated surface is characterized by the formation of  $\text{CoS}(\beta)$ , indicated by the appearances of the Co and S signals in the XP spectrum together with signals of C and O (Fig. 4.2c).
- ?? The deposited Ni film is a continuous layer, which covers the whole polymer surface. An intact metal layer is observed in the SEM image and a typical spectrum of a Ni layer is recorded in XP spectrograph (Fig. 4.1d and Fig. 4.2d).

Etching and activation of the polymer surface, which is shortly denoted as pre-treatment, are crucial steps deciding the metal deposition process. Nevertheless, the modification of the surface (roughness, hydrophobicity) also varies when different polymers are used. In this chapter, etching (section 4.1), activation (section 4.2), will be investigated in detail on the four polymers Acrylonitrile-Butadiene-Styrene (ABS), Poly-Ether-Ether-Ketone (PEEK), and Polyimide (PI), Polycarbonate (PC).



**Figure 4.1** SEM images of (a) original, (b) etched (c) activated and (d) Ni metallized ABS/PC polymer surface.



**Figure 4.2** XP survey of (a) original, (b) etched (c) activated and (d) Ni metallized ABS/PC polymer surface.

## 4.1. Etching

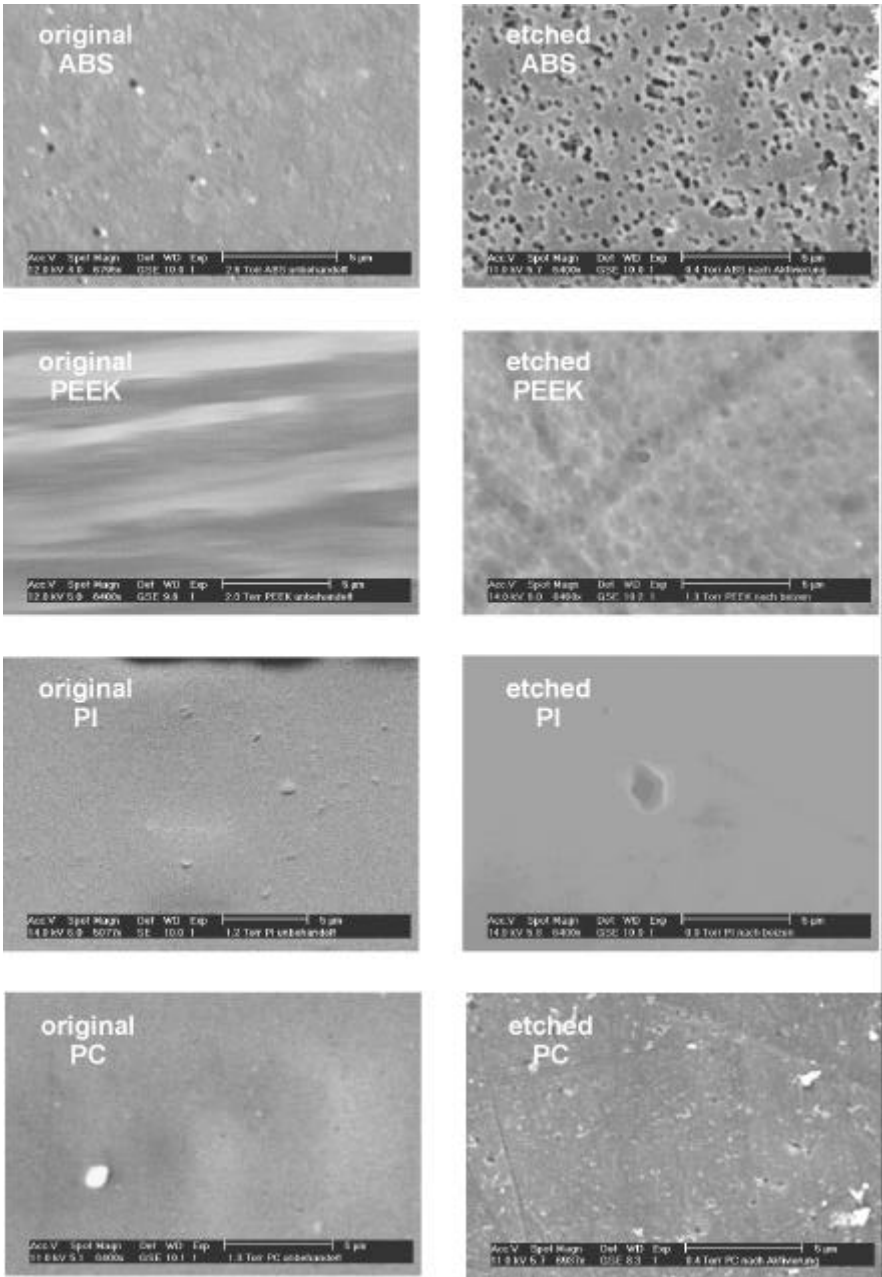
Generally, etching causes changes of roughness and chemical state of the surfaces. Those changes cause an increase of the surface energy. The hydrophilicity of the surfaces increases. In sections 4.2.2 - 4.2.4, the roughness and the chemical state of the surfaces before and after etching are quantitatively characterized using Atomic Force Microscopy (AFM) and X-ray Photoelectron Spectroscopy (XPS). The surface energy is studied using the contact angle measurement and contributions of roughness and chemical changes are calculated.

### 4.1.1. Topographies and roughness

#### *ESEM*

Fig. 4.3 shows ESEM images of the polymers ABS, PEEK, PI and PC before and after chemical etching (procedure is described in 2.1.2). Although the same etching conditions were applied, the resulting surfaces of the different polymer show very different topographies. Porous surfaces are obtained for the etched surfaces of ABS and PEEK, while no significant changes of topographies after etching are observed for PI and PC. In the case of the ABS surface, chromic acid attacks selectively butadiene particles (see table 3.1), leading to the formation of pores. The selective etching also occurs on the surface of semicrystalline PEEK. In this case, chromic acid etching preferentially removes amorphous regions from the PEEK surface, while the crystalline domains are almost stable in the high oxidation media. On the other hand, the surfaces of one-phase PI and PC polymers are homogeneously etched and the formation of pores is not observed on those surfaces.





**Figure 4.3** ESEM images of ABS, PEEK, PI and PC polymer surfaces before and after etching.

*Roughness definition*

The polymer surfaces before and after etching were characterized using AFM measurements. Two parameters were used to analyse the roughnesses of the surfaces: root mean square (rms) roughness  $R_{rms}$  and roughness factor  $r$ .

The root mean square (rms) roughness  $R_{rms}$  is determined by the following equation:

$$R_{rms} = \sqrt{\frac{1}{l} \int_0^l y^2 dx} \quad (4.1)$$

where  $l$  is the roughness sampling length and  $y$  is the height of the roughness trace at a given point from a reference central line. Roughness factor  $r$  is defined by the equation:

$$r = \frac{A}{A_0} \quad (4.2)$$

where  $A$  is the actual area of the surface,  $A_0$  is the apparent area, or geometrical area of the surface. Both parameters  $R_{rms}$  and  $r$  are obtained using data processing after AFM measurements.

#### AFM

Fig. 4.4 - 4.7 show AFM images of ABS, PEEK, PI and PC surfaces before and after etching. The cross-section analyses of the images show that the pores on the etched ABS surface have different sizes which range from 0.5-2 $\mu$ m in diameter and 100-500nm in depth, corresponding to the sizes of butadiene particles. Meanwhile, the dissolved amorphous domains on the semicrystalline PEEK surface have depths of about 50-100nm and diameters of 0.7-1.5 $\mu$ m. Similar to the observation on the ESEM images (Fig. 4.3), no significant changes of topographies for PI and PC before and after etching are observed. The corresponding root mean square roughness of the etched,  $R_{rms}^{(e)}$ , and of the original,  $R_{rms}^{(o)}$ , polymers, as well as and the roughness factor  $r$  are summarized in table 4.1.

**Table 4.1** Surface roughness  $R_{rms}$  and roughness factors  $r$  of different polymer surfaces before (o) and after (e) etching

Polymer	Original surfaces		Etched surfaces		$r^{(e)}/r^{(o)}$
	$R_{rms}$ (nm)	$r^{(o)}$	$R_{rms}$ (nm)	$r^{(e)}$	
ABS	30.9	1.03	115.8	1.76	1.71
PEEK	21.3	1.04	67.9	1.40	1.34
PI	7.0	1.01	10.7	1.06	1.05
PC	10.2	1.01	11.4	1.07	1.06

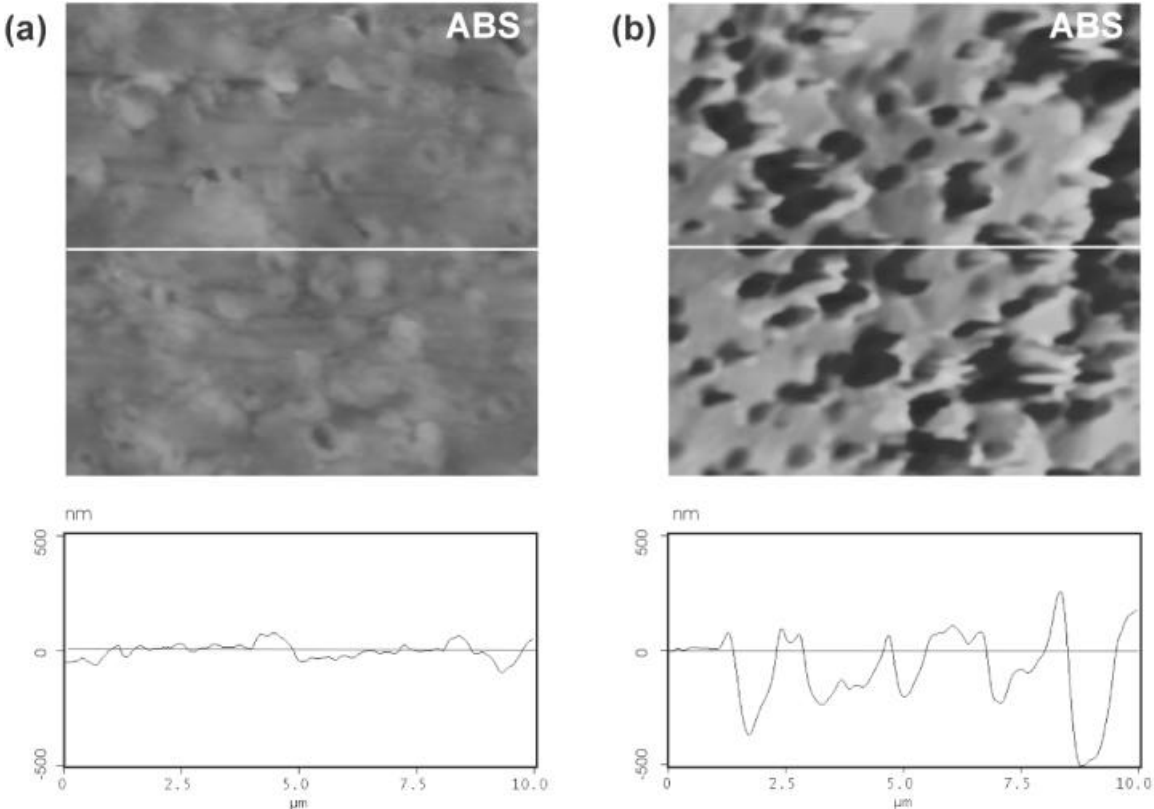


Figure 4.4 AFM images of ABS (a) before and (b) after etching.

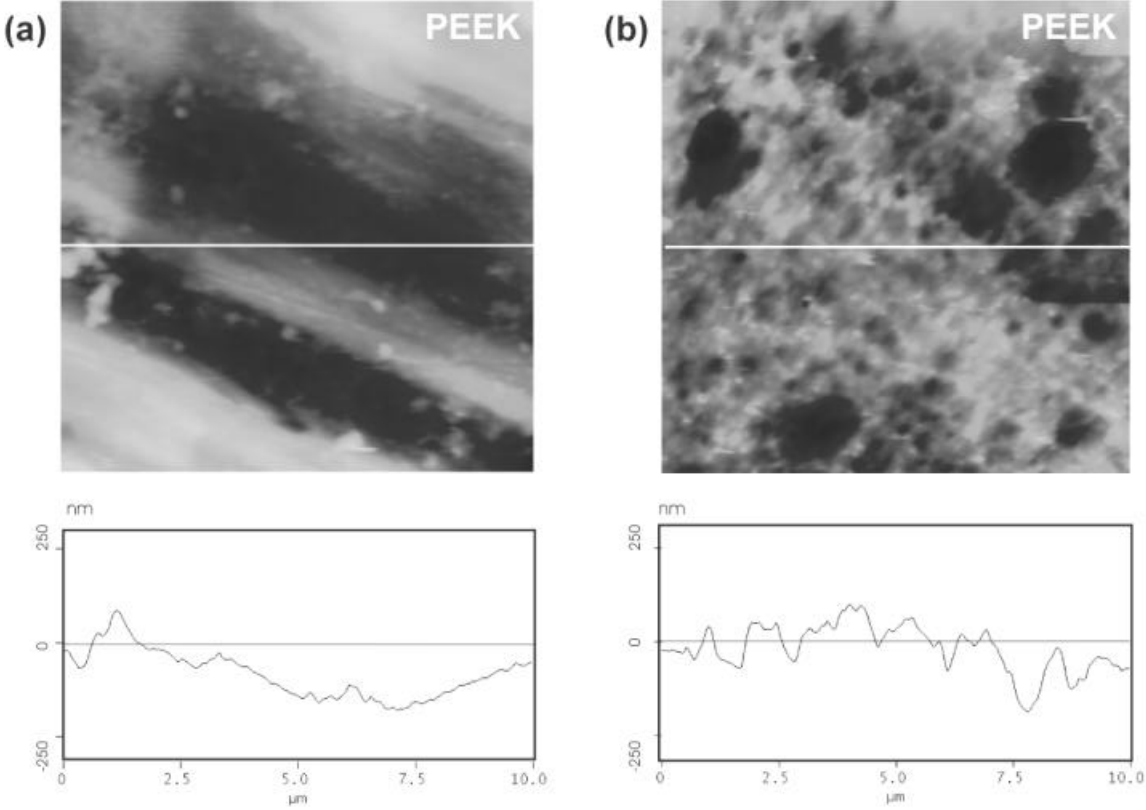


Figure 4.5 AFM images of PEEK (a) before and (b) after etching.

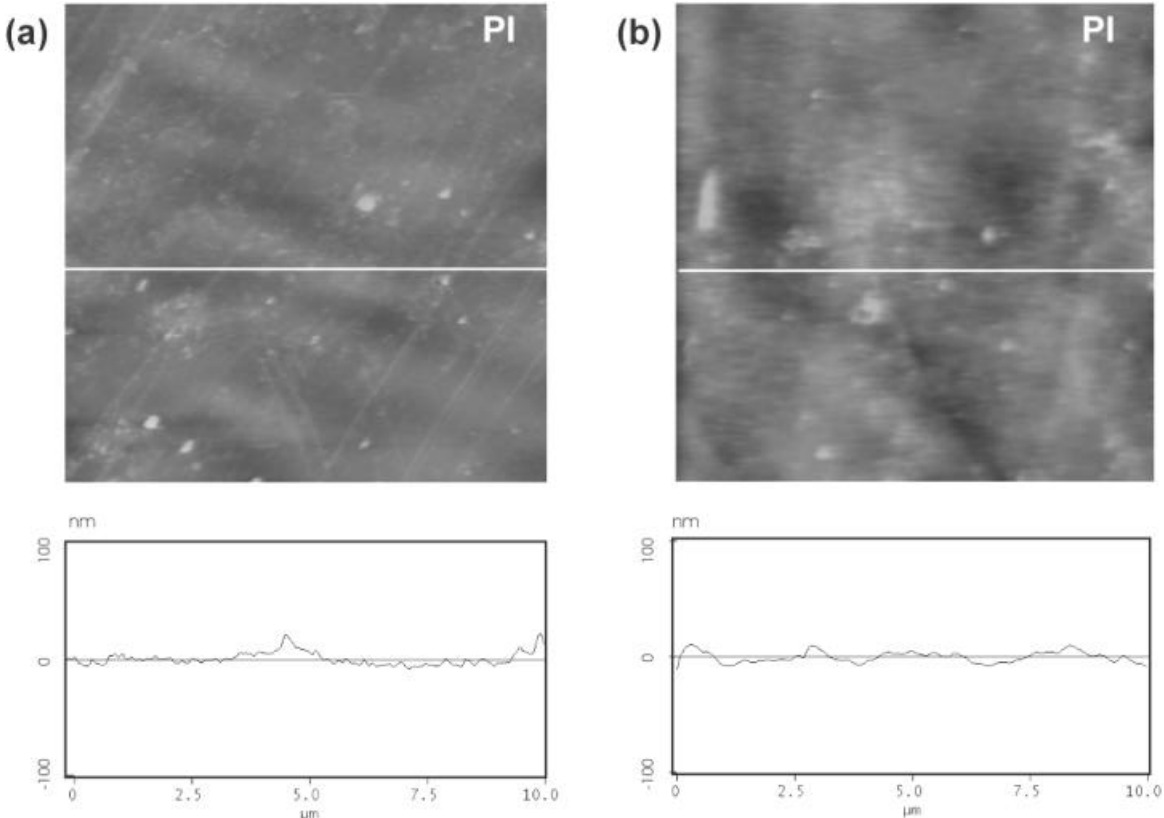


Figure 4.6 AFM images of PI (a) before and (b) after etching.

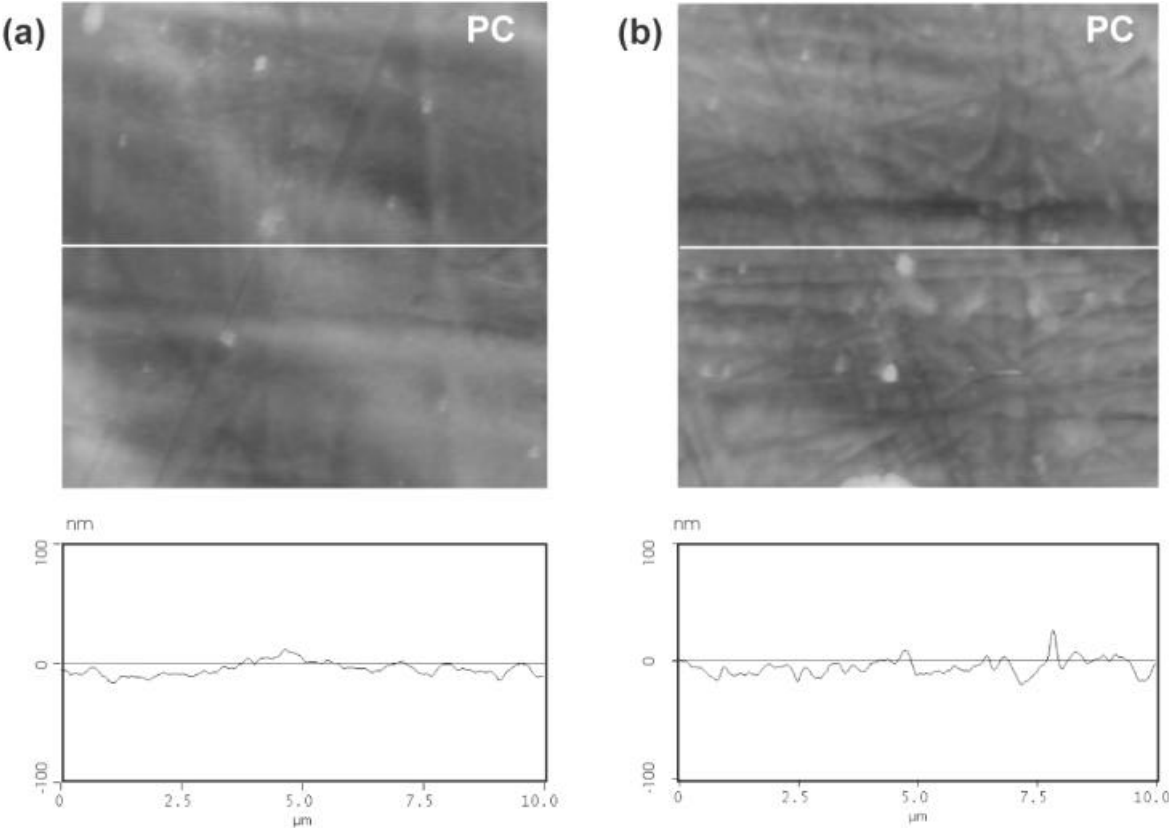
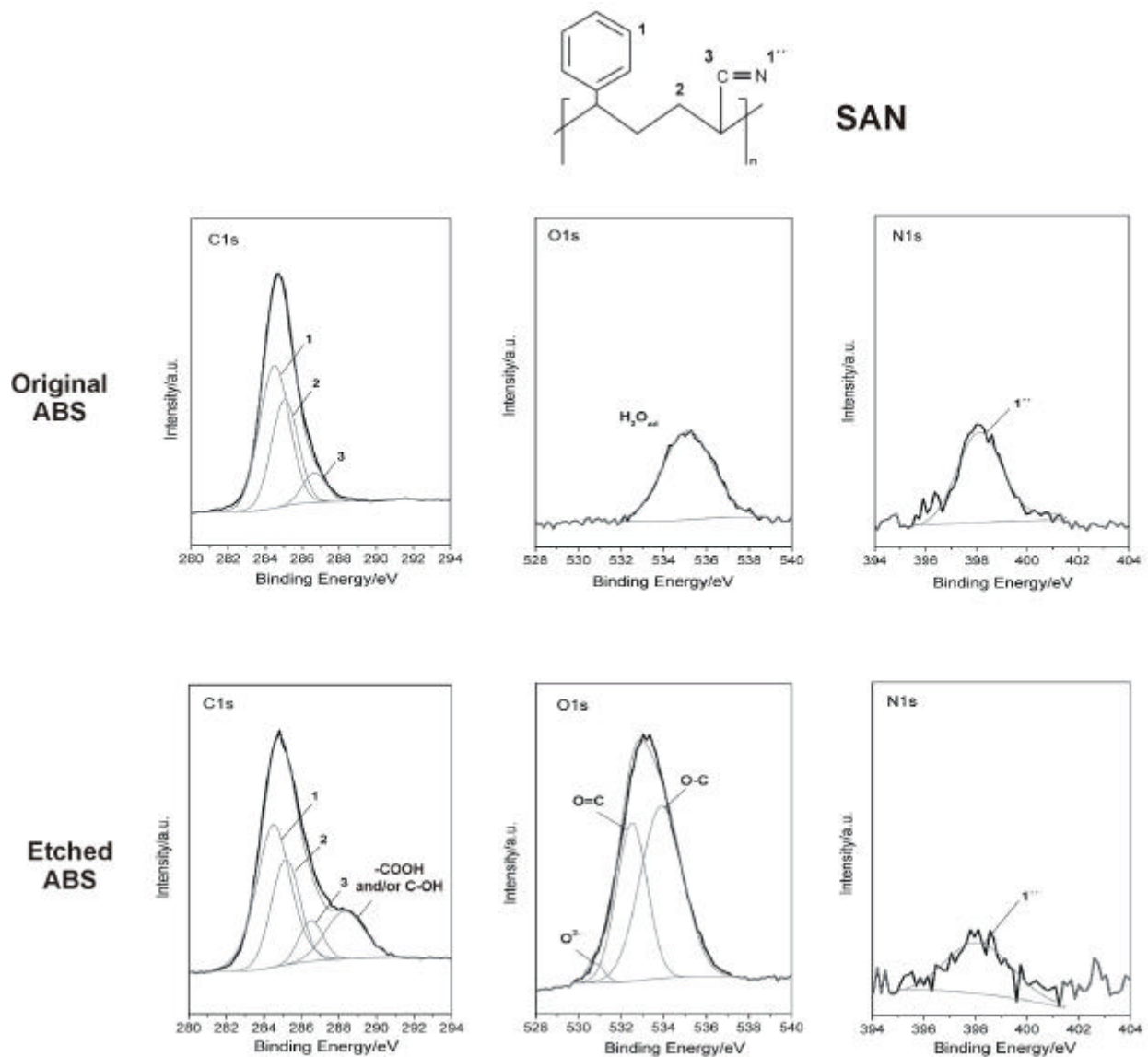


Figure 4.7 AFM images of PC (a) before and (b) after etching.

### 4.1.2. Surface groups (XPS)

#### ABS

As mentioned above, ABS is a two phase material including a Styrole Acrylonitrile (SAN) matrix and butadiene particles. Since the butadiene particles are dispersed in the matrix, the XP signals from the surface of ABS can be attributed to the signals of the SAN material. The deconvoluted signals of C1s, O1s, N1s for the polymer surfaces before and after etching are shown in Fig. 4.8. The numbered deconvoluted peaks correspond to different C-, O- and N-states labelled in the formula of SAN in the figure.



**Figure 4.8** Detailed XPS spectra of the ABS surface before and after etching.

The C signal of the original surface consists of 3 species: aromatic C-C or C-H (1), aliphatic C-C or C-H (2) and C<sup>?</sup>N (3) with the corresponding binding energies and fitting parameters shown in table 3.4. After etching, the peak corresponding to –COOH and/or –COH groups appears due to the oxidation of the surface during the chemical etching. Concentration ratio of C species before and after etching are both near the stoichiometry of SAN (cf. table 4.2).

The O signal observed on the original ABS surface with the binding energy of 535 eV is attributed to adsorbed water, since the original SAN does not include O elements in its structure [Broc95]. After etching, the surface consists of 3 species: O-C (1<sup>ˆ</sup>) and C=O (2<sup>ˆ</sup>) from the –COOH and/or C-OH groups and O<sup>2-</sup> (3<sup>ˆ</sup>) from chromate, which cannot be removed completely after rinsing. It should be noted that the ratio O(1<sup>ˆ</sup>):O(2<sup>ˆ</sup>)=1: 0.6, which is in the range from 1:0 (100% –COH) to 1:1(100% –COOH). Both signals of N1s before and after etching correspond to the N<sup>?</sup>C binding.

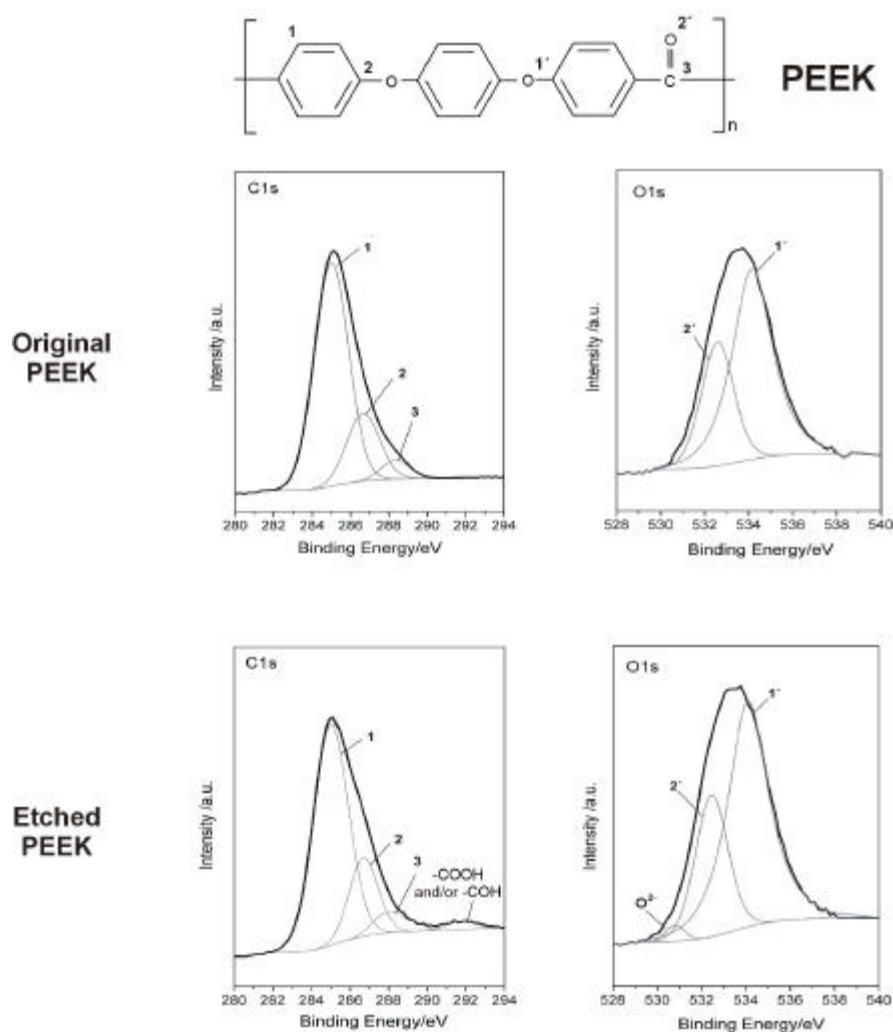
Thus, the ABS surface after etching is characterized by the formation of –COOH and/or –COH groups and the element concentration ratio O/C (C=C(1)+C(2)+C(3)+C(COOH); O=O(1)+O(2)) increases after etching due to the oxidation of the surface (cf. table 4.2) .

**Table 4.2.** Concentration ratios of species in C and O signals and element concentration O/C for ABS

Species	Concentration ratio			
	original surface		etched surface	
	Theor.	Exp.	Theor.	Exp.
C(1) : C(2) : C(3) : C(0) <sup>*</sup> (stoichiometrical)	6 : 4 : 1 : 0	6 : 4.2 : 1.8 : 0	6 : 4 : 1 : x	6 : 4.5 : 1.5 : 1.5
O(1 <sup>ˆ</sup> ) : O(2 <sup>ˆ</sup> )	0 : 0	0 : 0	2 : (1÷2)	1.6 : 1
O/C	0 : 1	0.12 : 1	~	0.92 : 1

\* C(0) represents the species –COOH and/or –COH

## PEEK



**Figure 4.9** Detailed XP spectra of the PEEK surface before and after etching.

Fig. 4.9 shows deconvoluted signals of C1s, O1s for the PEEK surfaces before and after etching. The C signal of the original surface includes 3 species: aliphatic C-C and C-H (1), C<sub>arom</sub>-O (2) and C=O (3). The corresponding binding energies and fitting parameters are shown in table 3.5. It should be noted that, similar to the ABS surface, -COOH and/or -COH groups also appear on the etched PEEK due to the oxidation of the polymer surface. The concentration ratios of the species (1), (2) and (3) are near stoichiometry for both original and etched surfaces (cf. table 4.3).

The O signal from the original PEEK surface consists of 2 species, corresponding to the bonds O-C (1') and O=C (2'). The concentration ratio O(1')/(O2') is also near the stoichiometry of the PEEK molecular unit (table 4.3). After etching, the formation of -COOH and/or -COH groups leads to the new sources of O-C and O=C species, resulting in an increase of the

concentration ratio  $O(1')/O(2')$ . Since the  $-COOH$  and/or  $-COH$  groups themselves have a concentration ratio  $O(1')/(O(2')) \approx 1$ , the concentration ratio  $O(1')/(O(2'))$  of the PEEK surface increases after etching (cf. table 4.3).

Thus, the PEEK surface after etching is characterized by the formation of  $-COOH$  and/or  $-COH$  groups and the element concentration ratio  $O/C$  ( $C=C(1)+C(2)+C(3)+C(COOH)$ ;  $O=O(1)+O(2)$ ) increases after etching due to the oxidation of the surface (cf. table 4.3)

**Table 4.3** Concentration ratios of species in C and O signals and element concentration O/C for PEEK

Species	Concentration ratio			
	original surface		etched surface	
	Theor.	Exp.	Theor.	Exp.
$C(1):C(2):C(3):C(0)^*$	12 : 6 : 1 (stoichiometrical)	12 : 6.5 : 1.2	12 : 6 : (1+x)	12 : 6.9 : 3.1
$O(1'):O(2')$	2 : 1	2 : 1.2	(1÷2) : 1	1.5 : 1
$O : C$	3 : 19	3 : 17.8	~	3 : 7.4

\*  $C(0)$  represents the species  $-COOH$  and/or  $-COH$

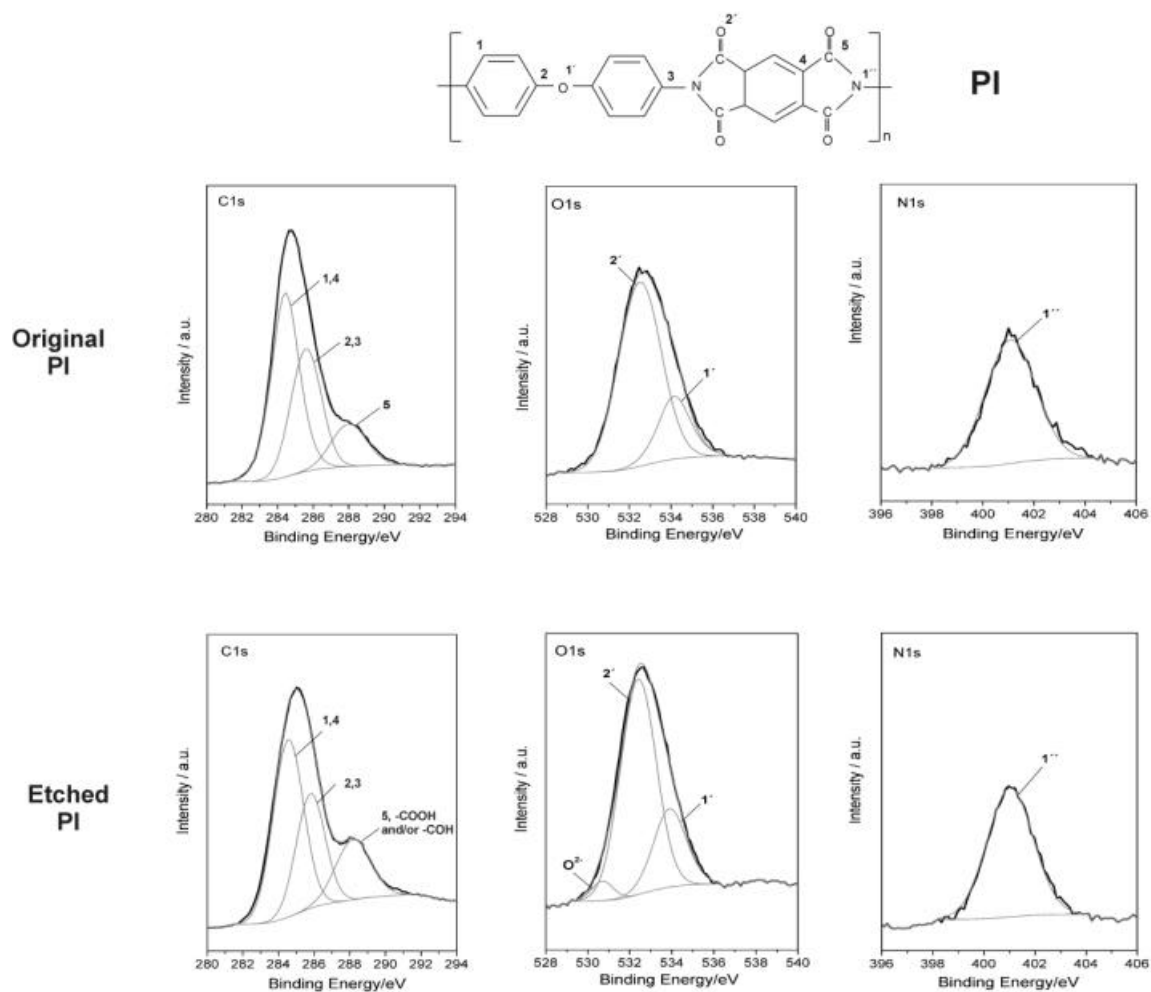
### PI

Fig. 4.10 shows the deconvoluted signals of C1s, O1s for the PI surfaces before and after etching. The C signal of the original PI surface includes several species, corresponding to the C positions labeled from 1 to 5. It should be noted that the species 1,4 as well as 2,3 have the same binding energies. Therefore, they overlap each other and can only be represented as sum fitting peaks 1,4 and 2,3, as shown in Fig. 4.10. The binding energies and fitting parameters are given in table 3.6. After etching, the formation of  $-COOH$  and/or  $-COH$  groups is also observed with the binding energy in the range of species (5). As a result, the species  $-COOH$  and/or  $-COH$  overlap the specie (5) and the sum peak has higher intensities, compared to peak (5) from the original surface. The concentration ratio of species are shown in table 4.4.

Similar to the PEEK surface, two O species are found corresponding to the bonds of  $O-C$  ( $1'$ ) and  $O=C$  ( $2'$ ), with concentration ratio shown in table 4.4. After etching, signal  $O^{2-}$  appears due to chromate, which cannot be removed completely and the ratio  $O(1')/O(2')$  increases due to the formation of  $-COOH$  and/or  $-COH$  groups. N signals, which are attributed to the N-CO bond, are observed in both original and etched surfaces.



Thus,  $-\text{COOH}$  and/or  $-\text{COH}$  groups are formed and the element concentration ratio O/C ( $\text{C}=\text{C}(1,4)+\text{C}(2,3)+\text{C}(5,-\text{COOH})$ ;  $\text{O}=\text{O}(1)+\text{O}(2)$ ) increases after etching due to the oxidation of the surface (cf. table 4.4).



**Figure 4.10** Detailed XP spectra of the PI surface before and after etching.

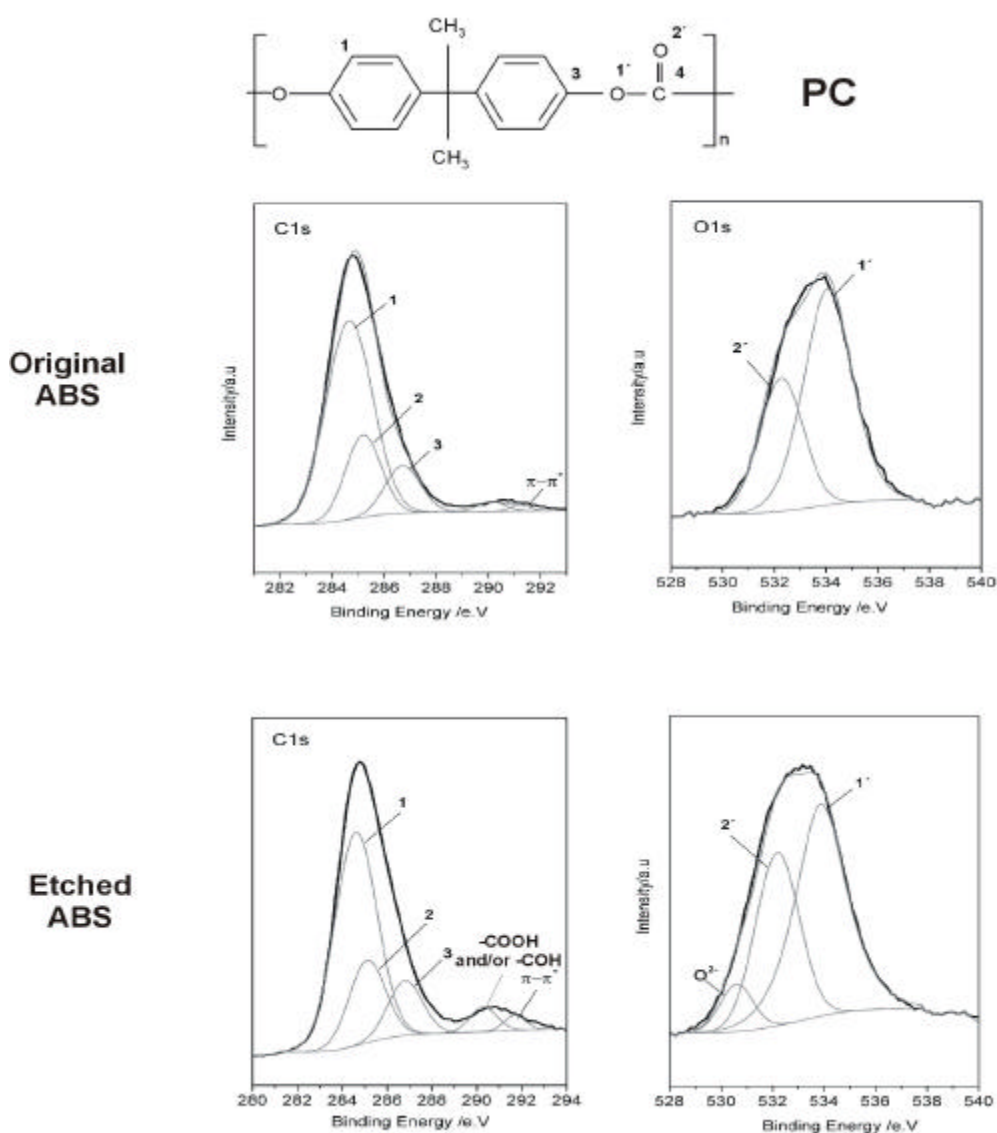
**Table 4.4** Concentration ratios of species in C and O signals and element concentration O/C for PI

Species	Concentration ratio			
	original surface		etched surface	
	Theor.	Exp.	Theor.	Exp.
$\text{C}(1,4):\text{C}(2,3): \text{C}(5,0)^*$	10 : 8 : 4 (stoichiometrical)	10 : 8.2 : 3.7	10 : 8 : (4+x)	10 : 8.7 : 6.5
$\text{O}(1') : \text{O}(2')$	1 : 4	1 : 3.8	1 : (4÷5)	1 : 2.2
$\text{O} : \text{C}$	5 : 22	5 : 20.6	~	5 : 12.3

\* C(0) represents the species  $-\text{COOH}$  and/or  $-\text{COH}$

## PC

The deconvoluted C signal shows 5 species corresponding to the bonds: aliphatic C-C and C-H (1), aromatic C-C and C-H (2), C-O (3), C=O(4) and  $\pi-\pi^*$  with fitting parameters shown in table 3.7. After etching,  $-\text{COOH}$  and/or  $-\text{COH}$  groups formed overlap peak C=O (4), leading to an increasing intensity at 290.2eV (Fig 4.11). Two oxygen species are found, corresponding to the bonds of O-C (1') and O=C (2'), with the concentration shown in table 4.5. The concentration ratio O(1')/O(2') increases after etching due to the formation of  $-\text{COOH}$  and/or  $-\text{COH}$  groups. Similar to the surfaces of ABS, PEEK and PI, element concentration ratio of O/C increases after etching due to the oxidation of the surface.



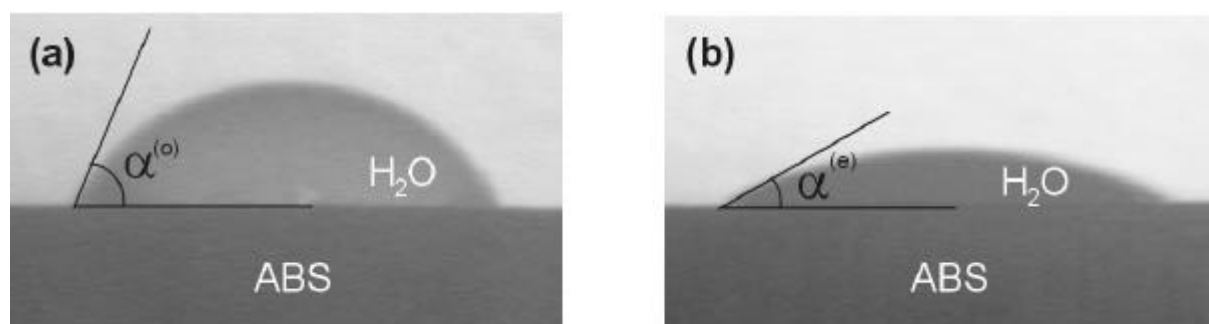
**Figure 4.11** Detail XP spectra of the PC surface before and after etching.

**Table 4.5** Concentration ratios of species in C and O signals and element concentration O/C for PC

Species	Concentration ratio			
	original surface		etched surface	
	Theor.	Exp.	Theor.	Exp.
C(1):C(2):C(3):C(4+0)	10 : 3 : 2 : 1 (stoichiometrical)	10 : 3.2 : 1.9 : 0.9	10 : 3 : 2 : (1+x)	10 : 4 : 2.3 : 2.1
O(1'):O(2')	2 : 1	2 : 1.1	(1÷2) : 1	1.7 : 1
O/C	3 : 16	3 : 13.5	~	3 : 7.3

\* C(0) represents the species –COOH and/or –COH

#### 4.1.2. Contact angle measurement and surface energy



**Figure 4.12** Contact angle measurement on (a) original  $\alpha^{(o)}$  and (b) etched  $\alpha^{(e)}$  surface.

Fig. 4.12 shows the contact angle measurements on the original and etched ABS surfaces. The contact angle on the etched surface is obviously lower than that on the original surface, indicating that the surface is hydrophilized due to etching. The corresponding surface energies of original and etched surfaces are calculated by the Young-Dupre equation (2.4). The measured contact angles of original and etched surfaces  $\alpha^{(o)}$  and  $\alpha^{(e)}$  as well as the values for  $\gamma^{(o)}$ ,  $\gamma^{(e)}$  of the four polymers, are summarized in table 4.6. It is shown that for all polymers, contact angles decrease and surface energies increase after etching.

**Table 4.6** Contact angles  $\theta$  and surface energies  $\gamma$  for different polymers before (o) and after (e) etching

polymer	original surfaces		etched surfaces		$\gamma_{\text{total}}^{(e)}$ (mJ.m <sup>-2</sup> )
	$\theta^{(o)}$	$\gamma^{(o)}$ (mJ.m <sup>-2</sup> )	$\theta^{(e)}$	$\gamma^{(e)}$ (mJ.m <sup>-2</sup> )	
ABS	68°	34.5	32°	62.3	28.8
PEEK	72°	31.2	39°	57.6	26.4
PI	67°	35.2	48°	50.8	15.6
PC	69°	33.6	56°	44.3	10.7

Generally, the increase of surface energy after etching,  $\gamma^{(e)}$ , is due to the two contributions: (i)  $\gamma_r$  from the increase of roughness and (ii)  $\gamma_{\text{COOH}}$  from the formation of –COOH and /or –COH groups. Thus:

$$\gamma^{(e)} = \gamma_r + \gamma_{\text{COOH}} \quad (4.3)$$

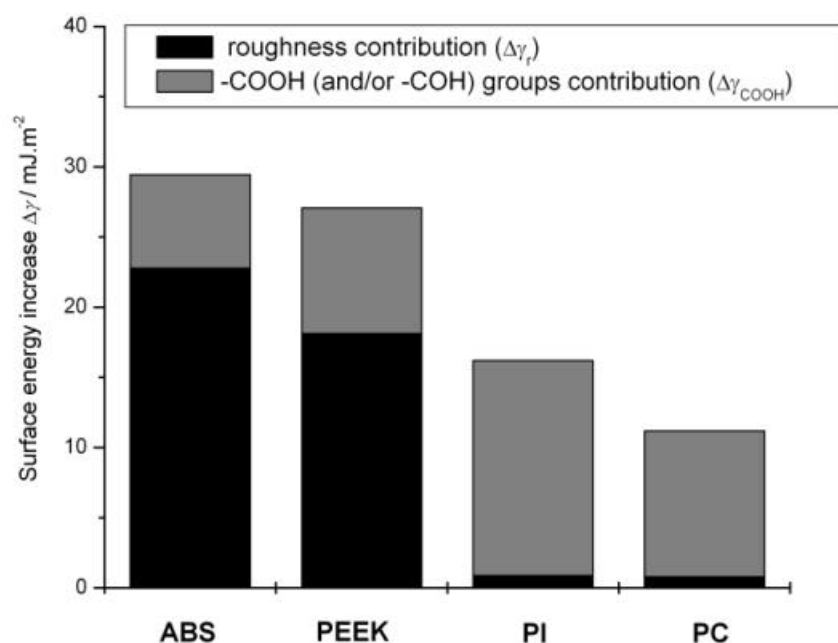
The roughness contributions  $\gamma_r$  were estimated from the equation

$$\gamma_r = \frac{\gamma_w}{4} \left( \frac{1}{\cos \theta_r^{(e)}} - \frac{1}{\cos \theta_r^{(o)}} \right) \quad (4.4)$$

In this equation  $\theta_r^{(e)}$  represents the expected contact angle of the etched surface by considering only the effect of roughness increase. The  $\theta_r^{(e)}$ -values were calculated from the roughness factors  $r^{(e)}$  and  $r^{(o)}$  of the original and etched polymer surfaces determined by AFM (cf. table 4.1) using the modified Wenzel relation (see chapter 2.1.1):

$$\cos \theta_r^{(e)} = \frac{r^{(e)}}{r^{(o)}} \cos \theta_r^{(o)} \quad (4.5)$$

The estimated  $\gamma_r$ - and  $\gamma_{\text{COOH}}$ -contributions to  $\gamma^{(e)}$  for different polymer substrates are presented in Fig. 4.13. The results show that the large surface energy increase of ABS and PEEK is mainly due to the increase of the surface roughness during the etching treatment, whereas the surface energy of PI and PC increases predominantly due to the formation of COOH (and/or COH) surface groups.



**Figure 4.13** Contributions of the surface roughness and the formation of -COOH and/or -COH groups to the surface energy increase of polymer substrates after etching.

## 4.2. Activation

### 4.2.1. Influence of the etched polymer surface on the activation

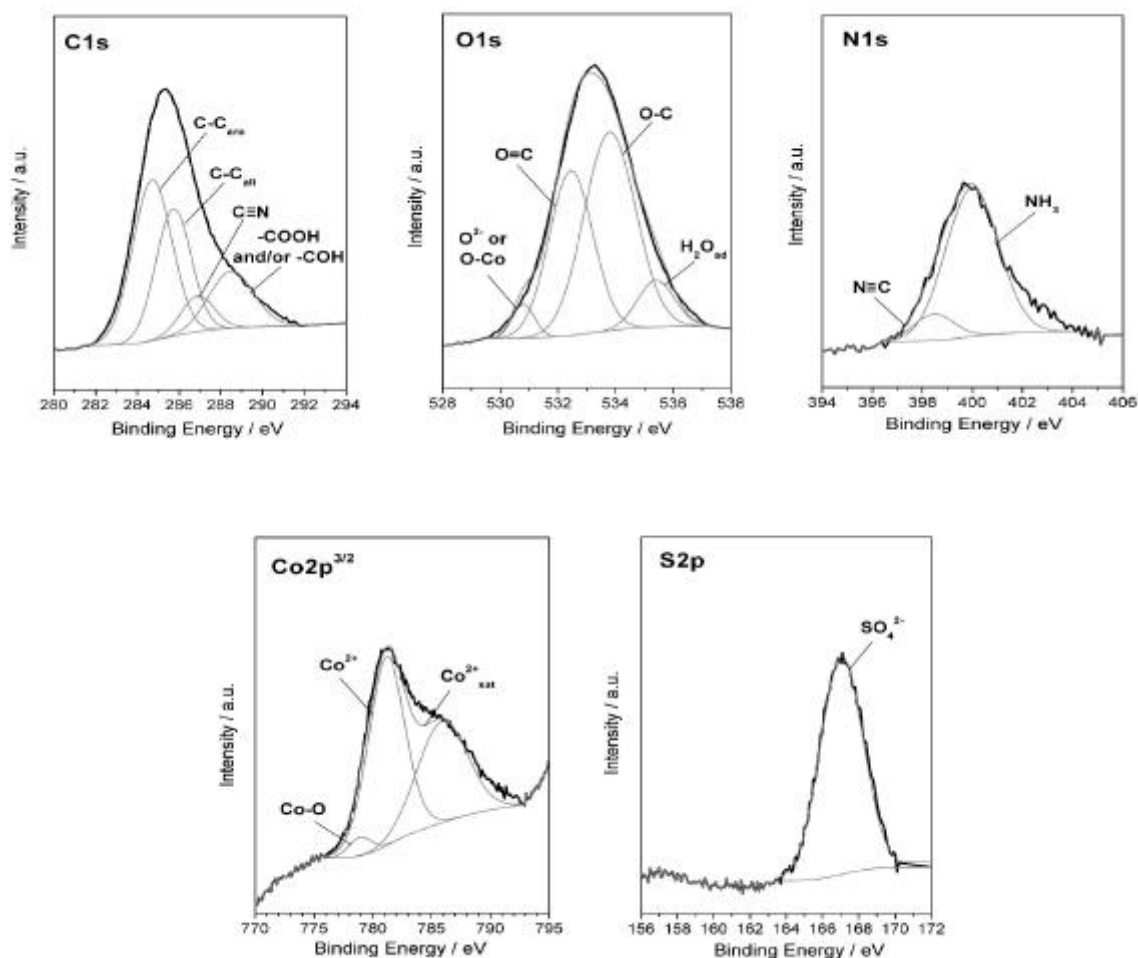
As introduced in chapter 2.1, the activation consists of two steps: (a) adsorption of the cobalt-complexes and (b) sulphidation. The surfaces after adsorption and sulphidation will be characterized using XPS.

#### *Adsorption of the cobalt-complex*

Fig. 4.14 shows the XP detailed spectra of C1s, O1s, N1s, Co2p and S2p recorded on an ABS surface after the adsorption of the cobalt-oxygen-complex. Similar to the etched ABS surface (see 4.1.2), the deconvoluted C signal consists of species: aromatic C-C or C-H (284.5eV), aliphatic C-C or C-H (285eV) and C<sup>?</sup>N (286.8eV) and the -COOH and/or -COH groups (288.7eV). It should be noted that the intensity of the peak for -COOH and/or -COH is lower than that of the etched surface, indicating that a part of -COOH and/or -COH groups is degraded in the cobalt-complex-solution (pH=10). The O signal consists of 4 species: O<sup>2-</sup> from the chromate or O-Co in oxygen-cobalt-complex (530.9eV), O=C (532.6eV) and O-C

(532.9eV) of the  $-\text{COOH}$  and/or  $-\text{COH}$  groups and  $\text{H}_2\text{O}$  adsorbed on the surface (535.1eV). The N signal includes species  $\text{N}\equiv\text{C}$  (398.6eV) and  $\text{NH}_3$  (400.1eV) from the cobalt-complex.

It should be mentioned that in the deconvoluted  $\text{Co}2\text{p}^{3/2}$  signal, not only species of  $\text{Co}^{2+}$  (781.5eV), but also the species  $\text{Co-O}$  (779.3eV) of the Co-oxygen-complex are observed (Fig. 4.14). The S signal includes only the  $\text{SO}_4^{2-}$  peak at 167.8eV.



**Figure 4.14** Detailed XP spectra of different elements on the ABS surface with adsorbed cobalt complex.

*Sulphidation*

Fig. 4.15 shows XP spectra of the C, O, Co and S measured on an activated ABS surface (ABS polymer/CoS( $\beta$ )). Not only the expected signals of Co and S, but also C and O peaks are obtained, indicating that the CoS( $\beta$ ) layer does not cover the polymer surface completely. The coverage of CoS( $\beta$ ) can be determined using the peak area of the species. It is important to note that not all species are used for the calculation of coverage. The  $H_2O_{ads}$  peak should be excluded since this peak is not from the free polymer surface. Similarly,  $SO_4^{2-}$  is not used for calculation of coverage since this signal is not from the CoS( $\beta$ ) clusters. The appearance of  $SO_4^{2-}$  is explained by the adsorption of the cobalt-complex solution, which was not removed completely after rinsing. In Fig. 4.15, the peaks used for calculation coverage are marked by hatched areas. The coverage  $\theta$  of CoS( $\beta$ ) on polymer surfaces can be determined by equation:

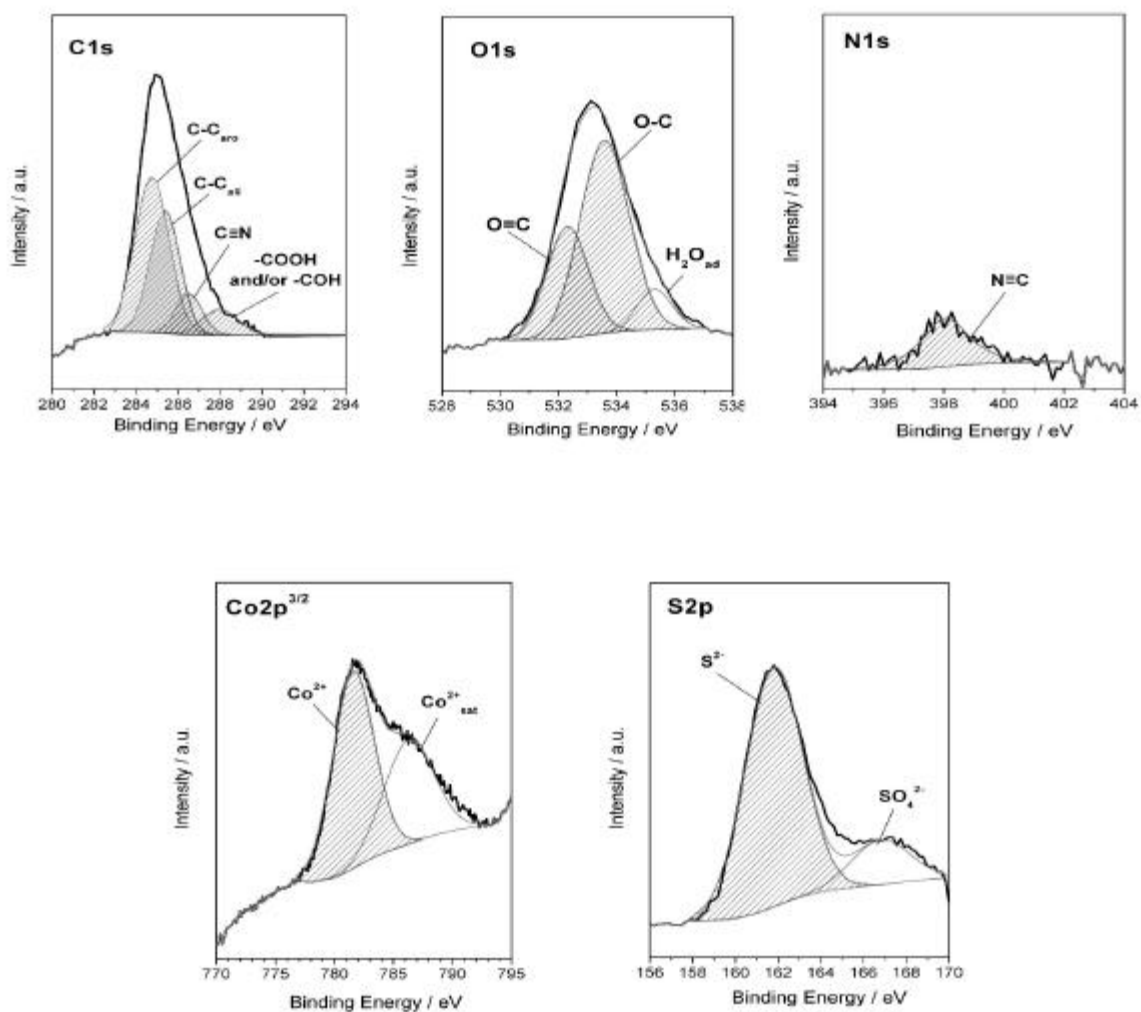
$$\theta = \frac{A_{Co}/S_{Co} + A_S/S_S}{\sum_i A_i/S_i} \quad \text{with } i = Co, S^{2-}, C, O, N. \quad (4.6)$$

In this equation the ratio  $A_i/S_i$  is proportional to the surface concentration of the element  $i$ , and  $A_i$  and  $S_i$  represent the corresponding XPS peak areas and sensitivity factors, respectively.

Table 4.7 shows the coverage of CoS( $\beta$ ) determined using relation (4.6) for the four polymers ABS, PEEK, PI, PC after one activation cycle.  $\theta$ -values increase in the sequence PC, PI, PEEK and ABS. These results correlate well with the surface roughness data of those polymers (cf. table 4.1), and indicate that the surface roughness is a decisive factor influencing the activation degree. It is also very important to mention that the electrodeposition process could be induced only on activated substrates, which exhibit a relatively high CoS( $\beta$ ) coverage ( $\theta > 30\%$ ). Thus, activated surfaces of ABS and PEEK can be metallized due to their higher coverage, while the metal deposition cannot be induced on activated PI, PC after one activation cycle (cf. table 4.7).

**Table 4.7.** Coverage of cobalt sulphide on ABS, PEEK, PC and PI after one activation cycle

polymer	ABS	PEEK	PI	PC
Coverage $\theta$ %	49 %	36 %	17 %	15 %
	(metallizable)	(metallizable)		

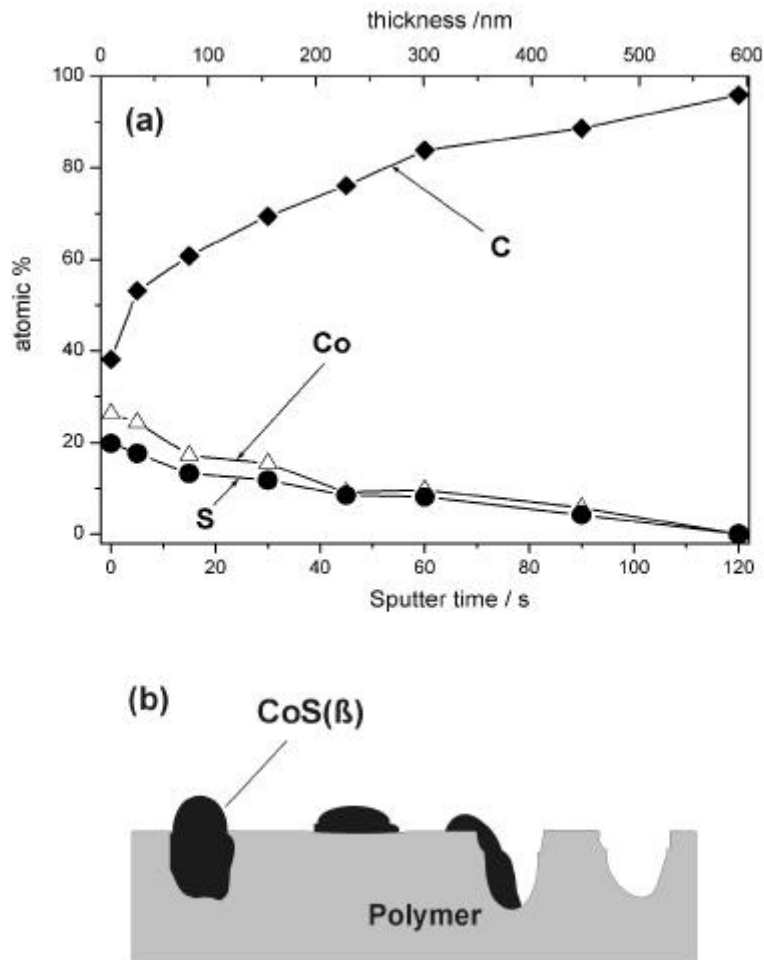


**Figure 4.15** Detailed XPS spectra of different elements on the activated ABS surface. Hatched areas are used for determination of the CoS( $\beta$ ) coverage ?.

#### 4.2.2. Influence of the activation cycle on the coverage

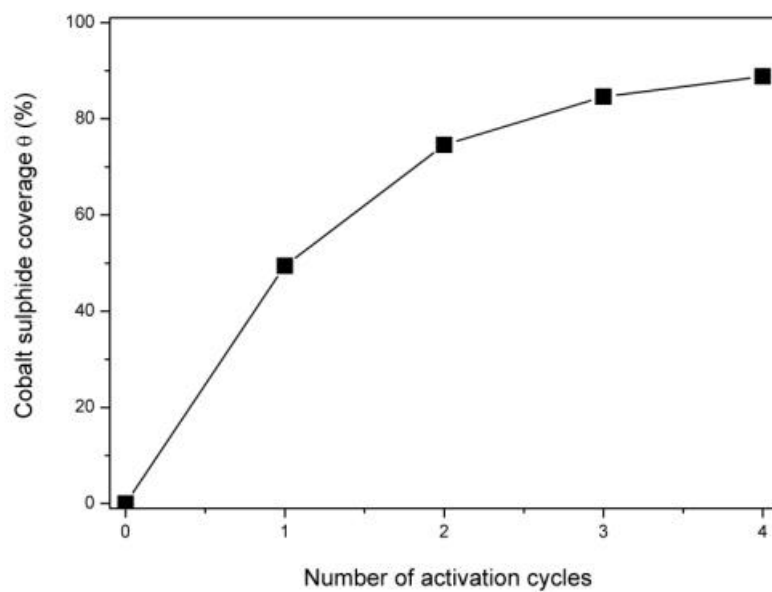
Fig. 4.16a shows typical XPS sputter depth profiles of Co, S and C for an ABS surface after a single activation. As can be seen, the Co signal disappears after 120 minutes sputtering time, corresponding to a depth of about 600 nm, which is comparable to the depth of the pits observed on etched ABS surfaces by AFM (Fig. 4.4.b). It is reasonable to suggest from these results that the CoS( $\beta$ ) clusters are located preferentially in the pits of the etched ABS surface as schematically shown in Fig. 4.16b. The fact that the coverage of CoS( $\beta$ ) is only 49% while the pits occupy 60-80% area of the surface indicates that some pits or parts of pits are still free of CoS( $\beta$ ).





**Figure 4.16** XPS sputter profile (a) and schematic presentation (b) of an etched ABS surface after single activation with  $\text{CoS}(\beta)$  (one activation cycle).

It was found that repetition of the activation procedure for several times results in a significant increase of the  $\text{CoS}(\beta)$  coverage  $\theta$ . The change of the colour from of the activated surface due to the increasing coverage after applying several activation cycles can be observed by optical microscope. Fig. 4.17 shows  $\theta$  as a function of repeated activation cycles for ABS. As can be seen, after single activation,  $\theta$  is 49% and reaches an approximately constant value of about 86% after four activation cycles. This effect is explained by the filling of  $\text{CoS}(\beta)$  on the free pits (Fig. 4.16b) after each activation cycle. After four activation cycles, all pits are filled by  $\text{CoS}(\beta)$ , leading to the saturation behaviour of the coverage.



**Figure 4.17** Dependence of the CoS( $\beta$ ) coverage  $\theta$  on the number of activation cycles for an etched ABS surface.

## 5. Metal deposition

Metal deposition in the PLATO process is induced by electrical contact tips and characterized by the lateral propagation of the metal layer. Two characteristic features of the process will be considered in this study, including:

- (i) The possibility for electrodeposition to take place on activated surface of a very low conductivity. Electrochemical properties of CoS( $\beta$ ) can probably play a role in the metal deposition process.
- (ii) Mechanism of the propagation is not understood. Nucleation and growth of the metal in this case are influenced by the uneven and time dependent potential distribution.

In chapter 5.1, studies of the electrochemistry of CoS( $\beta$ ) will be presented. In chapter 5.2, kinetics of metal electrodeposit will be focussed: Results for characterization of Ni layers formed during propagation and the simulation of the growth of deposited layer will be reported. Influences of deposition potential( $E$ ), coverage of CoS( $\beta$ )(?), electrolyte concentration ( $C_{Ni}$ ) will also be discussed. In chapter 5.3, the deposition mechanisms will be discussed, considering the questions: why the deposited layer propagates laterally during the deposition process.

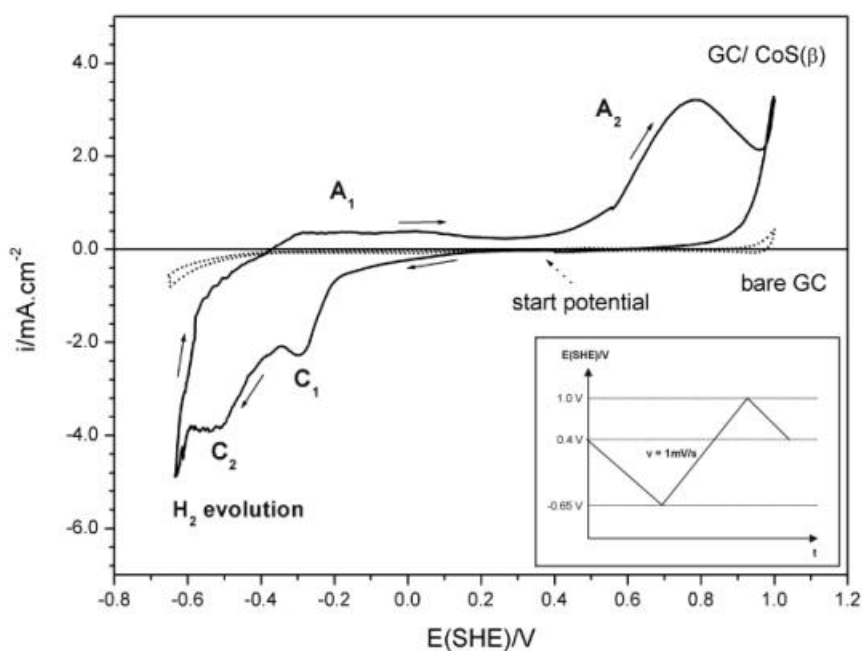
## 5.1. Electrochemistry of cobalt sulphide

Electrochemistry of CoS( $\beta$ ) was studied using CoS( $\beta$ ) covered glassy carbon (GC) electrodes (GC/CoS( $\beta$ )). The preparation of the electrode GC/CoS( $\beta$ ) is described in chapter 3.2. Cyclic voltammetric measurements were performed in the two electrolytes:

- Ni free electrolyte  $S_0$  (0.1M NaCl + 0.9MNa<sub>2</sub>SO<sub>4</sub> + H<sub>3</sub>BO<sub>3</sub>,  $C_{Ni}=0$ )
- Ni containing electrolyte  $S_{Ni}$ : (0.1MNiCl<sub>2</sub> + 0.9MNiSO<sub>4</sub> + H<sub>3</sub>BO<sub>3</sub>,  $C_{Ni}=1M$ )  
( $pH=4$ ,  $T=25^\circ C$  for both solutions)

### 5.1.1. Electrochemistry of CoS( $\beta$ ) in a Ni free solution

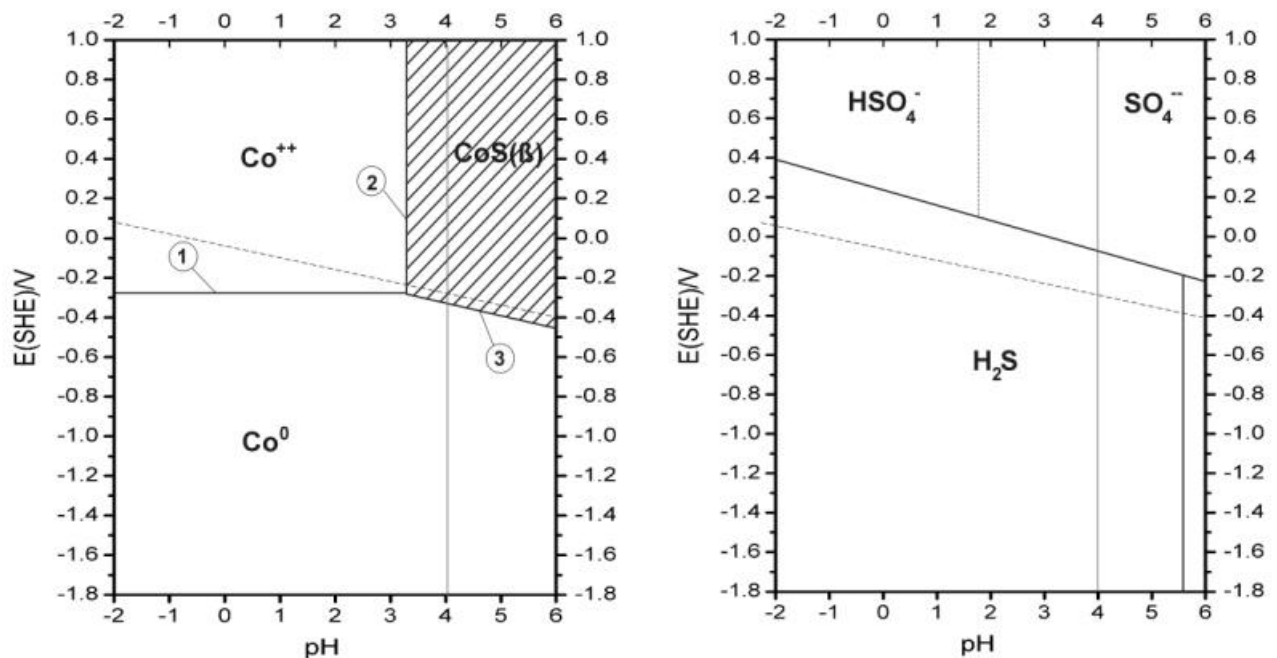
Fig. 5.1 shows a typical cyclic voltammogram of the (GC/CoS( $\beta$ )) electrode). In order to avoid hydrogen evolution, which may cause a removal of the CoS( $\beta$ ), the CV starts at 0.4V and goes in negative direction as shown in the potential program in Fig. 5.1 (small diagram). Results show that cathodic peaks  $C_1$ ,  $C_2$ , and anodic peaks  $A_1$ ,  $A_2$  appear during scanning. The corresponding peak potentials and the possible reactions according to thermodynamic equilibrium are shown in table 5.1. It should be noted that the mixture obtained on the electrode GC/CoS( $\beta$ ) contains not only CoS( $\beta$ ), but also possible SO<sub>4</sub><sup>2-</sup>, S<sup>2-</sup> and polysulphides. In order to elucidate the occurring electrochemical processes, the peaks  $C_1, C_2$  and  $A_1, A_2$  were investigated in detail.



**Figure 5.1** Cyclic voltammogram of GC/CoS( $\beta$ ) and bare GC in the free Ni solution ( $pH=4$ ,  $T=25^\circ C$ ). Scan rate  $v=1mV/s$ .

**Table 5.1** Peak potentials for C<sub>1</sub>, C<sub>2</sub>, A<sub>1</sub>, A<sub>2</sub> and possible corresponding electrochemical reactions

Peaks	Peak Potential	Possible Reactions	Equilibrium Potential	References
C <sub>1</sub>	$E = -0.25 ? -0.35\text{V}$	CoS( $\beta$ ) reduction (I)	$E^0 = -0.3 ? -0.5\text{V}$	Pourbaix diag. (Fig 5.2)
C <sub>2</sub>	$E = -0.45 ? -0.5\text{V}$	CoS( $\beta$ ) reduction (I)	$E^0 = -0.3 ? -0.5\text{V}$	Pourbaix diag. (Fig 5.2)
		$2\text{S}^{2-} = \text{S}_2^{2-} + 2\text{e}^-$ (II)	$E^0 = -0.524\text{V}$	[Bard80][Pour66]
		S <sup>2-</sup> desorption (III)	$E = -0.6\text{V}$	[Wier79]
		(i $\sim\mu\text{A}/\text{cm}^2$ )		
A <sub>1</sub>	$E = -0.1 ? 0\text{V}$	Co + H <sub>2</sub> S + H <sub>2</sub> O ? (IV)		[Nick68]
A <sub>2</sub>	$E = 0.7\text{V} ? 0.8\text{V}$	H <sub>2</sub> S + 4H <sub>2</sub> O ? (V)	$E^0 = 0.303\text{V}$	[Bard80][Pour66]
		SO <sub>4</sub> <sup>2-</sup> + 10H <sup>+</sup> + 8e <sup>-</sup>	$E^0 = 0.6 ? 0.8\text{V}$	[Wier79]

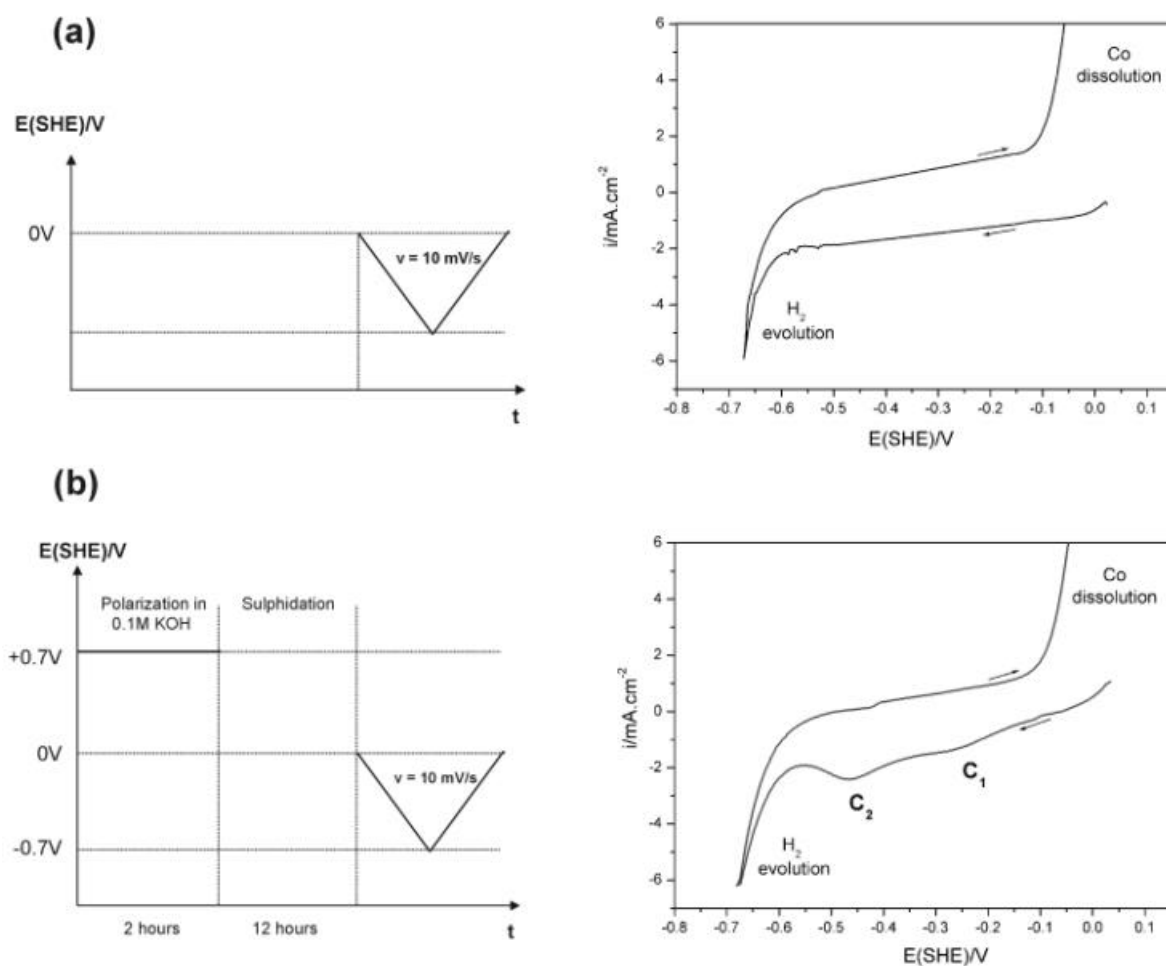
**Figure 5.2** Pourbaix diagrams of (a) CoS( $\beta$ ) and (b) S.

The establishment of the CoS( $\beta$ ) diagram is described in appendix 8.1. All experiments in this work are carried out at pH=4.

Peaks  $C_1$  and  $C_2$ 

In order to exclude  $\text{SO}_4^{2-}$ ,  $\text{S}^{2-}$  and polysulphides, which may cause additional electrochemical reactions during potential scanning, a solid  $\text{CoS}(\beta)$  electrode is produced. The preparation of the solid  $\text{CoS}(\beta)$  electrode is described in Fig. 5.3b: Co metal is polarized at 0.7V in KOH 0.1M for 2 hours, followed by an electroless sulphidation in  $\text{Na}_2\text{S}$  0.05M during 12 hours. The estimated thickness of the sulphide film is about  $100\text{\AA}$ .

Fig. 5.3 shows CVs of a reference Co metal electrode and a solid  $\text{CoS}(\beta)$  in the solution  $S_0$ . It is interesting to see that the peaks  $C_1$  and  $C_2$  are also observed at  $-0.25\text{V}$  and  $-0.45\text{V}$ , respectively. This result indicates that the peaks  $C_1$  and  $C_2$  are only related to the reduction of  $\text{CoS}(\beta)$  (cf. table 5.1).

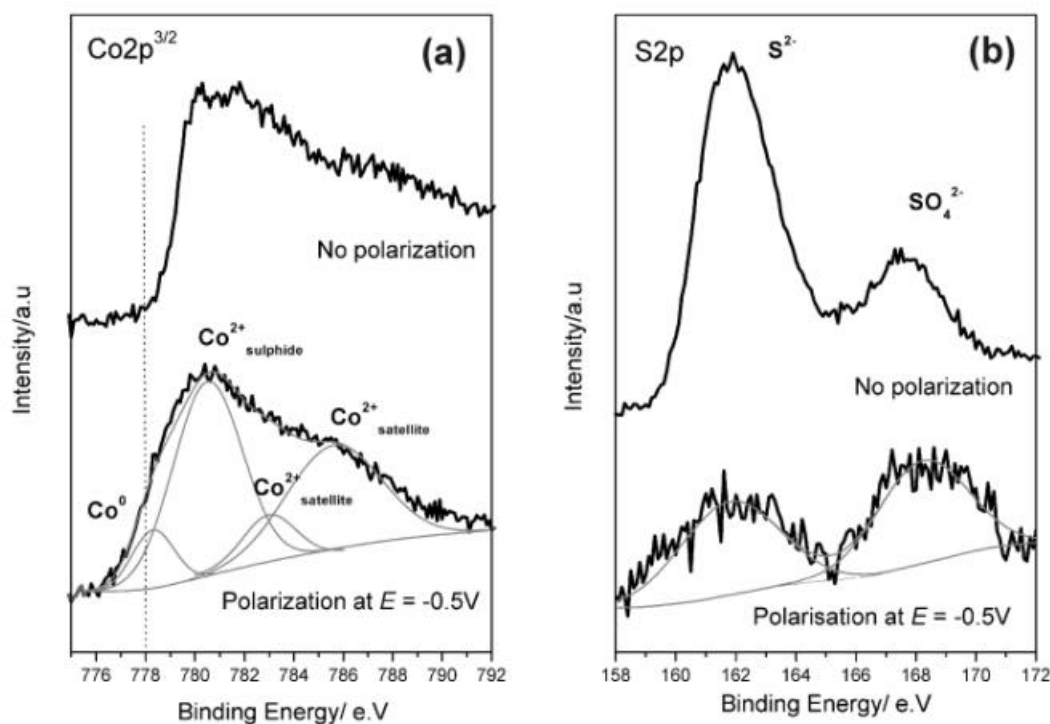
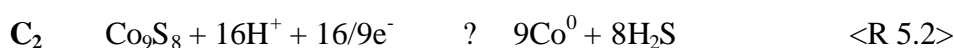
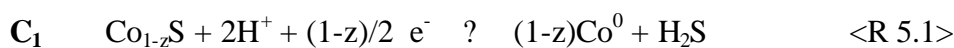


**Figure 5.3** Preparation of electrode, potential programs and cyclic voltammogram in the free Ni solution  $S_0$  (pH=4,  $T=25^\circ\text{C}$ ) of:

(a) Co-metal electrode

(b)  $\text{CoS}(\beta)$  electrode

Fig 5.4 shows XP spectra of Co2p and S2p for CoS( $\beta$ )/GC electrode before and after polarization at  $E=-0.5V$  in solution (58g/l NaCl, 30g/l  $H_3BO_3$ , pH=4)( $S_0$  without anion  $SO_4^{2-}$ ) for 5 minutes. It is interesting to note that  $Co^0$  signal is observed after polarization at  $E=-0.5V$  (Fig. 5.4), indicating that the peaks  $C_1$  and  $C_2$  correspond to the reductions of CoS( $\beta$ ) to  $Co^0$ . Meanwhile, the intensity of  $S^{2-}$  specie decreases after polarization, remarked by the increase of concentration ratios  $S^{2-}/Co$  from 0.85 (before polarization) to 5 (after polarization). This result indicates that the reductions takes place preferentially on surfaces of the CoS( $\beta$ ) clusters, where reduction product  $H_2S$  can easily diffuse into the solution. It is also interesting to mention that  $S_0$  (164eV) and  $S_n$  (163.8eV) are not observed in the XP spectra of the precipitated CoS( $\beta$ ) mixture, confirming that  $C_1$  and  $C_2$  are not related to the reactions of  $S_0$  and  $S_n$ . Bearing in mind that CoS( $\beta$ ) is a mixture of  $Co_9S_8$  and  $CoS_{1-z}$  (see chapter 2.2), the corresponding reactions are\* :



**Figure 5.4** XP detailed spectra of (a) Co and (b) S before and after polarization of GC/CoS( $\beta$ ) at  $E=-0.5V$  in the solution  $S_0$ .

\* At pH=4, the form  $H_2S$  is thermodynamically more stable than  $S^{2-}$ . See Pourbaix diagram of S [Pour63]

*Peaks A<sub>1</sub> and A<sub>2</sub>*

As shown in table 5.1, the only reaction corresponding to A<sub>1</sub> is the oxidation of Co<sup>0</sup> to Co<sup>2+</sup>. Since pH = 4 at the electrode surface and H<sub>2</sub>S may appear due to reactions C<sub>1</sub>(R 5.1) and C<sub>2</sub>(R 5.2), Co<sup>2+</sup> exists in the form of Co(OH,SH)<sub>2</sub> (CoS(?)). Thus, the reaction for A<sub>1</sub> is:

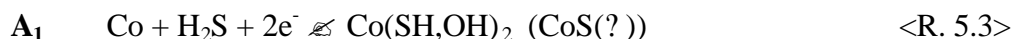


Fig. 5.5. shows cyclic voltammograms of the CoS(β)/GC for 3 cycles. The process occurring during the cyclic voltammetry can be interpreted as following: After the first cycle, a part of CoS(β) is reduced through reactions C<sub>1</sub>, C<sub>2</sub> and CoS(?) is formed through A<sub>1</sub>. It should be mentioned that only about 15% CoS(β) is reduced after the first cycle (calculated from charges of C<sub>1</sub> and C<sub>2</sub>)<sup>\*</sup>. The cathodic reactions in the second cycle, therefore, are the reductions of the mixture of CoS(?) and the rest CoS(β). The curve shows that the reduction of CoS(?) takes place at E = -0.3V ~ -0.35 (peak C<sub>1</sub>'), overlapping the peak C<sub>1</sub>. As a result, the intensity of the overlapping peak (C<sub>1</sub>+C<sub>1</sub>') is higher than that of C<sub>2</sub> (i<sub>C<sub>1</sub>+C<sub>1</sub>' > i<sub>C<sub>2</sub>), in contrast to the first cycle with i<sub>C<sub>1</sub>' < i<sub>C<sub>2</sub>. In the third cycle, the peak C<sub>2</sub> is not observed any more, since the rest of CoS(β) is reduced completely. It should be mentioned that H<sub>2</sub> evolution after each cycle causes a partial removal of the CoS(β) or CoS(β)/Co<sup>0</sup> clusters, leading to a lower charge q<sub>A<sub>1</sub></sub> comparing with total reduction charge q<sub>C<sub>1</sub>+C<sub>1</sub>'</sub>, and the decrease of q<sub>C<sub>1</sub>+C<sub>1</sub>'</sub> after each cycle. As shown in Fig. 5.6, the cobalt sulphide mixture that remains after the cyclic voltametric experiment is clearly less than in the original CoS(β)/GC electrode.</sub></sub></sub></sub>

\* Calculation of the amount of reacted CoS(β):

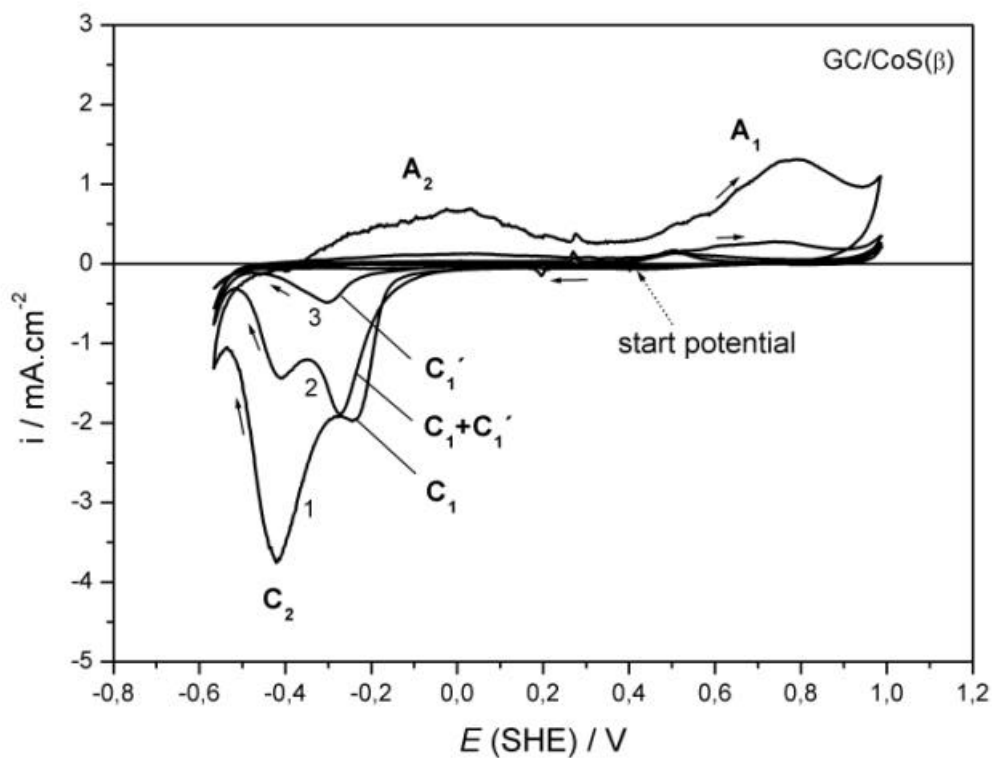
The total amount of CoS(β) on GC:  $n_{total} = C_{\text{Co}^{2+}(\text{complex})} \cdot V_{\text{Co}^{2+}(\text{complex})} = 5 \cdot 10^{-2} \text{ (mol/l)} \cdot 10^{-3} \text{ (l)} = 5 \cdot 10^{-5} \text{ mol}$   
 $C_{\text{Co}^{2+}(\text{complex})}$  and  $V_{\text{Co}^{2+}(\text{complex})}$  are concentration and volume of the Co<sup>2+</sup>-complex for preparation of GC/CoS(β) electrode (cf. 3.2.1.2)

The amount of reduced CoS(β):  $n_{red} = A \frac{q_{total}}{F} = A \frac{q_1 + q_2}{F} = 7.4 \cdot 10^{-6} \text{ mol}$

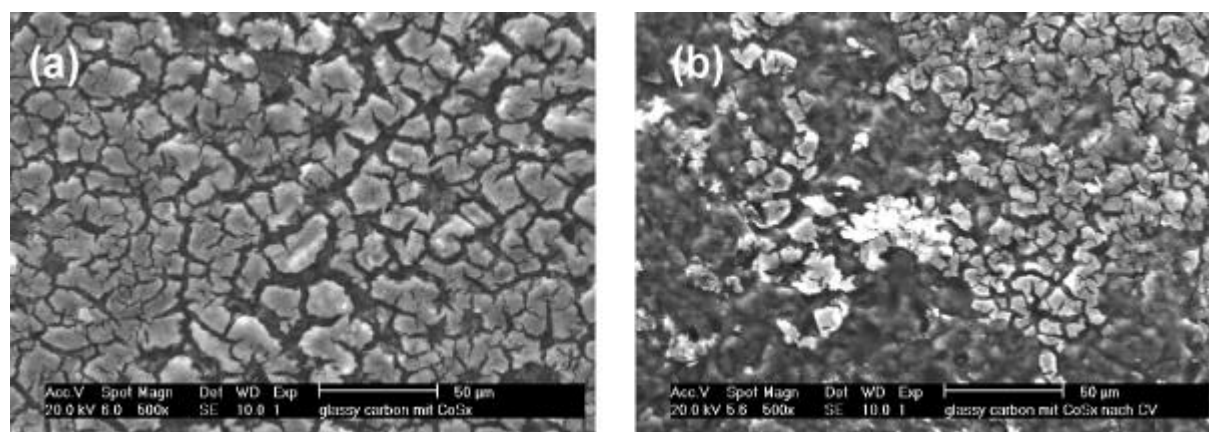
where A is the electrode area (A = 0.785 cm<sup>2</sup>), q<sub>1</sub>, q<sub>2</sub> are the reduction charges of reduction peaks C<sub>1</sub> and C<sub>2</sub> (q<sub>1</sub> = 250 mC/cm<sup>2</sup>, q<sub>2</sub> = 667 mC/cm<sup>2</sup>), F is Faradays constant (F = 96500 C/mol).

Percent of reacted CoS(β)  $\frac{n_{red}}{n_{total}} \approx 15\%$



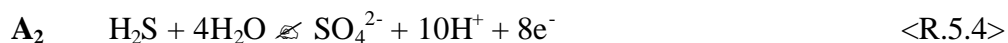


**Figure 5.5** Cyclic voltammogram of GC/CoS( $\beta$ ) in the Ni free solution (pH=4, T=25°C). Scan rate  $v=1\text{mV/s}$ .

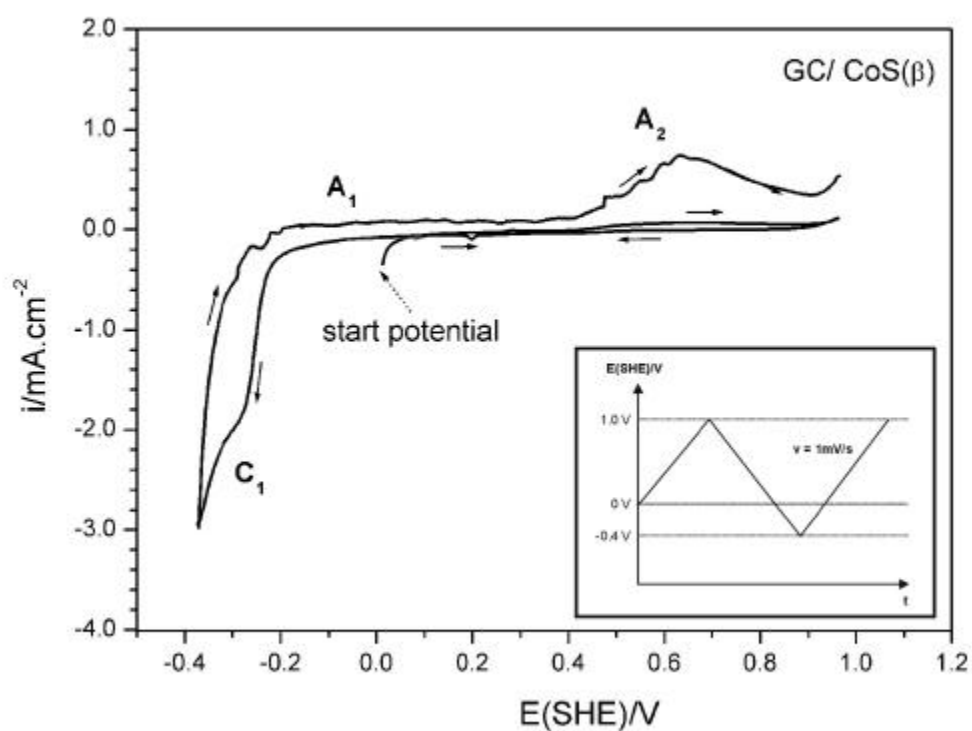


**Figure 5.6** SEM images of GC/CoS( $\beta$ ) (a) before and (b) after cyclic voltammetry

The possible reaction for  $A_2$  is :



In order to study the relation between  $A_2$  and the reduction reactions  $C_1$ ,  $C_2$ , a cyclic voltammetric experiment is programmed as followed: unlike the CVs presented before, in this measurement, potential starts at 0V and the first scan goes in the increasing potential direction (see potential program in Fig. 5.7). It is interesting to note that during the first scan from 0.4 to 1.0V, the peak  $A_2$  is not observed. However, after the reduction reaction  $C_1$  takes place in the second cycle,  $A_2$  appears again. This behaviour indicates that the reaction  $A_2$  consumes products of the reaction  $C_1$  e.g. reaction  $C_1$  occurring in the forward scan supplies  $H_2S$ , which will be oxidized at potential  $E=0.6$  to  $0.8V$  through reaction  $A_2$  in the back scan.



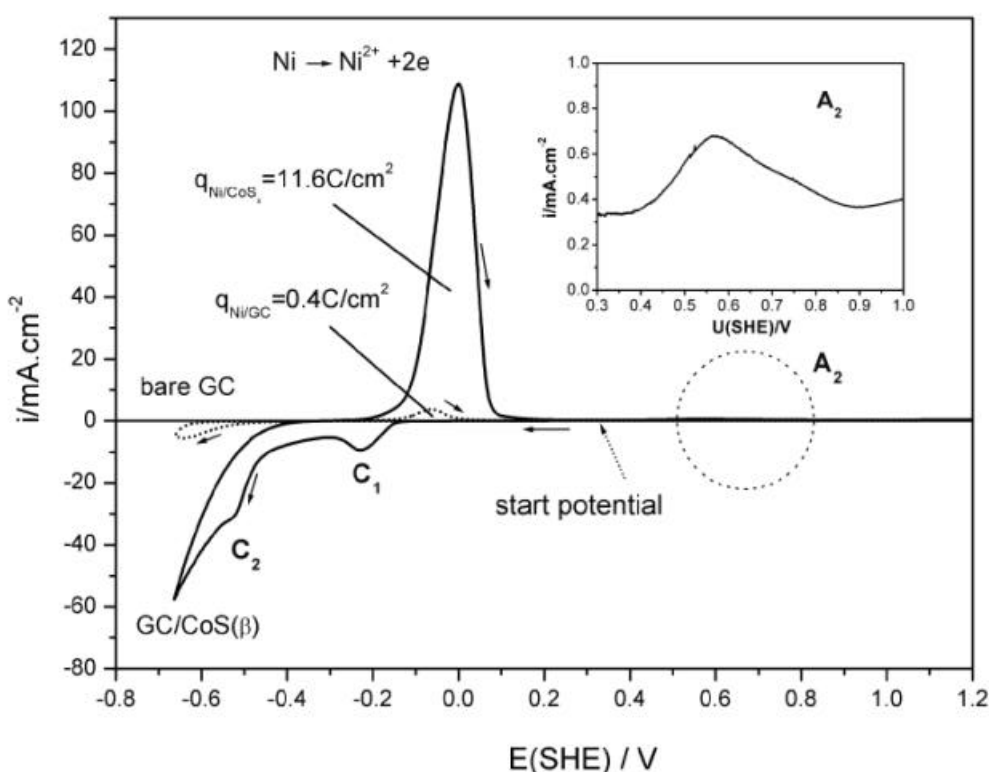
**Figure 5.7** Cyclic voltammogram of GC/CoS( $\beta$ ) in the Ni free solution. The potential program is shown in the small figure.

### 5.1.2. Electrochemistry of CoS( $\beta$ ) in the Ni containing solution

Fig. 5.8 presents cyclic voltammograms of the bare GC and GC/CoS( $\beta$ ) electrodes in the electrolyte containing Ni with the same potential program shown in Fig.5.1. The cyclic voltammogram on bare GC shows that the Ni deposition occurs at  $E < -0.25$  V and a small dissolution peak appears in the reverse scan, corresponding to the small amount of deposited Ni. On the CV curve of the GC/CoS( $\beta$ ) electrode, the reduction peaks  $C_1$  and  $C_2$  can be observed in the forward scan, similarly to the experiment in the Ni free electrolyte. For the reverse scan, a dissolution peak of Ni(Co) appears at  $-0.1$  V and  $A_2$  is also observed, indicating that  $H_2S$  is trapped together with the reduced CoS( $\beta$ ) under the Ni cap during the metal deposition. It is very interesting to note that, compared to the Ni dissolution charge on bare GC, the Ni dissolution charge for GC/CoS( $\beta$ ) is much higher than that for bare GC

( $\frac{q_{GC/CoS(\beta)}^{Ni}}{q_{GC}^{Ni}} = \frac{11.6}{0.4} = 29$ ). Plausible explanations for the extraordinary high deposition rate are:

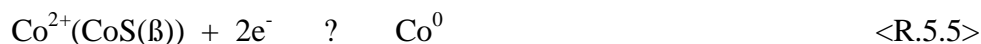
(i) the reduction reactions  $C_1$  (R 5.1),  $C_2$  (R 5.2) accelerate the charge transfer of the parallel Ni deposition on the freshly formed Co metal. (ii) high interaction between Ni and Co substrate. The high current density due to this interaction is also observed in other study, in which Ni is deposited onto Co [Vall99].



**Figure 5.8** Cyclic voltammogram of GC/CoS( $\beta$ ) and bare GC in the Ni containing solution. Scan rate  $v=1mV/s$ .

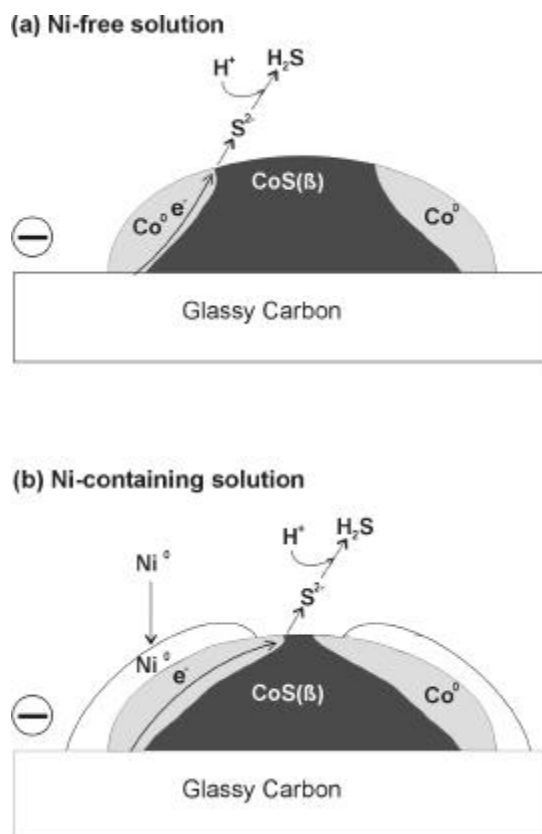
Thus, the electrochemical processes on a CoS( $\beta$ ) cluster can be summarized as follow:

In the Ni-free solution, two reactions occur (Fig. 5.9a)



Both reaction take place at border Co<sup>0</sup>/CoS( $\beta$ )/electrolyte, where the S<sup>2-</sup> combines with proton and the product H<sub>2</sub>S diffuses easily into the solution. It should be noted that the electrons, which supplied from the negative polarized GC electrode, go through the Co<sup>0</sup> phase to the border Co<sup>0</sup>/CoS( $\beta$ )/electrolyte due to the low conductivity of the CoS( $\beta$ ) phase. As a result, Co<sup>0</sup> domains are formed preferentially on the surface of the cluster. In the Ni-containing solution (Fig. 5.9b), on one hand, the Ni deposition reaction is catalyzed by the reduction of CoS( $\beta$ ), and on the other hand, it results a conductive layer on the Co<sup>0</sup> domain and enhances the further reduction of CoS( $\beta$ ).

On insulating polymer surfaces, the source of electron is from a contact tip and the electrons transfer through the system CoS( $\beta$ )/deposited Ni for the reduction and metal deposition on the next CoS( $\beta$ ) clusters. The processes on the activated polymer surfaces will be studied in the next sections.



**Figure 5.9** Electrochemical processes on a CoS( $\beta$ ) cluster in  
(a) Ni-free solution      (b) Ni-containing solution

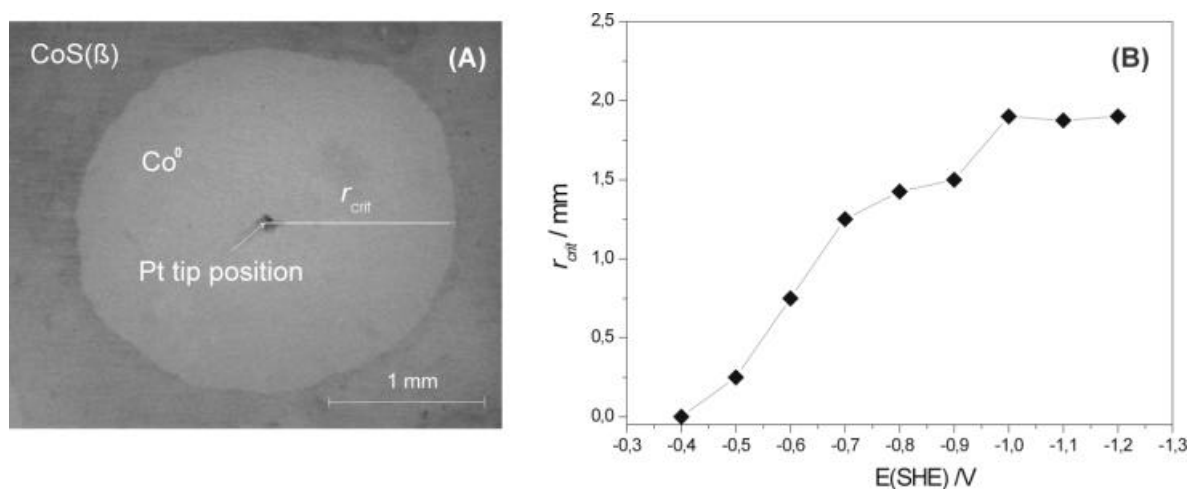
## 5.2. Kinetics of metal deposition

### 5.2.1. Formation of Ni layer

#### 5.2.1.1. Electrochemical processes during metal deposition

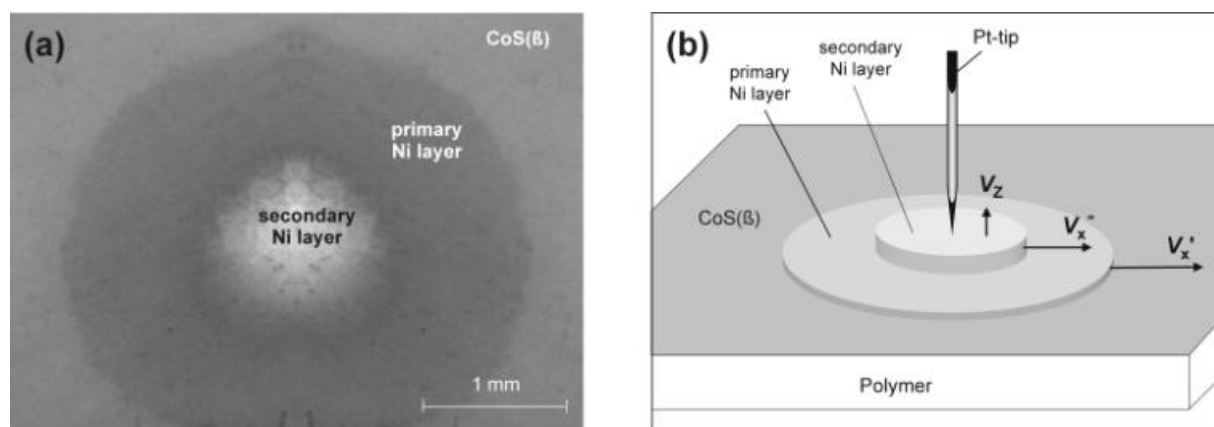
Fig. 5.10 shows an activated ABS substrate ( $\theta=86\%$ ) after polarization at  $E=-0.9\text{V}$  in the Ni free solution ( $S_0$ ) using a Pt contact tip. A very interesting phenomenon is observed: the area near the Pt tip changes to a brighter colour, which is attributed to the reduction of  $\text{CoS}(\beta)$  to  $\text{Co}^0$ . The  $\text{Co}^0$  area propagates until it achieves a maximum radius ( $r_{crit}$ ), which is dependent on polarization potentials at the contact tip. The influence of  $r_{crit}$  on the polarization potential is shown in Fig. 5.9b.

It should be noted that this phenomenon is only observed with relative high coverage  $\theta$  of  $\text{CoS}(\beta)$  ( $\theta>84\%$ ). The reduction in a certain zone cannot be explained by the potential distribution on the  $\text{CoS}(\beta)$  layer since the conductivity produced by the 3D contact among the clusters is very low (cf. 5.2.1). It is suggested that the reduction on a  $\text{CoS}(\beta)$  increases its conductivity and thereby enhance the supply of electrons for the reduction of the neighbour clusters. This chain reaction will stop at a certain distance, at which clusters cannot receive electrons supplied from the contact tip and conducted through  $\text{CoS}(\beta)$  zone.

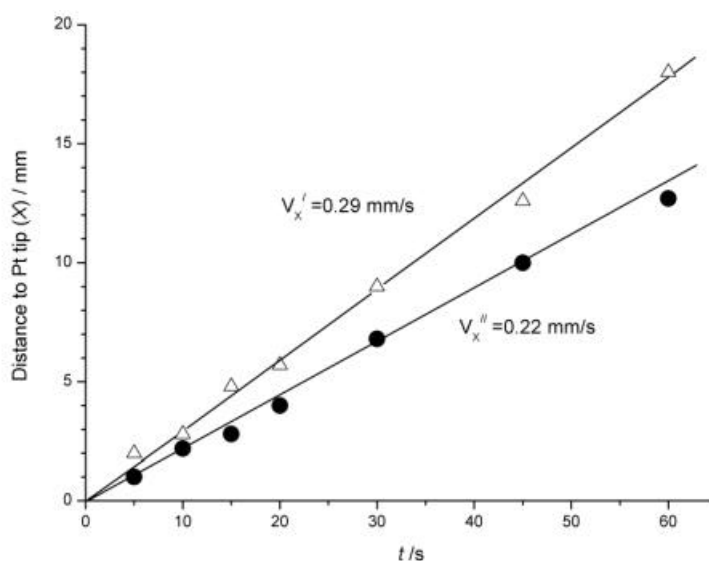


**Figure 5.10** (a) Reduction of  $\text{CoS}(\beta)$ /ABS ( $\theta=86\%$ ) in the solution  $S_0$ . (polarization potential  $E=-0.9\text{V}$ ,  $t = 3\text{min}$ ).  
 (b) Influence of polarization potential on critical radius  $r_{crit}$ .

Meanwhile, in the Ni-containing electrolyte, the Ni deposition takes place with the propagation of the deposited Ni layer. Two layers are generally formed during the propagation: a primary layer and a secondary layer with different propagation rates (Fig. 5.11). The changes of the distances to the Pt tip from the edge of the primary and of the secondary layers during propagation were recorded (Fig. 5.12). Results show that both distances increase linearly with time after the first 60 seconds, indicating that the propagations of the primary and the secondary layers take place with constant rates  $V_x'$  and  $V_x''$ , respectively. It should be noted, that with extended deposition ( $t > 180$ s), propagation rates of the primary and the secondary layers are no longer constant and decrease with time. The reason may be related to the increasing potential drop when the propagation proceeds.

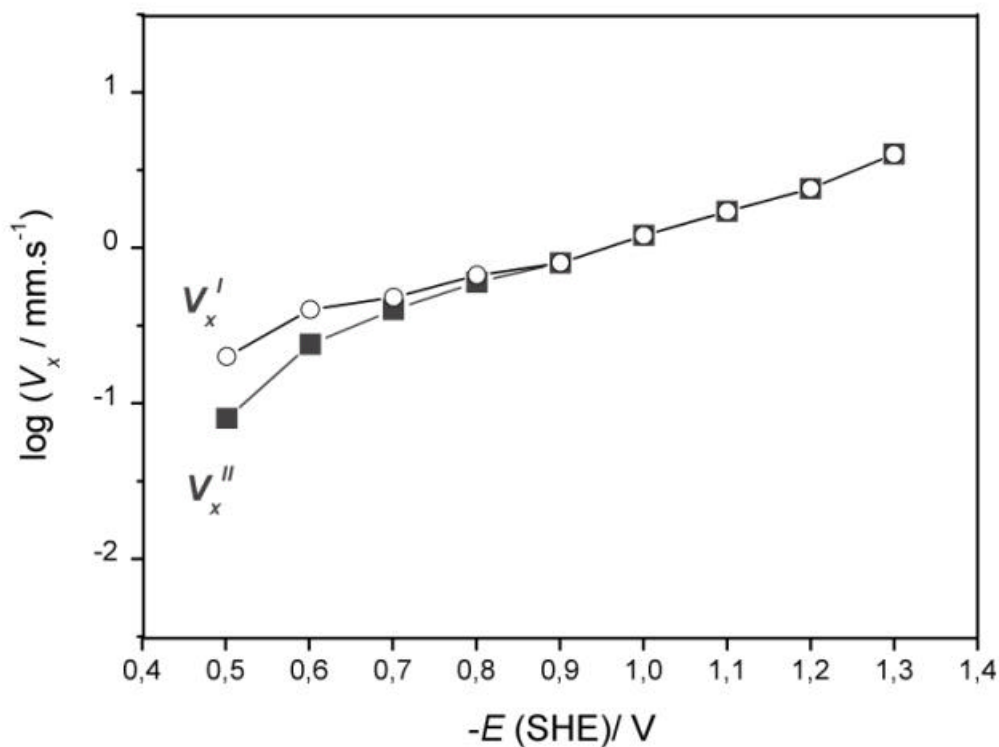


**Figure 5.11** (a) Micrograph of the primary and the secondary layer during metal deposition ( $E = -0.6$ V,  $t = 5$ s).  
(b) Schematic description of the Ni layer propagations.

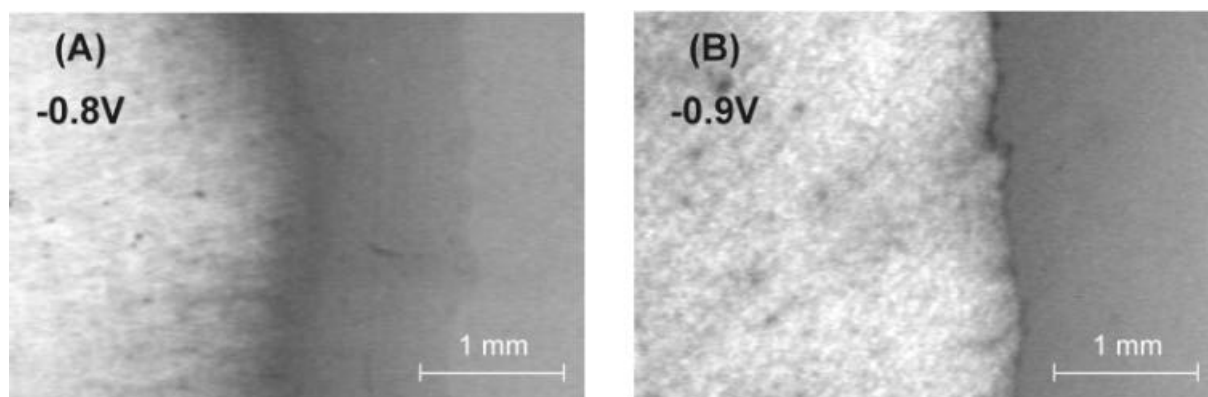


**Figure 5.12** Change of the distance from Pt tip to the end of the primary and the secondary layer during metal deposition.

Fig. 5.13 shows the influence of the potential  $E$  on  $V_x'$  and  $V_x''$ . Results show that at  $E > -0.8\text{V}$ , the rate  $V_x'$  is larger than  $V_x''$  and both layers can be observed in the micrograph (Fig. 5.14a), whereas  $V_x'$  is equal to  $V_x''$  at  $E < -0.8\text{V}$ , leading to the complete covering of the secondary layer on the primary sublayer during propagation and only the secondary layer is observed in the microscope (Fig. 5.14b).



**Figure 5.13** Influence of the metallization potential on the propagation rates of the primary layer ( $V_x'$ ), the secondary layer ( $V_x''$ ).

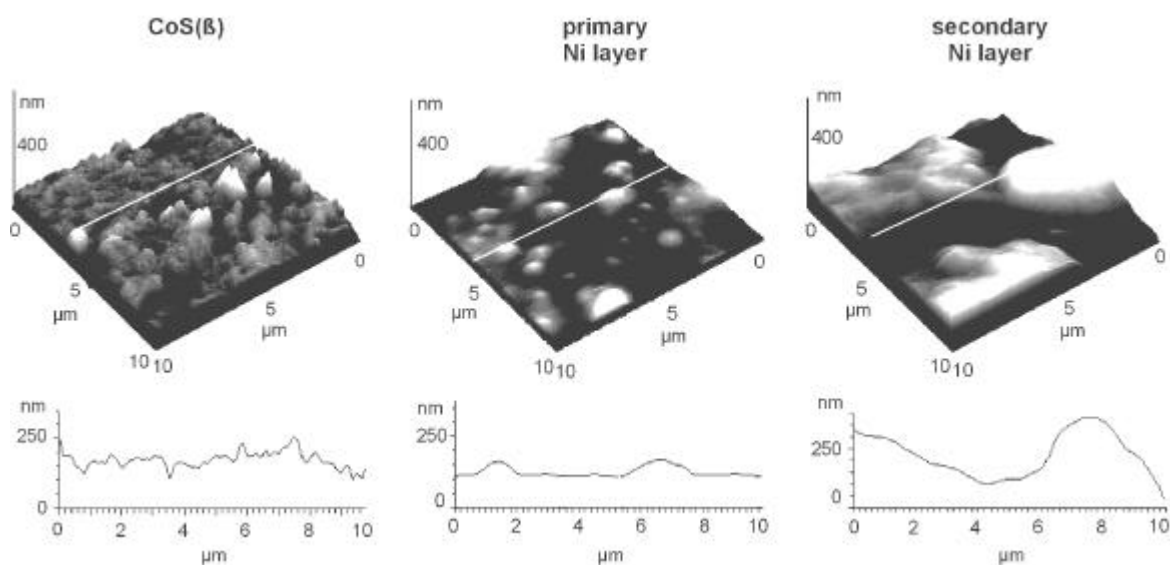


**Figure 5.14** Etches of electrodeposited Ni layers after 20s and  
(a)  $-0.8\text{V}$  (b)  $-0.9\text{V}$

### 5.2.1.2. Characterization of the primary and the secondary layer

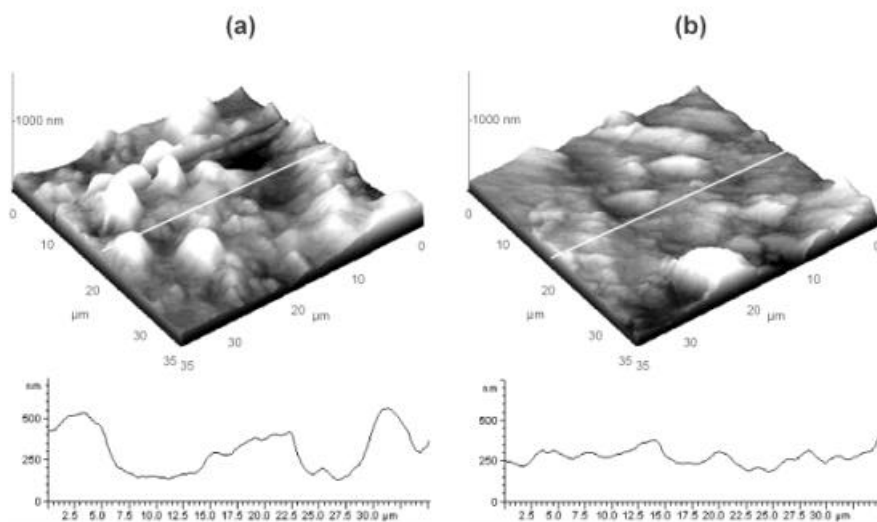
#### AFM

Fig. 5.15 shows typical AFM topographies and line scans of the activated area, the primary layer and secondary layer obtained after 60s deposition at  $E = -0.6V$ . CoS( $\beta$ ) clusters with rough mean square roughness  $R_{rms}^{CoS(\beta)}$  of 25 nm can be observed on the activated surface. The primary Ni-layer shows hemispheres with a height of 10 to 50nm and a diameter of 0.5 to 2 $\mu$ m. The secondary Ni layer owns a repetition topography of the primary one with a higher roughness ( $R'_{rms} ? 45nm$ ,  $R''_{rms} ? 160nm$ ), but lower density of hemispheres. This repetition behaviour is expected, since the deposition of the secondary Ni layer follows the mechanism of electrodeposition on a metal substrate. In absence of additives, the morphological repetition of substrates for electrodeposited metal layers is well-known [Bud96]. It should be mentioned that the rough surface of the secondary layer due to the repetition morphology of the primary layer can be flattened by the use of brightener additives. Fig 5.16 shows the two Ni layers deposited on an ABS substrate in electrolytes without additives and with brightener additives. The roughness of the surface in the additive containing solution is decreased obviously and a smoother surface is obtained as a result.



**Figure 5.15** AFM images of the activated surface, the primary and the secondary Ni layers. The Ni layer is obtained after deposition with  $E = -0.6V$  and  $t = 60s$ .

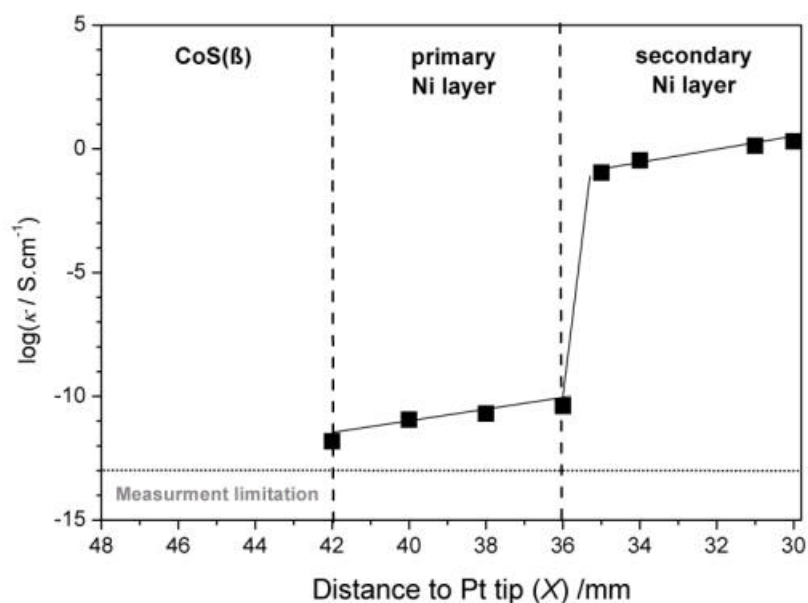




**Figure 5.16** AFM images of Ni layers deposited on activated ABS substrates (coverage  $\approx 49\%$ ) at  $E = -0.6\text{V}$  and  $t = 120\text{s}$  from electrolytes (a) without additives (b) with brightener additives Enthone-X5 (Thiourea).

### Conductivity measurement

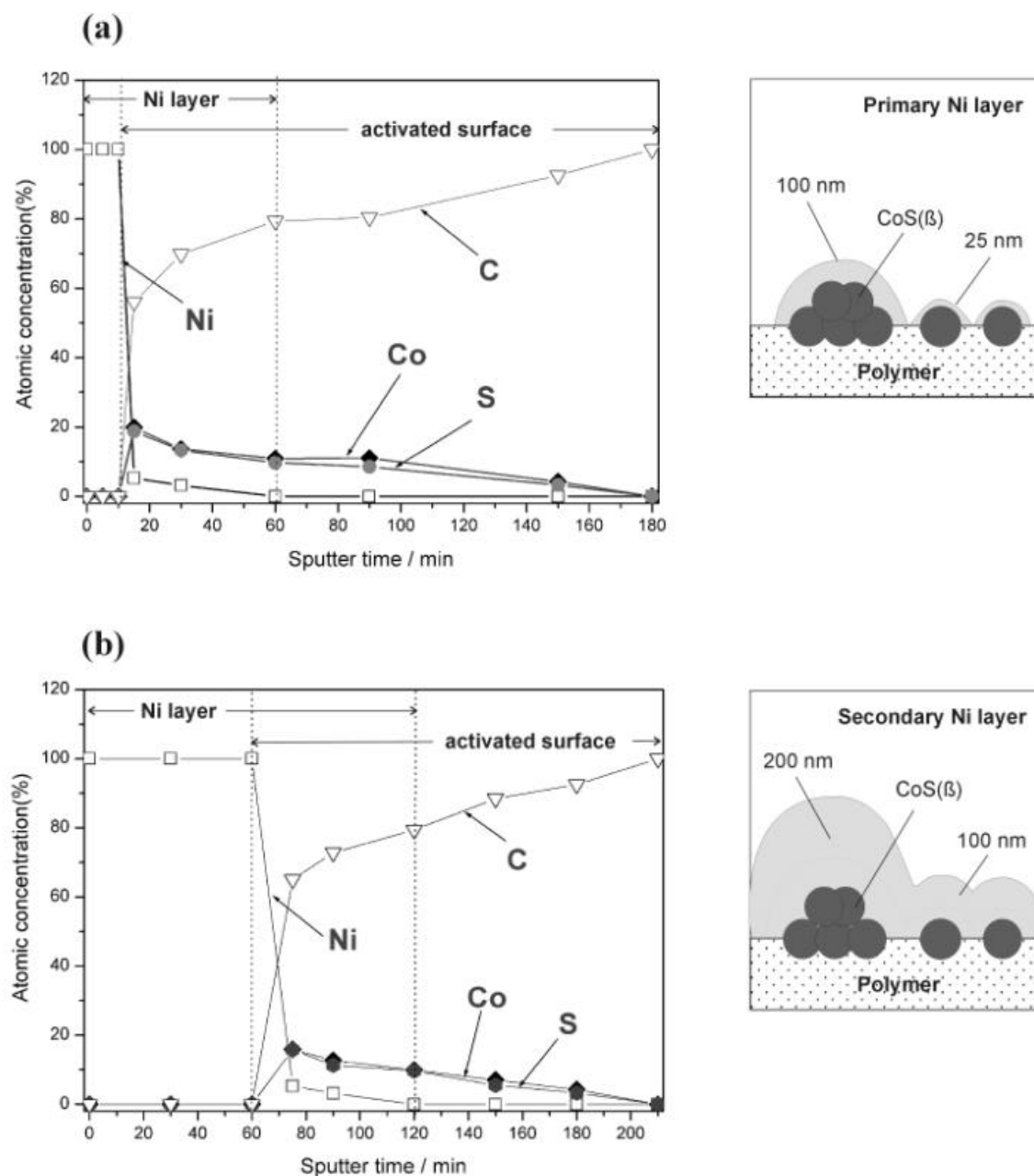
Fig. 5.17 shows the conductivity measured by 4-point method (cf. section 3.4) of the three zones: activated, primary layer, secondary layer. The conductivity of the secondary Ni layers is obviously higher than that of the primary ( $\sigma \approx 10^8 \text{--} 10^{10}$ ). This result indicates that the secondary Ni layer is remarkably thicker than the primary one. The conductivity of the activated zone cannot be measured due to the fact that  $\text{CoS}(\beta)$  is in the form of discrete clusters, but not as a continuous layer on the surface.



**Figure 5.17** Conductivities of the activated surface, the primary and the secondary Ni layers. The Ni layer is obtained after deposition with  $E = -0.6\text{V}$  and  $t = 60\text{s}$ .

*XPS sputter profile*

The XPS sputter profiles of the primary and secondary Ni layers are shown in Fig. 5.18. It should be noted that during sputtering, the Ni layer and the polymer surface are etched with different rates (average sputter rates of the Ni layer  $v_{Ni} = 1.6$  nm/min and of the polymer  $v_{Ni} = 6$  nm/min)[Chan92]. On the unsputtered surface of the primary layer (Fig. 5.18a), the concentrations of Co and S are zero, indicating that the primary Ni layer is a continuous layer and the activated surface underneath this layer is not exposed. The first Co and S signals are recorded after 15 minutes of sputtering, corresponding to the removal of the thinnest part with thickness of about 25 nm. It is interesting to note that during the first 15-60 minutes sputtering, all Ni, Co and S signals appear with concentrations decreasing gradually with time. This result indicates that the thickness of the primary layer is not evenly distributed e.g. thinner parts were etched away faster. After sputtering for 60 minutes, Ni is completely removed, corresponding to a thickness of about 100nm. The corresponding thickness of the primary layer is therefore in the range of about 25 to 100 nm (Fig. 5.18a). Further sputtering yields the decreasing of Co and S concentrations until they vanish after 180 minutes. Fig. 5.17b shows the sputter profile of the secondary layer. The same sputter behaviour of the primary layer is also observed for the secondary layer. However, the time for the appearance of the first Co signal is much higher (after 60 minutes sputter), corresponding to the higher thickness range of 100 to 200 nm (Fig. 5.18b).



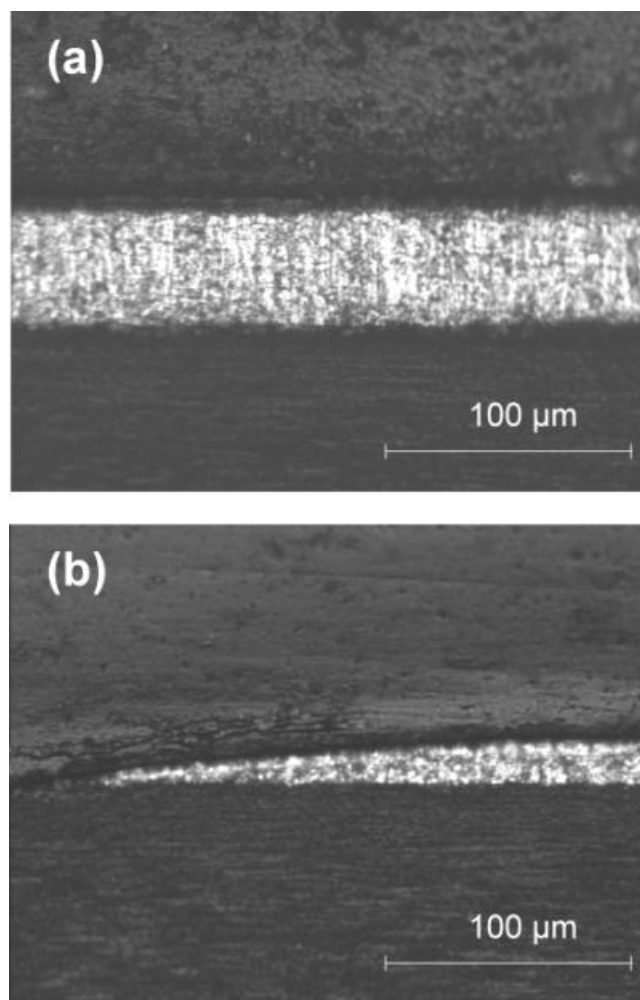
**Figure 5.18** XPS sputter profile of (a) the primary layer and (b) the secondary layer. The Ni layer is obtained after deposition at  $E = -0.6V$  and  $t = 60s$ .

### Cross-section

Typical cross-sections of deposited Ni layers on an activated ABS surfaces are shown in Fig. 5.19. At  $E = -0.6V$ , the propagation of the secondary layer occurs very fast, resulting in an even thickness distribution of the Ni layer, which is required for metallization of insulating microstructures (Fig 5.19a). It is interesting to note that the Ni layer has a columnar structure, which is also observed in Ni deposited on a metal substrate in absence of additives [Bren63][Bud96]. This indicates that after formations of primary and secondary at the first

stage of deposition, potential drop on the deposited layer can be neglected and deposition occurs practically following the mechanism of deposition on a metal substrate.

However, an even distribution of thickness is not always the case. At low degree of activation ( $\alpha \approx 40\%$ ) and  $E > -0.6V$ , the lateral propagation can stop after a certain time. Thereafter, thickness grows only in normal direction and is influenced by the conductivity of the first primary layer. As a result, the thickness decreases with distance from the contact (Fig 5.19b). Thus, for microstructured metallization, the deposition potential  $E$  and activation  $\alpha$  should be optimized in order to avoid the stoppage of propagation and to obtain the metal microstructures with an even thickness.



**Figure 5.19** (a) even thickness distribution of an electrodeposited Ni layer obtained at  $E = -0.6V$ ,  $t = 120 \text{ min}$  ( $\alpha = 49\%$ ).  
(b) thickness profile obtained on surface low coverage of  $\text{CoS}(\beta)$  ( $\alpha \approx 40\%$ ) at  $E = -0.5V$ ,  $t = 120 \text{ min}$  (propagation stops).

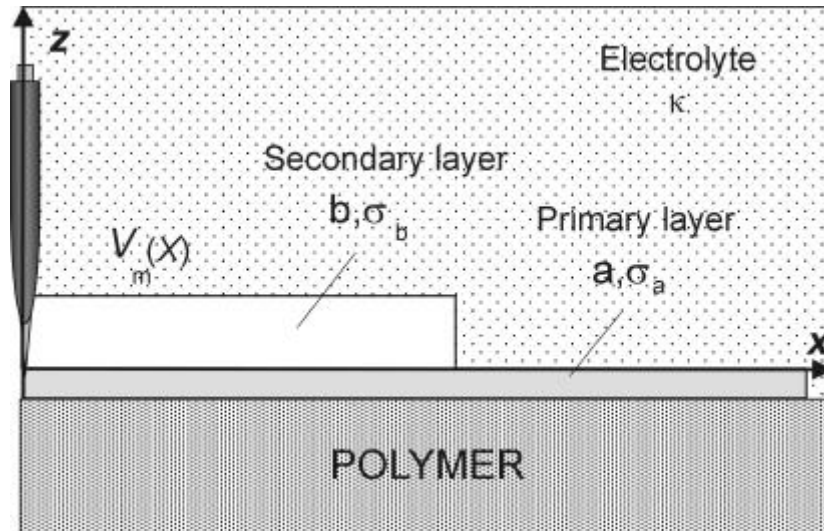
### 5.2.1.3. Current and thickness distributions on the primary layer

As shown in section 5.2.1.2, at the first period, metal deposition on an activated surface takes place by the formation of a low conductivity primary layer. The secondary layer is formed with a lateral propagation on the primary layer. The first aim of this chapter is to calculate the current and thickness evolutions of the secondary layer during metal deposition, considering the influence of conductivity and thickness of the primary layer. The following question will be answered: do the current and thickness distributions cause the propagation phenomenon?

#### *Dimensionless Formulation*

The physical model for calculation is described in Fig. 5.20. The parameters of the model are summarized as follows:

<b>Primary layer</b>	Thickness	$a$
	Conductivity	$\sigma_a$
<b>Secondary layer</b>	Thickness	$b(x,t)$
	Average thickness	$b_{avg}(x) = \frac{1}{t} \int_0^t b(x,t) dt$
	Conductivity	$\sigma_b(x,t)$
<b>Solution</b>	Conductivity	$\sigma_s$
<b>Dimension</b>	Coordinate	$x,y,z$
	Length of the primary layer	$L$
<b>Current</b>	Current at the metal surface)	$i_m(x,t)$
	Current through solution	$i_s(x,y,t) = \text{const}$
<b>Potential</b>	Potential at the metal surface	$\phi_m(x,t)$
	Potential at contact tip (or deposition potential)	$\phi_m(0,t)$
	Nernst equilibrium potential of Ni	$\phi_0$
	Overpotential	$\eta(x,t) = \phi_m(x,t) - \phi_0$



**Figure 5.20** Sketch of the physical model of an electrodeposition on activated polymer surface.

*Dimensionless parameters*

Dimensionless coordinate

$$X \ ? \ x/L \tag{5.1}$$

$$Z \ ? \ z/L \tag{5.2}$$

Dimensionless potential at metal surface and overpotential

$$V_m \ ? \ \frac{f_m}{RT/nF} \tag{5.3}$$

$$H \ ? \ \frac{?}{RT/nF} \tag{5.4}$$

Dimensionless current density and deposit thickness

$$I \ ? \ \frac{i_m}{i_s} \tag{5.5}$$

$$B \ ? \ \frac{b(x,t)s_b}{as_a} \tag{5.6}$$

Dimensionless time

$$? \ ? \ \frac{b_{avg}(x,t)s_b}{as_a} \quad (\text{with } b_{avg}(x,t) \ ? \ \int_0^t b(x,t)dt) \tag{5.7}$$

Dimensionless resistance of the primary layer

$$R_0 \ ? \ \frac{1/as_a}{1/kL} \ ? \ \frac{kL}{as_a} \tag{5.8}$$

Dimensionless resistance of the metal layer

$$R(x, t) = \frac{1 / (a s_a + b_{avg}(x, t) s_b)}{1 / kL} = \frac{kL}{a s_a + b_{avg}(x, t) s_b} \quad (5.9)$$

From (5.11) and (5.12),

$$R(x, t) = \frac{R_0}{1 + \dots} \quad (5.10)$$

Deposit thickness

$$B(X, \dots) = \int_0^{\dots} I dt \quad (5.11)$$

*Primary distribution*

The primary current distribution, which is the current distribution at the beginning with a uniform conductance of the primary layer, can be calculated following the method described by Landolt [Matl99]. For the high-resistance limit, a sharp rise of in the local current density associated with the ohmic drop in the metal phase is produced in a region of characteristic dimensionless length  $1/R$  near the contact tip. To emphasize the importance of this region, a stretched cathode length variable can be defined as follows:

$$\dots = RX \quad (5.12)$$

The current distribution is given by a function:

$$\frac{I}{R} = \frac{2}{\dots} g(\dots) \quad (5.13)$$

where  $g(\dots)$  is the auxiliary Fourier intergral function. The numerical espression of  $g(\dots)$  is given in reference [Matl99]. The plot of the function  $g(\dots)$  is shown in Fig. 5.21.

From the equation (5.16) ,the following approximate expression can be employed:

$$I = (1 + e) \frac{2}{\dots} R g(\dots) \quad (5.14)$$

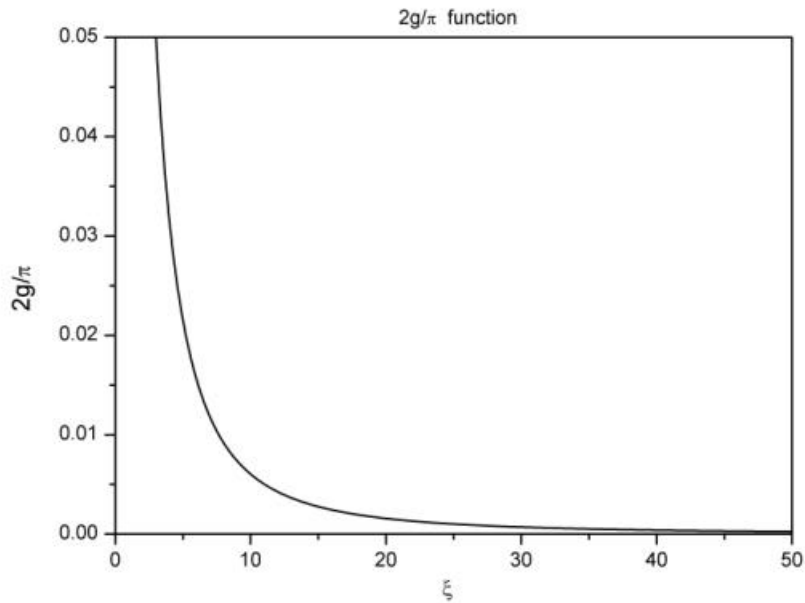
where the scale factor  $(1+x)$  is defined as follows

$$(1 + e) = \frac{\dots}{R} \int_0^{\dots} 2 g(\dots) d\dots \quad (5.15)$$

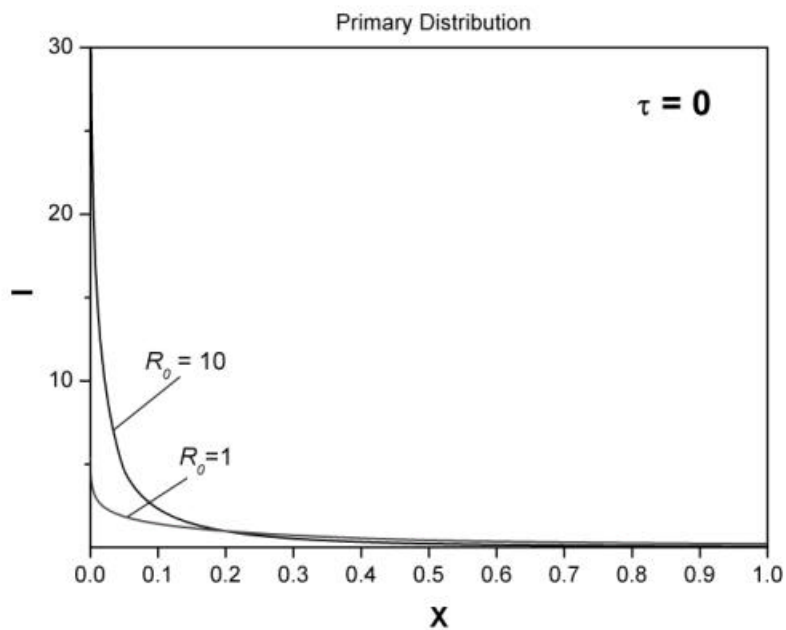
and for  $R > 5$

$$e^{-\xi} \frac{2}{\sqrt{R} \sqrt{2}} \tag{5.16}$$

For  $R = 1$ , the approximate formula described above provides a reliable estimate of the current distribution, particularly near the contact tip. The calculated primary current distributions on substrates with  $R_0=1$  and  $R_0=10$  are shown in Fig. 5.22.



**Figure 5.21** Function  $2g/\pi$  for use in estimating current distributions [Matl99].



**Figure 5.22** Primary current distributions ( $\tau=0$ ) on the primary layer with resistances  $R_0 = 1$  and  $R_0 = 10$ .



*Growth of the electrodeposited layer*

At the beginning, the conductance of the substrate is a minimum  $a^?_a(b(x)=0)$ , and the current distribution follows the primary distributions described above. As deposition proceeds, the growing deposits provide additional conductance and thickness, leading to a new current distribution. The growth of thickness and corresponding changes of current distribution under potentiostatic conditions will be calculated using dimensionless parameters.

The algorithm for the numerical calculation of  $I, B$  at time  $t$  is described below:

*Algorithm*

For a positions  $X = \{0; 0.02; 0.04; 0.06; 0.08; 0.1; 0.2; 0.3; 0.4; 0.5; 0.6; 0.7; 0.8; 0.9; 1\}$

At time  $t_n$

$$t_n = t_{n-1} + \Delta t \quad (\Delta t = 0.1)$$

Current  $I_n = \exp[0.5 * H_n(X)] / \exp[-0.5 * H_n(X)]$  (Buttler-Volmer)  
(assumption  $\alpha = 0.5$ )

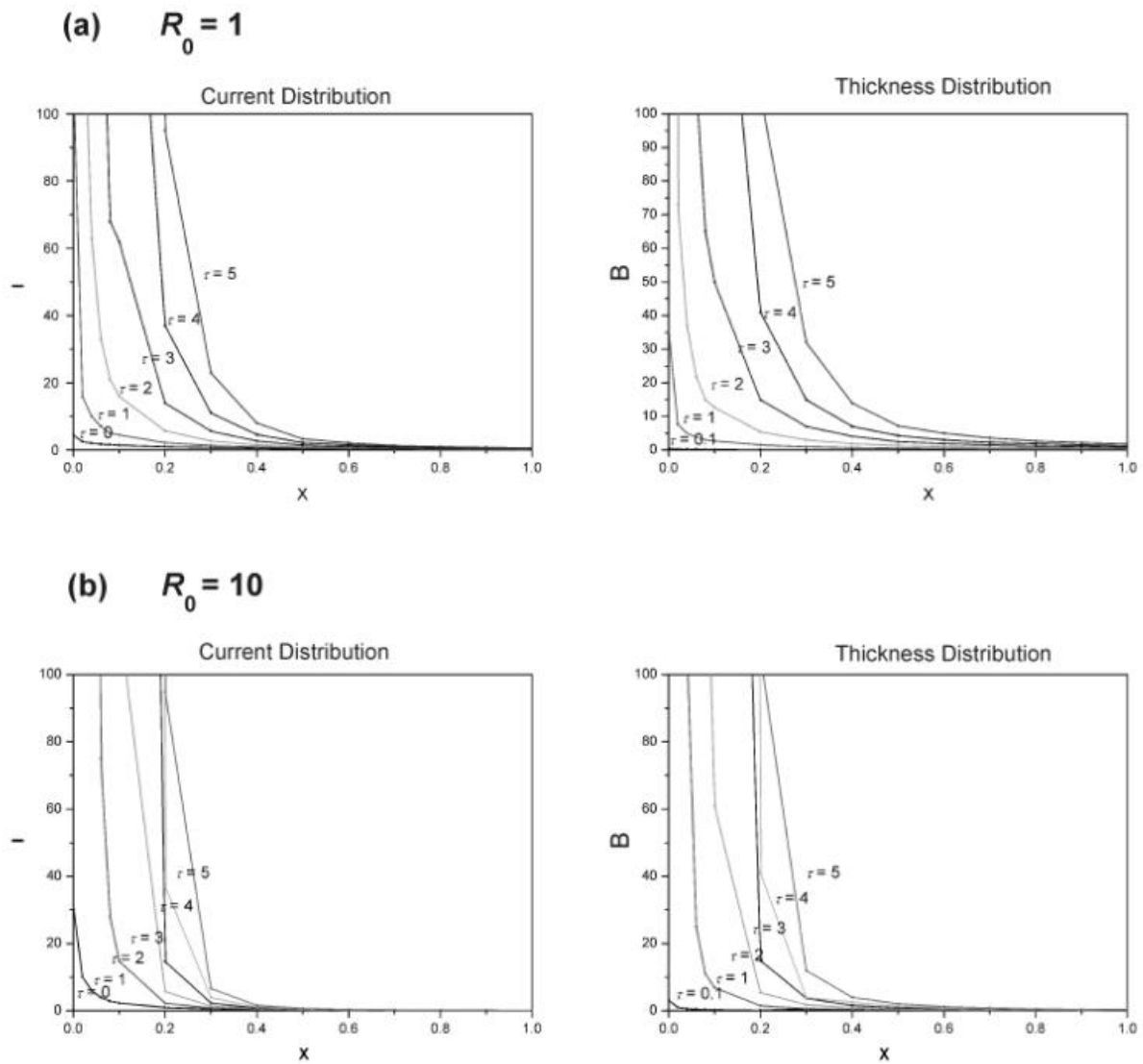
$$H_n = V_n - V_0$$

$$\text{with } V_n(X) = V_{n-1}(X) + R_{n-1}(X) \cdot I_{n-1}(X) \quad (\text{Ohm's law})$$

Thickness  $B_n(X) = B_{n-1}(X) + I_{n-1} \Delta t$

Resistance  $R_n(X) = \frac{R_{n-1}(X)}{1 + B_n}$

The changes of current distribution and the corresponding thickness distribution calculated for  $R_0 = 1$  and  $R_0 = 10$  are shown in Fig. 5.23.



**Figure 5.23** Current and thickness distributions during metal deposition on the primary layer with resistances (a)  $R_0 = 1$  (b)  $R_0 = 10$

According to the calculations, as deposition proceeds, the current always distributes more densely in the position near the contact tip, and the thickness grows mainly in the  $z$ -direction in the area near the contact tip. The higher the resistance  $R_0$  of the primary layer, the more dense the distributions of current and thickness near the contact tip. This behaviour is paradox to the lateral propagation observed during metal deposition. If propagation occurs due to the current distribution, the current should be distributed more densely at the edge of the deposited metal layer and the layer develops in the lateral direction.

Thus, the current distribution cannot be used as explanation for the propagation of the secondary layer. The mechanisms of propagation of the secondary as well as that of primary layers will be discussed in section 5.4.

## 5.2.2. Influence of potential, coverage of cobalt sulphide and electrolyte concentration on the propagation rate

### 5.2.2.1. Current transient of the metal deposition

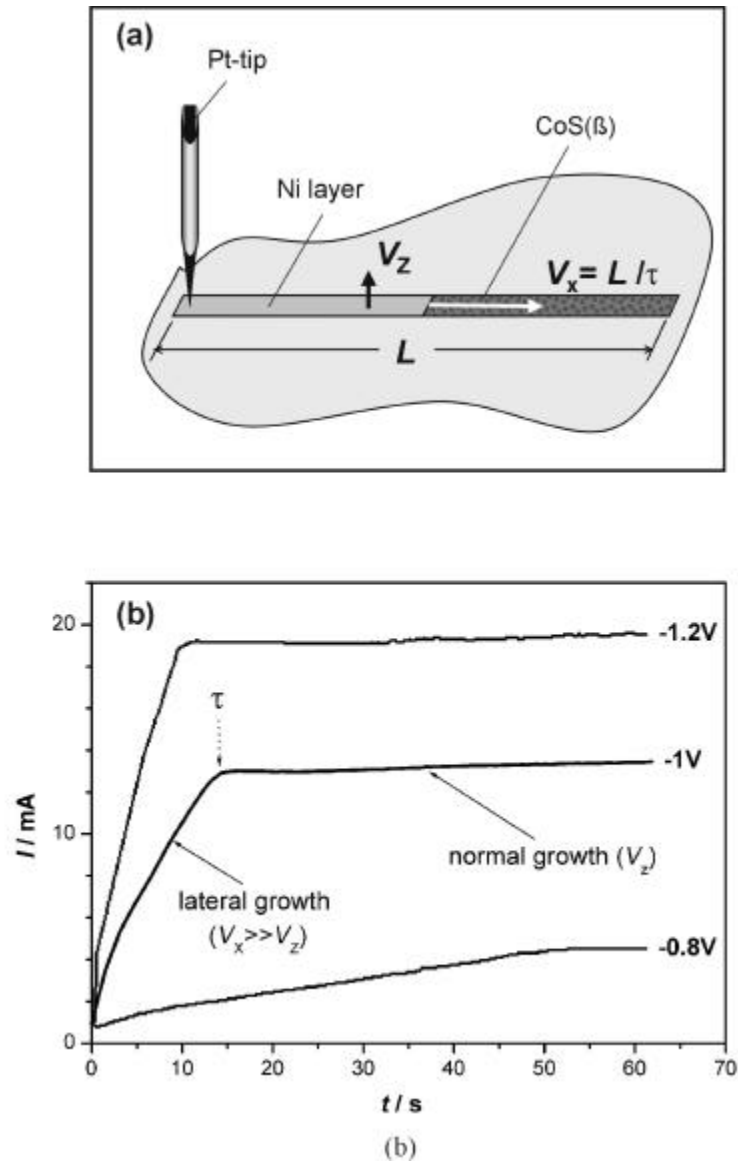
The propagation of the Ni layer is induced at local contact and propagates until the activated surface is completely covered. For microsystem technology, it is interesting to study the propagation of the metal in a defined activated microstructure. In this section, the kinetics of lateral propagation of the Ni layer was investigated by current transient measurements on activated line-shaped structures, which were formed following the pre-structuring concept using a mask. The metal deposition is performed by a Pt contact tip as illustrated in Fig. 5.24.

Typical current transients for metallization of activated line-shaped structures on ABS are shown in Fig. 5.24b. The transients are characterized by an initial nearly linear current increase followed by an establishment of a stationary current at a characteristic time  $t$ . Simultaneous microscopic observations showed that  $t$  corresponds exactly to the time at which the propagating secondary Ni layer reaches the opposite edge of the line-shaped structure (Fig. 5.24a). It should be mentioned that the currents recorded are mainly related to the secondary layer, probably because of its high conductivity compared with the primary and the current distributes mostly on the secondary layer. The lateral propagation rate  $V_x$  of the secondary Ni layer was calculated using the relation:

$$V_x \approx V_x'' \approx \frac{L}{t} \quad (5.17)$$

where  $L = 12 \text{ mm}$  is the length of the line-shaped structure.

It should be noted that the electrodeposition can initiate at applied potentials more cathodic than a critical potential  $-0.25 < E_{\text{crit}} < 0.3 \text{ V}$ . However, a propagation on the whole activated structure can only occur at  $E = -0.5 \text{ V}$ . The metal deposition at  $E_{\text{crit}} > E > -0.5 \text{ V}$  leads to a stoppage of propagation and an uneven thickness is obtained as shown in Fig. 5.24.



**Figure 5.24** Lateral propagation of the Ni layer during metallization of an activated line-shaped ABS surface structure (CoS( $\beta$ ) coverage  $\approx 49\%$ ).

- (a) Schematic representation of the experiment.  
 (b) Current transients at different applied potentials  $E$

### 5.2.2.2. Influence of potential, coverage of CoS( $\beta$ ) and electrolyte concentration

#### *Influence of potential and the coverage*

Experimental results show that both, the CoS( $\beta$ ) coverage  $\theta$  and the potential  $E$  of the contact Pt-tip determine propagation rate  $V_x$  of Ni layers. Fig. 5.25 shows  $V_x$  as a function of potential  $E$  and CoS( $\beta$ ) coverage  $\theta$ . Experimental results indicate that for a given  $\theta$ , the propagation rate  $V_x$  increases exponentially with  $E$  and can be described by:

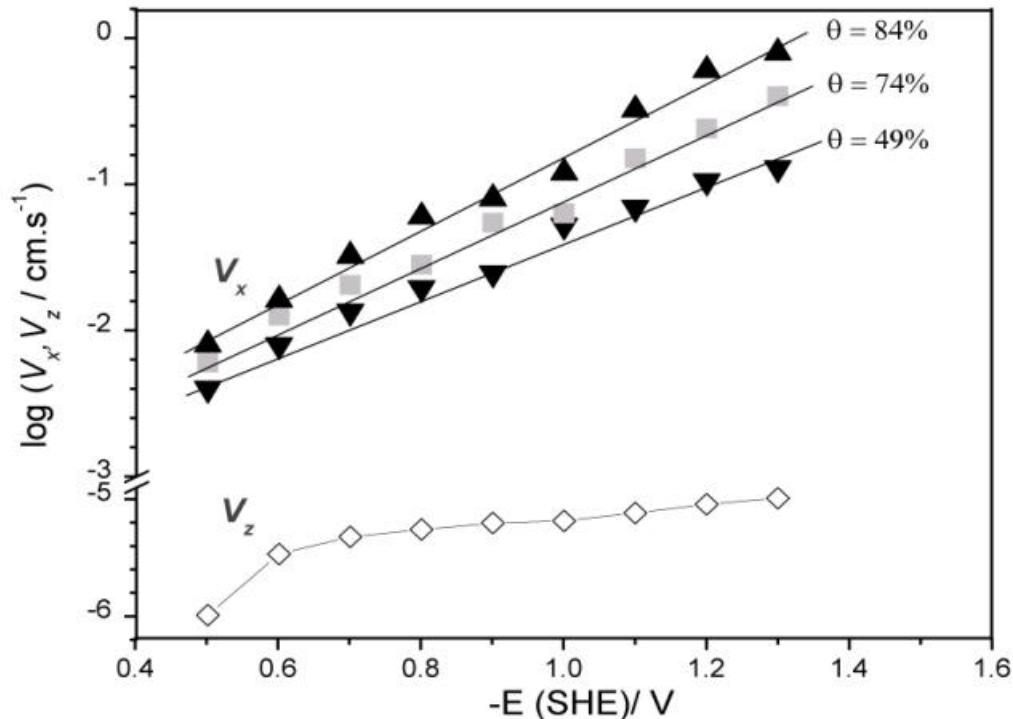
$$V_x(E) = V_x(E_{crit}) \exp\{k_7 |E - E_{crit}|\} \quad (5.18)$$

where  $V_x(E_{crit})$  represents the propagation rate at the critical potential and  $k_7$  is a constant depending on the CoS( $\beta$ ) coverage  $\theta$ . A value of  $k_7 = 0.18 \text{ V}^{-1}$  is obtained for single activation ( $\theta = 49\%$ ).

In order to compare the growth of the metal in the  $x$  and  $z$  directions, the normal growth rate of the Ni layer  $V_z$  is calculated using Faraday's relation:

$$V_z = \frac{d(d_{Ni})}{dt} = \frac{D}{F.A} \cdot \frac{dQ}{dt} = \frac{D}{F.A} \cdot \eta \cdot I \quad (5.19)$$

Where  $D$  is the density of Ni ( $D=6.59 \text{ cm}^3/\text{mol}$ ),  $A$  is the area of the line-shaped structure ( $A=0.096$ ),  $F$  is Faraday's constant ( $F = 96500 \text{ C/mol}$ ),  $\eta$  is the current efficiency [Bren63] and  $I$  is the current recorded by the transient measurement. Results show that the lateral propagation rate  $V_x$  is several orders of magnitude higher than the normal growth rate of the Ni layer  $V_z$  in the  $z$ -direction ( $V_x/V_z = 10^3$ – $10^4$ ). This behaviour offers possibilities for metallization of insulating surfaces with complex profiles and microstructures. The application of the PLATO technique for microstructured metallization will be demonstrated in chapter 6.

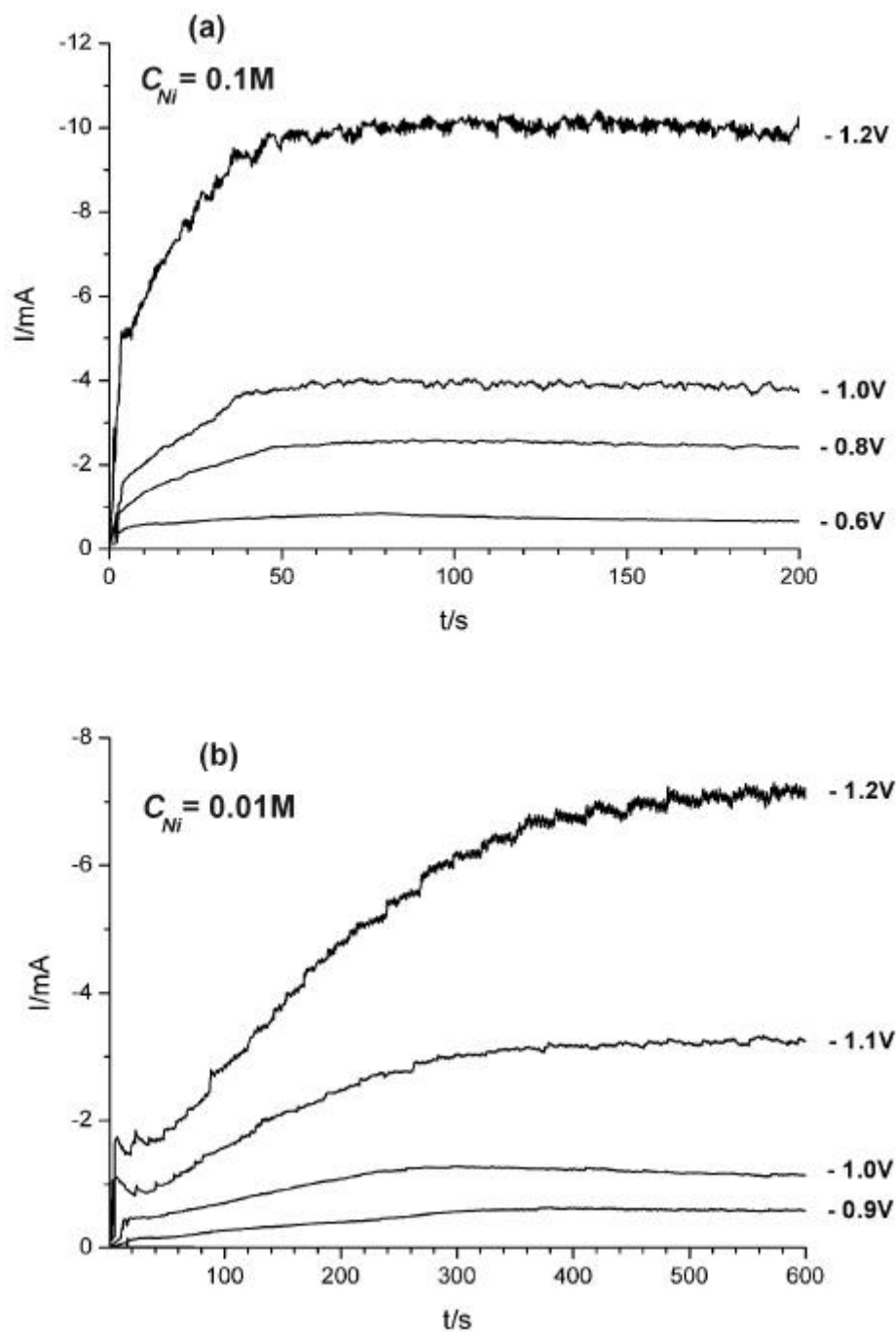


**Figure 5.25** Dependence of the propagation rate  $V_x$  and the normal growth  $V_z$  of a Ni layer on the applied potential  $E$  and the CoS( $\beta$ ) coverage  $\theta$  for metallization of ABS.

*Influence of the electrolyte concentration*

Fig 5.26 shows current transients during metal deposition on the line-shaped structures and in electrolytes containing 0.1M and 0.01M Ni<sup>2+</sup>, compared with the experiments carried out in 1M Ni (Fig. 5.19). Some behaviours of the propagation are remarked:

- The propagation can only take place at:
  - $E = -0.6\text{V}$  for  $C_{Ni} = 0.1\text{M}$
  - $E = -0.9\text{V}$  for  $C_{Ni} = 0.01\text{M}$
  - ( $E = -0.5\text{V}$  for  $C_{Ni} = 1\text{M}$ ).
- The propagation rate decreases with time, indicated by the parabolic increase of the current at the first period in transients (Fig. 26). This behaviour is attributed to the increase of the potential drop due to the low conductivity of the deposited Ni layer. With decreasing  $C_{Ni}$ , the non-linear increase is more pronounced.
- The concentration also influences the normal growth of Ni after the structures are covered by the Ni layers. Transients show a decrease of the currents in the “stationary” zone for  $C_{Ni} = 0.1\text{M}$  and  $C_{Ni} = 0.01\text{M}$ , while the currents are constant for the  $C_{Ni} = 1\text{M}$ .
- As mentioned above, the propagation rate is not constant during metal deposition on the structures in solution with  $C_{Ni} = 0.1\text{M}$  and  $C_{Ni} = 0.01\text{M}$  Ni. However, the average propagation rate can be calculated using relation (5.1). Results from the calculation show that the propagation rates decrease with decreasing concentration of Ni.



**Figure 5.26** Current transients of Ni deposition on line-shaped activated structures ( $\approx 49\%$ ) in electrolytes:

(a)  $C_{Ni} = 0.1M$

(b)  $C_{Ni} = 0.01M$

### 5.3. Mechanisms of metal deposition

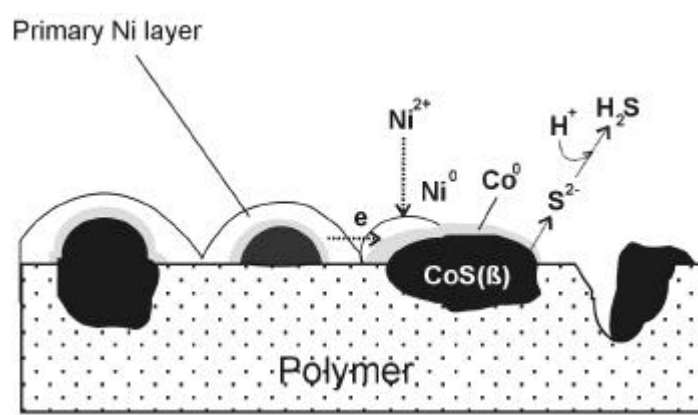
Ni deposition on insulating surfaces activated by CoS( $\beta$ ) takes place by the lateral propagations of the two layers: primary ( $\dot{\phantom{x}}$ ) and secondary ( $\ddot{\phantom{x}}$ ). As shown in section 5.2, the propagation rates of the primary layer ( $V_x\dot{\phantom{x}}$ ) and the secondary layer ( $V_x\ddot{\phantom{x}}$ ) are functions of deposition potential ( $E$ ), coverage of CoS( $\beta$ ) ( $\theta$ ) and Ni concentration in the electrolyte ( $C_{Ni}$ ).

#### 5.3.1. Formation of the primary layer

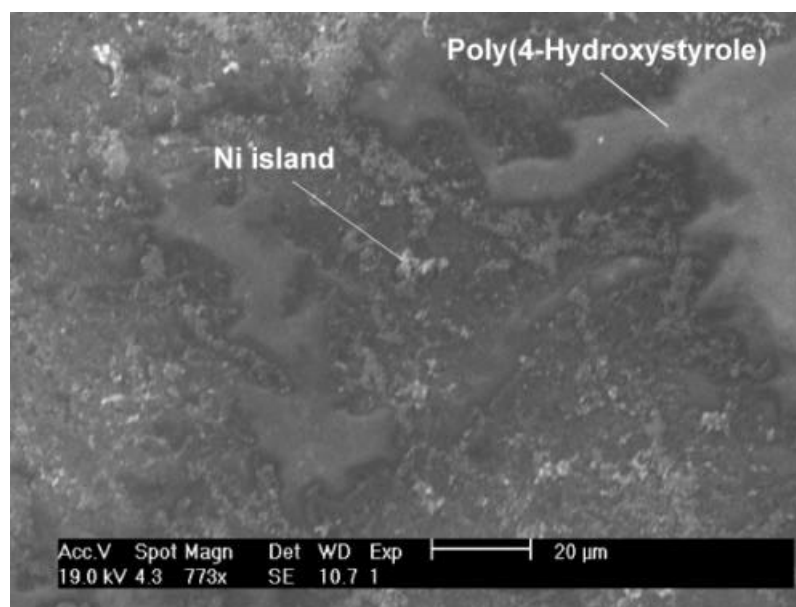
As shown in chapter 5.2, AFM and XPS studies show that the primary layer consists of Ni hemispheres. The appearance of those hemispheres indicates that Ni deposits preferentially at certain positions. In chapter 5.1, it was shown that the reduction of CoS( $\beta$ ) at potential  $E < -0.25V$  catalyzes the deposition reaction of Ni. Thus, it is reasonable to suggest that Ni deposits preferentially onto CoS( $\beta$ ) clusters to form the primary Ni layer. Thus, the deposition mechanism of Ni on the metal cluster can be proposed as following (Fig 5.27): reduction reactions occur partially on the CoS( $\beta$ ) surface, where  $H_2S$  can easily diffuse into the electrolyte. The structure of the obtained hemispheres consists of a core (15%  $Co^0$ , 10%  $H_2S$ , the unreduced CoS( $\beta$ )), covered by deposited Ni. As mentioned above, Ni hemispheres contact to each other in three dimensions to form the conductive primary layer, which maintains the supply of electrons from contact tip to the next unreacted CoS( $\beta$ ) cluster (Fig. 5.26). The Ni deposition reaction, which is catalyzed by the reductions of CoS( $\beta$ ), occurs very fast among the CoS( $\beta$ ) clusters, resulting a lateral propagation of the Ni layer at the first stage of the deposition process. The conductivity of the primary layer is decided by the density of hemispheres following the percolation rule e.g. the conductivity increases exponentially with density.

In order to demonstrate the nucleation on CoS( $\beta$ ) clusters, a Ni deposition on a glass/Poly(4-Hydroxystyrole)/CoS( $\beta$ ) is carried out (Poly(4-Hydroxystyrole) is the hydrophilic layer to enhance the adsorption of CoS( $\beta$ )). Fig. 5.28 shows the border zone between the deposited metal layer and the activated area. At sites near the metal layer, metal deposition takes place on CoS( $\beta$ ) clusters and Ni islands are obtained (Fig. 5.28), although the islands are only connected with each other, but they do not form a continuous Ni layer. This indicates that the Ni deposition is induced by reduction reactions on clusters. Underpotential deposition may also take place in this case.





**Figure 5.27** Processes during metal deposition



**Figure 5.28** Ni islands formed near the Ni layer on glass/Poly(4-Hydroxystyrole)/CoS(β). Metal deposition is carried out at  $E=-0.6V$ .

As mentioned above, Ni hemispheres contact to each other to form the primary layer. Therefore, the conductivity  $\sigma'$  of the primary layer is determined by 2 factors: (i) the contact between hemispheres, following the “percolation” theory (e.g. the conductivity is an exponential function of the conductive hemisphere) [Wu97] and (ii) the thickness of the deposited Ni on the clusters. Thus, influences of the deposition potential  $E$ , the coverage  $\theta$  of CoS(β) and the Ni concentration  $C_{Ni}$  on the conductivity  $\sigma'$  of the primary layer can be interpreted as follows:

- Potential  $E$ : An increase of  $E$  leads to a higher deposition rate  $i$  through Butler – Volmer equation (2.8). Thereby, thicker and higher conductivity deposited Ni films on each CoS( $\beta$ ) are obtained, leading to the higher conductivity  $\sigma'$  of the primary layer.
- Coverage  $\theta$ : the contact of hemispheres is easier when the number of CoS( $\beta$ ) clusters is higher, corresponding to the coverage  $\theta$  on the surface. The higher density of the hemispheres, the higher the conductivity of the primary layer, according to the percolation theory.
- Concentration  $C_{Ni}$ : at low  $C_{Ni}$ , the Ni deposition is controlled by the diffusion of  $Ni^{2+}$  from bulk to the Co surface, leading to the lower deposition rate  $i$  in equation (2.8) As a result, the deposited Ni layer on Co has lower thickness e.g. the formed hemispheres have lower conductivity.

### 5.3.2. Formation of the secondary layer

The secondary layer is formed on the primary layer following the metal deposition mechanism on a thin and low conductivity metal layer. Generally, nucleation and growth of metal at an arbitrary position on the primary layer is determined by three factors:

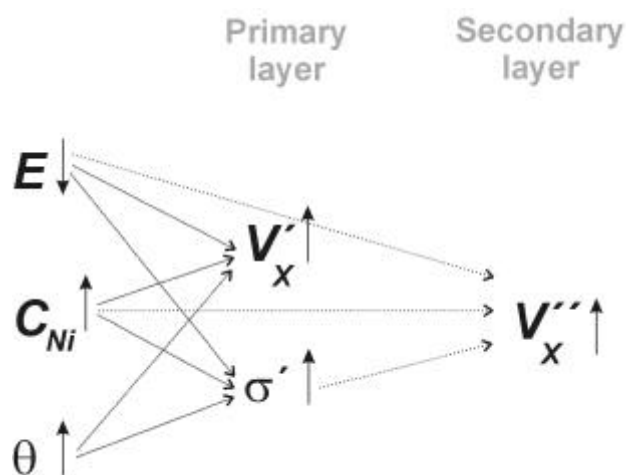
- (i) overpotential  $\eta$  at this position;
- (ii) the metallographic properties of the position (crystallographic defects, inhibited surface) and
- (iii) Ni concentration  $C_{Ni}$ .

If we suppose that the metallographic properties (factor (ii)) are neglected, the thickness growth can be calculated as shown in section 5.2 (simulation). This calculation shows that the thickness grows mainly in the area near the contact tip and in the normal direction  $z$  e.g. the lateral propagation does not occur. This paradox indicates that the metallographic properties play important roles in the propagation phenomenon. We suggest that the propagation observed is a result of two effects: nucleation takes place preferentially at the border secondary/primary/electrolyte and the growth in  $z$ -direction is slowed down by the hydrogen formation.

The influence of  $E$ ,  $\theta$  and  $C_{Ni}$  on the propagation rate  $V_x''$  can be explained as follows:

Nucleation and growth rates at the border secondary/primary/electrolyte increase with increasing  $\theta$ , which is given by  $\theta = E - E_{drop} - E_{Ni^{2+}/Ni}$ . It should be noted that the potential drop  $E_{drop}$  decreases with increasing conductivities  $\sigma'$  of the primary layer, which is in turn related to the coverage  $\theta$  and  $C_{Ni}$ . On the other hand,  $C_{Ni}$  influences directly the nucleation rate at the border, since low concentration of Ni leads to a lower adatom concentration, depletion of  $Ni^{2+}$  for charge transfer reaction at the border, thereby slows down the nucleation and growth processes. Both reasons result in a decreasing  $V_x''$  with decreasing  $C_{Ni}$ , as shown in 5.2.3.2.

The complex influences of  $E$ ,  $\theta$  and  $C_{Ni}$  on propagation rates of the primary,  $V_x'$ , and the secondary,  $V_x''$ , are summarized in Fig. 5.29.



**Figure 5.29** Schema describing influences of the applied potential  $E$ , coverage  $\theta$  and Ni concentration  $C_{Ni}$  on propagation rates of the primary layer,  $V_x'$ , and the secondary layer,  $V_x''$ .

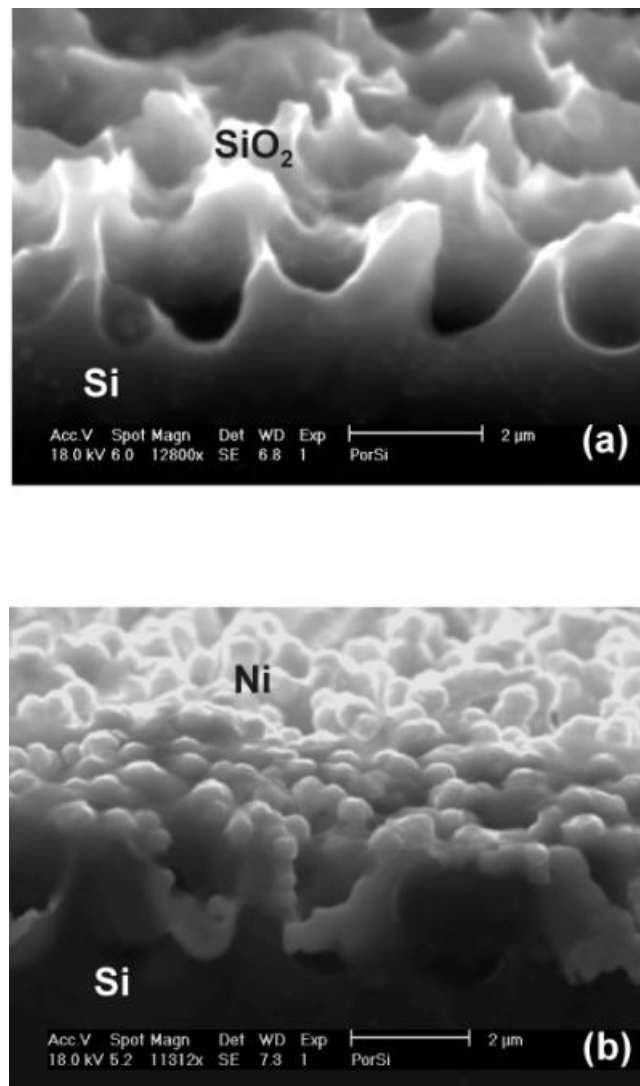
## 6. Applications

### 6.1. PLATO technique with different substrates and metals

#### 6.1.1. Metallization of porous silicon

Normally, the metallization of porous silicon (PoSi) is carried out by contact to the back side of the silicon wafer [Ronk96][Schö00]. The difficulty of the method is that potential drops on the silicon body and the oxide layer are relative high [Lehm02][Zhang01]. Therefore, the oxide layer on the back side must be removed and metal deposition onto PoSi is carried out at high potential (or current densities). Especially, if Si inside the pores is also oxidized, the metal deposition could become very difficult.

The PLATO technique, which uses tip contacting on the front side of PoSi, is a suitable method for metal deposition onto oxidized PoSi, since the oxidized PoSi owns a porous and hydrophilic surface. Fig. 6.1 shows typical SEM images for a successful direct Ni metallization of an oxidized porous nSi surface using this approach. These PoSi surfaces were prepared by electrochemical etching and subsequent oxidation [Lehm02][Schö00]. The activation with CoS( $\beta$ ) was performed applying the routine described in chapter 3.1. Similarly as on polymer substrates, the metallization occurs by a fast lateral propagation of the Ni layer, which covers perfectly the surface profile.

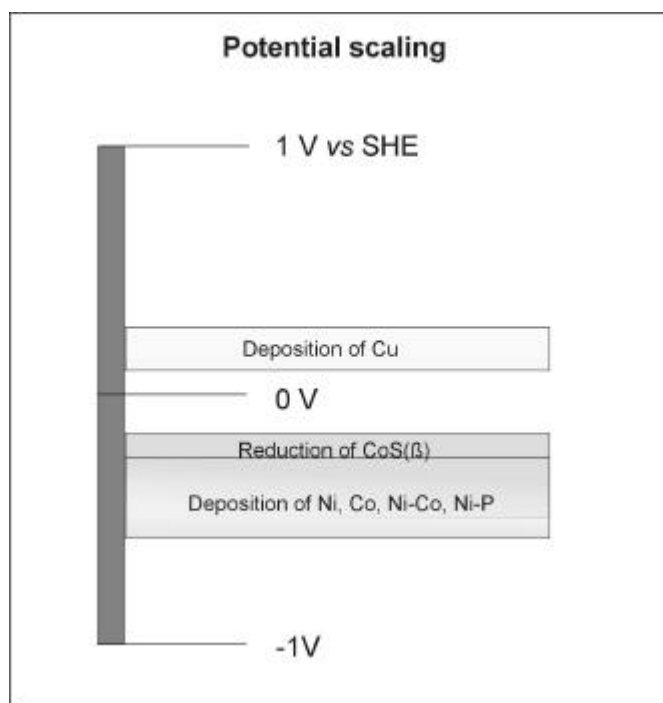


**Figure 6.1** SEM images of an oxidized porous n-Si surface (a) before and (b) after a direct galvanic Ni metallization at a potential of  $E = -0.7$  V.

### 6.1.2. Deposition of metals and alloys

The possibility for electrodeposition of metals and alloys by the PLATO technique is decided by two parameters:

- Plating zone  $E_{Me/Me^{z+}} > E > E_{powder}$  ( $E_{Me/Me^{z+}}$  is equilibrium potential,  $E_{powder}$  is potential corresponding to the formation of the metal powder). For metallization by the PLATO technique, the plating zones of metals or alloys should overlap the zone of CoS( $\beta$ ) reduction ( $E < -0.25V$ ). Fig. 6.2 represents the plating zones of different metals(alloys) and the reduction zone of CoS( $\beta$ ).
- pH of the deposition electrolyte. The pH of electrolyte influences on the hydrogen evolution and the stability of CoS( $\beta$ ).

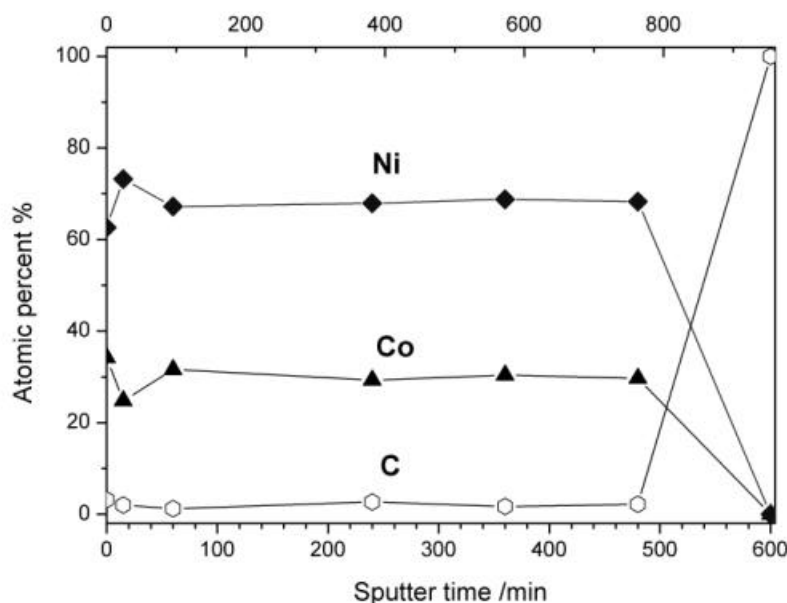


**Figure 6.2** Plating zones of Cu, Co, Ni and Ni-alloys and reduction zone of CoS( $\beta$ ).

#### *Deposition of Co-Ni alloy*

Both Ni and Co are suitable for metallization using activated CoS( $\beta$ ) because of two reasons: (a) their plating zones overlap the zone of CoS( $\beta$ ) reduction (cf. Fig. 6.2) and (b) pH of the deposition electrolyte is relative high (pH=4). Therefore, H<sub>2</sub> evolution is eliminated and CoS( $\beta$ ) is stable (cf. Pourbaix diagram of CoS( $\beta$ ) - Fig. 5.2). Because of those reasons, we attempt to deposit electrochemically a Co-Ni alloy on insulating substrates using the PLATO technique.

Electrodeposition of Ni-Co alloy was carried out successfully in a Watt's type bath with  $C_{Co}/C_{Ni}=1/10$  (cf. table 3.2),  $E = -0.7V$ ,  $t = 3$  min. The XPS sputter profile shows that the deposited alloy layer has a composition (64Ni36Co) and concentrations of Co and Ni are evenly distributed in the layer (Fig. 6.3).



**Figure 6.3** XPS sputter profile of a Ni-Co alloy electrodeposited on an ABS substrate ( $\eta=49\%$ ). Deposition conditions ( $C_{Co}=0.1M$ ,  $C_{Ni}=1M$ ,  $E=-0.7V$ ,  $t=3min$ ).

#### *Deposition of Ni-P alloy*

According to the plating zone criteria, Ni-P can be deposited easily on polymers activated by  $CoS(\beta)$ . In reality, after the deposition is induced, the propagation can stop after a certain time ranging from 2-4 minutes. The reason is that the low pH of the electrolyte ( $pH=1.8$ ) causes a dominant hydrogen evolution to occur predominantly on both the deposited Ni-P layer and the  $CoS(\beta)$  clusters. Therefore, the active sites for nucleation of the metal are inhibited, leading to the stoppage of propagation. The strong hydrogen evolution on Ni-P and metal sulphides is also reported in several studies [Pase93][Pase95][Pase97].

#### *Deposition of Cu*

Similar to the case of Ni-P, Cu deposition cannot be carried out in acidic Cu electrolyte because of the hydrogen evolution. On the other hand, Cu must be deposited at  $E < -0.25V$ , which results powder Cu, meaning that a Cu layer cannot be obtained. It is interesting to note that both problems, low pH and high potential of the plating zone, can be solved by the use of the Cu complex. However, the suitable conditions (ligands, pH...) should be further studied.

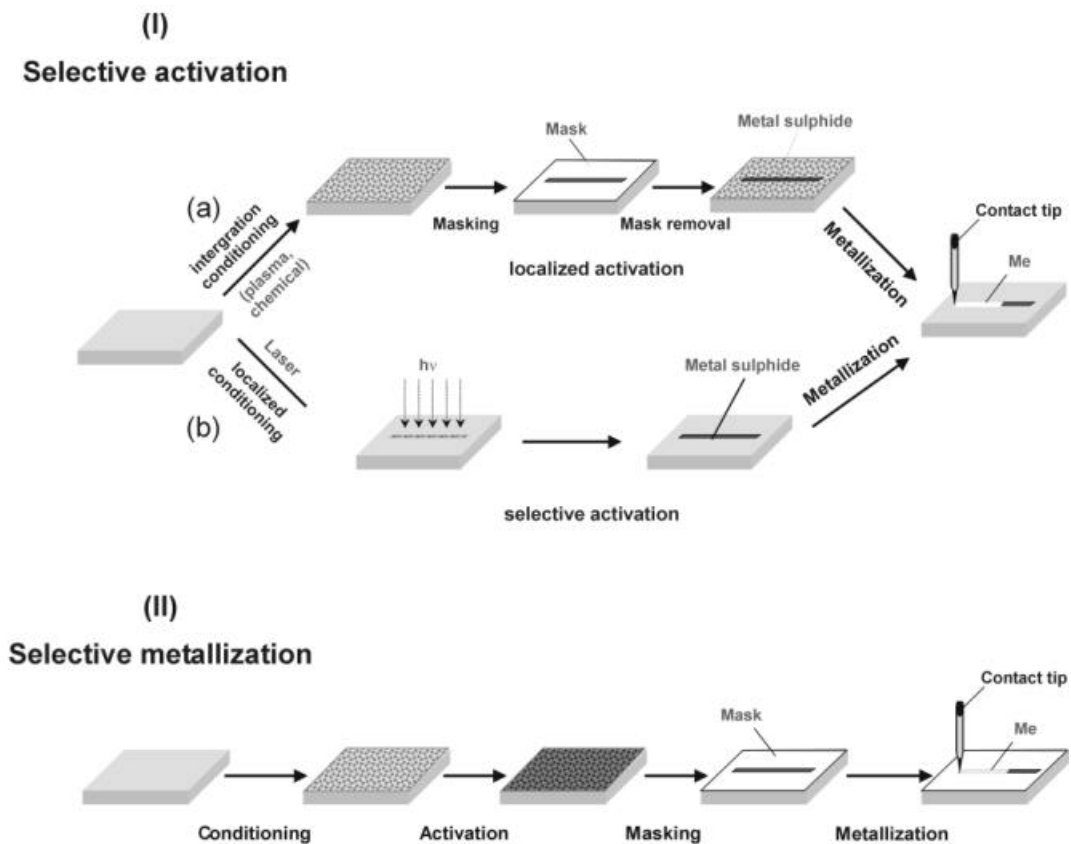
## 6.2. Microstructured metallization

### 6.2.1. Concepts and processes

Generally, microstructured metallization can be carried out following two concepts: post-structuring and pre-structuring. In the post-structuring routine, metal is deposited overall, followed by microetching of the metal layer. A typical example for this routine is the damascene process (IBM) [And94], in which the direct metallization method is considered as a substitutional method for electroless deposition and physical vapour deposition (PVD).

In this work, we propose two new routines for microstructured metallization considering the specific properties of the direct metallization using metal sulphide (Fig. 6.4):

- (I) microstructured activation and subsequent electrodeposition. Two possibilities for microstructured activation are:
  - (a) Homogeneous conditioning and selective activation using a mask;
  - (b) Local conditioning. The following activation localize only on the etched zone due to its properties (roughness, hydrophile);
- (II) homogeneous activation and selective metallization using a mask;



**Figure 6.4** Routines for microstructured metallization using the PLATO technique.



### 6.2.2. Microstructured activation (Routine I)

The microstructured activation and subsequent using mask (Ia) was shown in chapter 5.2, in order to study the propagation in microstructures. This routine provides a high selective metallization method e.g. metal is deposited only on the activated line-shaped structure, but the propagation does not take place on the unactivated zone.

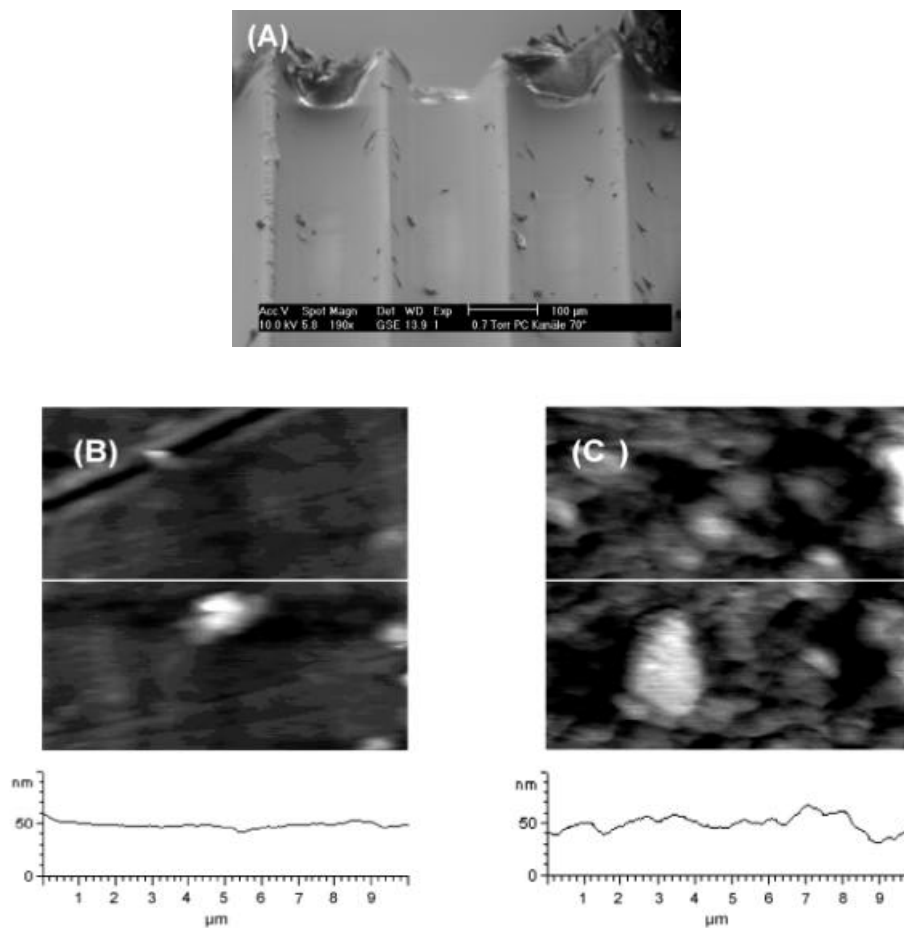
The routine (Ib) was tested with two processes:

- Local modification by excimer laser: The aim is to produce a rough and hydrophilic surface in microstructure, while the unmodified surface is kept flat and hydrophobic. It is expected that only the microstructure is covered by CoS( $\beta$ ) when the whole sample is activated. Fig. 6.5 shows a PC sample, on which channels (width 100 $\mu$ m, height 50 $\mu$ m) are produced by excimer laser (Kr source,  $\lambda=351$ nm,  $E_{puls}=500-1000$ mJ,  $f=1$ Hz)(delivered by Bartels GmbH). The roughnesses of the unmodified and the modified surface in channels obtained from AFM measurement are  $R_{rms}^{ori}=7$ nm,  $R_{rms}^{mod}=21$ nm.

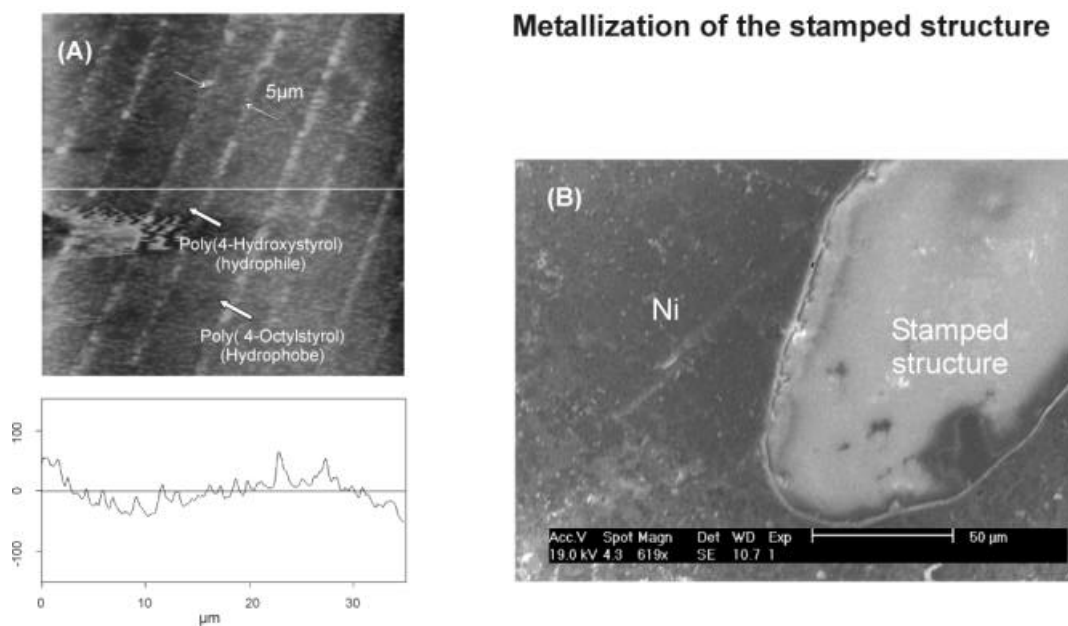
Results show that both, the unmodified and laser structured, surfaces cannot be metallized although four cycles of activation were applied. The reason is from the insufficient roughness of the modified structure. In order to achieve a modified surface suitable for the PLATO technique (higher roughness), the laser conditions should be optimized.

- Microstructuring by stamping technique [Breh02]: The sample shown in Fig. 6.6 consists of alternative hydrophilic and hydrophobic lines. The hydrophobic sublayer is Poly(4-Octylstyrol) (contact angle of water measuring on the material is  $\theta_{oct}=110^\circ$ ) and the hydrophilic block stamped on the layer is Poly(4-Hydroxystyrol) (contact angle  $\theta_{hyd}=90^\circ$ ). The principle is that CoS( $\beta$ ) will be selectively formed on hydrophilic blocks and only those blocks will be metallized when metal deposition is carried out.

However, results show that CoS( $\beta$ ) clusters are formed unselectively on both hydrophobe and hydrophile blocks. The subsequent metal deposition leads to the metallization of the whole surface (Fig. 6.6 b). The reason is from the insignificant difference of contact angle between hydrophilic and hydrophilic blocks.



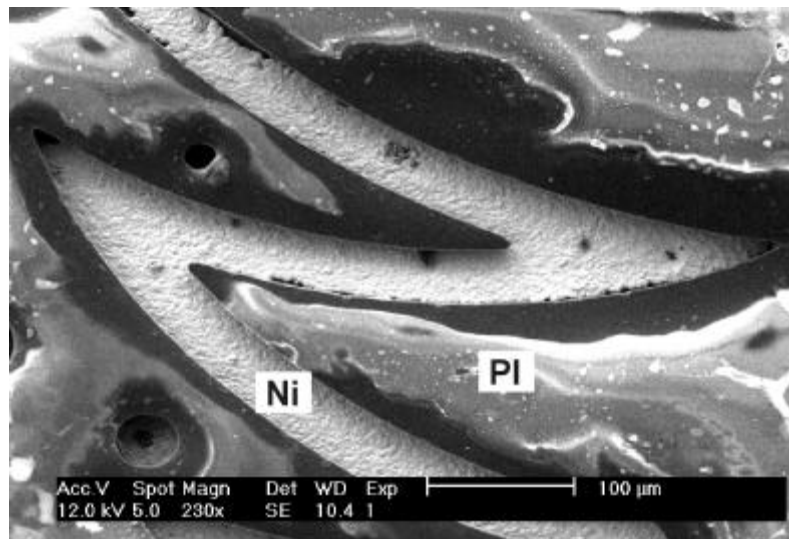
**Figure 6.5** (a) Microchannel on PC polymer produced by excimer laser; (b) surfaces topography of unmodified PC and (c) laser structured channel.



**Figure 6.6** (a) The original stamped structure  
(b) The structure after metallization

### 6.2.3. Metallization using masks (Routine II)

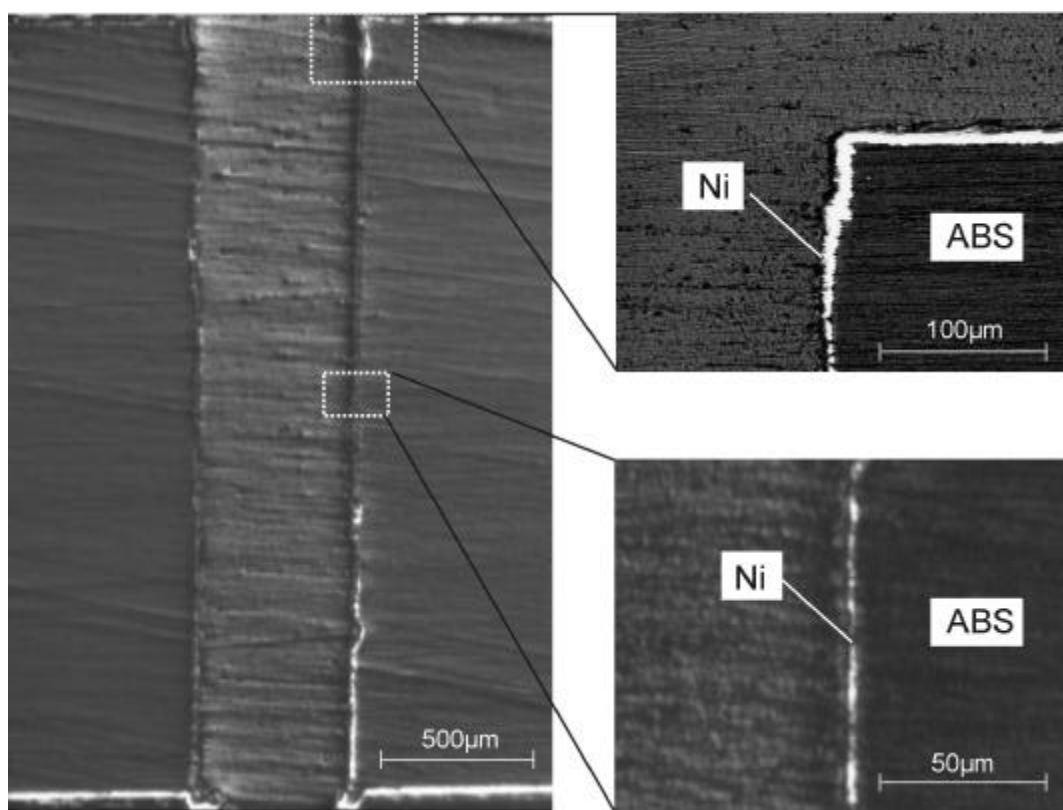
Fig. 6.7 demonstrates the example of direct microstructured metallization using mask (routine II – Fig. 6.4). The mask, which has the shape of a Christmas tree, was fixed on the activated ABS surface (coverage of  $\text{CoS}(\beta)$   $\approx 84\%$ ). The metallization was carried out using a local contact at the top of the tree. This experiment shows that the propagation during metal deposition can also take place in small and complex geometries with a width of  $40\ \mu\text{m}$  and a length of several mm. Bended shapes with angles  $<30^\circ$  are well reproduced. However, similar to electrodeposition through masks on metal substrates, concentration and current distributions should be taken into account.



**Figure 6.7** Metallized microstructure of an homogeneously activated ABS substrate (coverage of cobalt sulphide  $\approx 84\%$ ). For metallization, an excimer laser structured polyimide (PI) mask was applied ( $E = -0.8\text{V}$ ,  $t = 3\text{min}$ ).

#### 6.2.4. Through-hole metallization

Due to the fast propagation rate and the flexibility of the activation process, the direct metallization is a good method for metallization of insulating microstructures with complex geometries. Fig. 6.8 demonstrates a through-hole metallization of an insulating structure with aspect ratio  $A = 5$ . The activation was applied on the surface of the sample and on the hole-walls. The through-hole metallization was carried out successfully by placing a contact tip on the surface of the sample. The uneven distribution of the thickness (Fig. 6.8) due to the diffusion of the electrolyte in the hole can be further optimized by applying suitable technological parameters (additive, convection etc.).



**Figure 6.8** Cross-section of the through-hole metallized structure on the ABS substrate applying the PLATO technique ( $E = -0.8V$ ,  $t = 5\text{min}$ ).

## 7. Conclusions

### 1. Pre-treatment (Fig. 7.1)

?? Etching: surfaces of polymers after chemical etching are characterized by the enhancement of roughness (roughness factor  $r$ ), the formation of  $-\text{COOH}$  and/or  $-\text{COH}$  groups, and the consequent hydrophilicity (contact angle  $\theta$ ). Among those factors, the enhancement of roughness is decisive for the degree of activation e.g. the coverage of  $\text{CoS}(\beta)$  after activation. However, the surface modification and the corresponding coverage of  $\text{CoS}(\beta)$  are not the same on different polymers due to their different chemical nature.

?? Activation: The degree of activation determines the metallization ability of a surface. Only surfaces with coverage of  $\text{CoS}(\beta)$   $\theta > 30\%$  can be metallized using the PLATO technique. On the activated surface,  $\text{CoS}(\beta)$  is not a continuous layer, but discrete clusters, which are located preferentially in the pores.

### 2. Metal deposition (Fig. 7.1)

?? The formation of the primary layer occurs by deposition of Ni onto the  $\text{CoS}(\beta)$  clusters. It is suggested that the reduction of  $\text{CoS}(\beta)$  to  $\text{Co}^0$  at  $E < -0.25\text{V}$  catalyzes the Ni deposition process. The primary layer is a set of conducting hemispheres consisting of a core ( $\text{Co}^0$ ,  $\text{CoS}(\beta)$ ) covered by deposited Ni (Fig. 7.1) with a conductivity governed by the percolation law. The factors influencing the formation of the primary layer (e.g. propagation rate ( $V_x'$ ), thickness ( $d'$ ) and conductivity ( $\sigma'$ )) are:

Deposition potential  $E$

Coverage of  $\text{CoS}(\beta)$   $\theta$

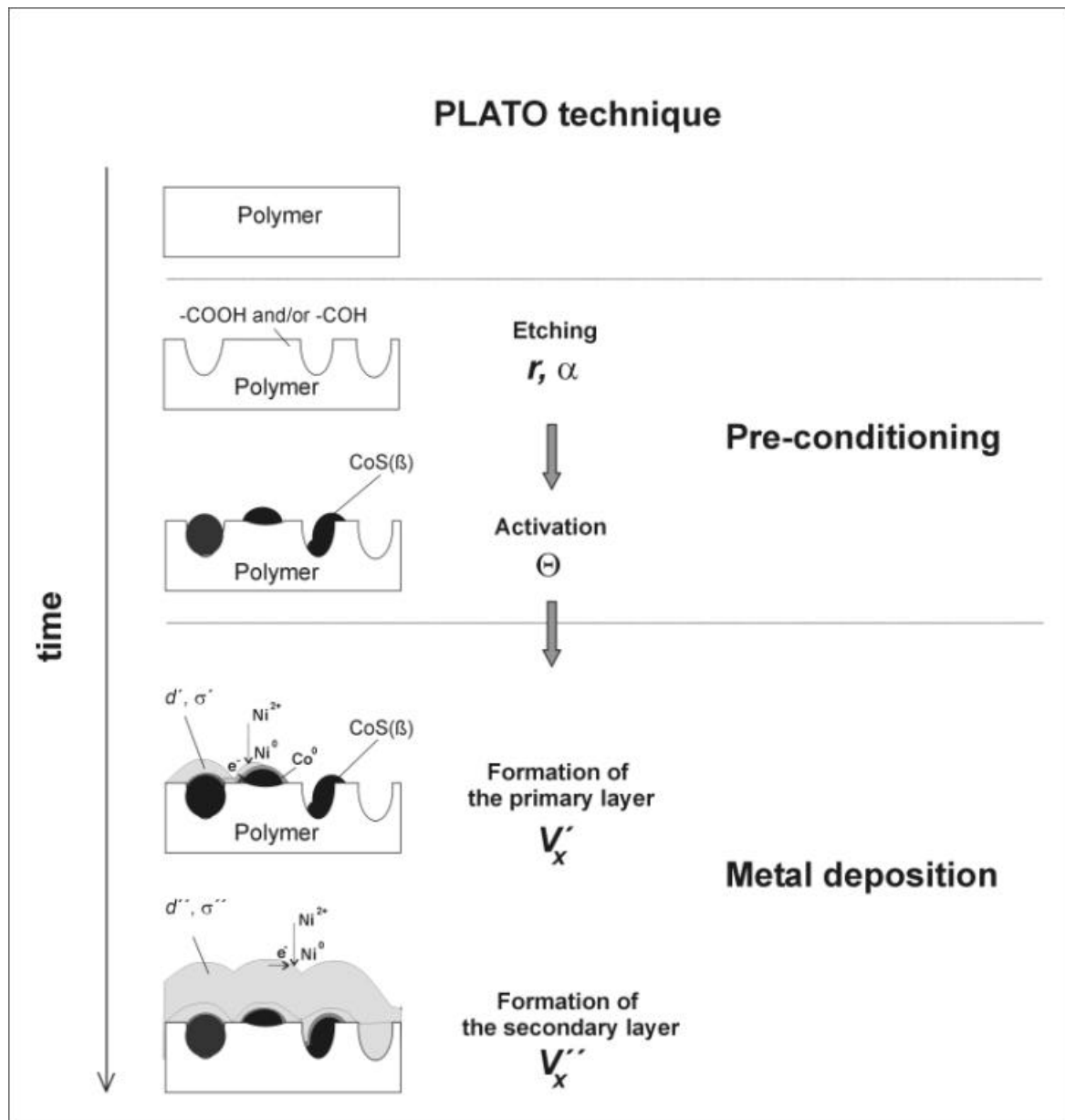
Ni concentration of electrolyte  $C_{\text{Ni}}$

?? The formation of the primary layer follows the mechanisms of metal deposition onto a low conductivity metal layer. At the first stage of the formation, the secondary layer propagates laterally with a rate  $V_x''$ . The propagation rate  $V_x''$  is determined by:

Deposition potential  $E$

Conductivity of the primary layer  $\sigma'$

Ni concentration of electrolyte  $C_{\text{Ni}}$



**Figure 7.1** Mechanisms of pre-treatment and metal deposition in the PLATO technique and characteristic parameters for each step.

### 3. Application

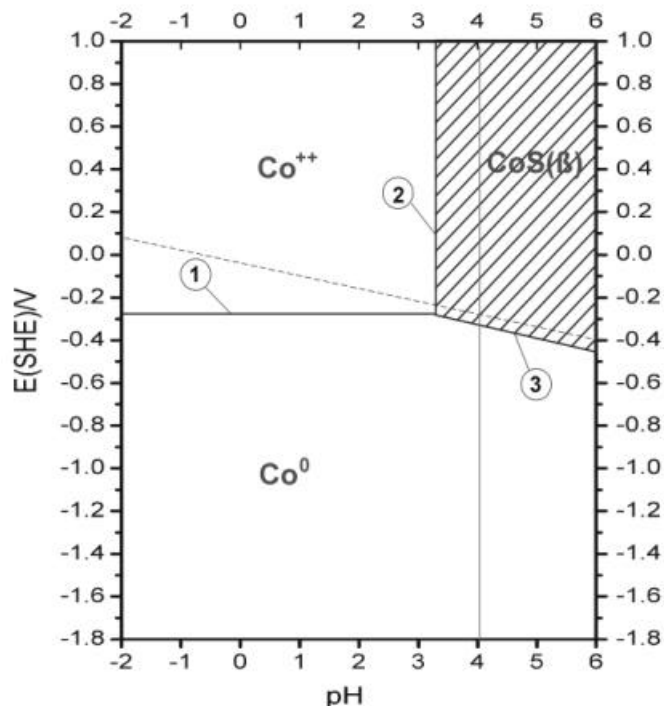
- ?? PLATO technique can be applied for metalization of oxidized porous silicon (PoSi). The most suitable deposited metals and alloys for the technique are Ni, Co and Co-Ni alloys. Other metals and alloys can be only deposited if the two conditions are optimized: (i) plating zones of the metals (alloys) overlap the reduction zone of the sulphide and (ii) pH of the electrolyte is not low (pH>3).
- ?? Microstructured metallization can be applied by (i) microstructured activation and (ii) metallization using masks.

#### **4. Further studies**

- ?? Influence of the roughness on the activation and the adhesion of the deposited metal layer. In order to regulate the roughness, the etching condition should be precisely controlled, probably by the uses of plasma or excimer laser.
- ?? Characterization of the electrochemical reduction of other metal sulphides (CuS, ZnS)
- ?? Influence of electrolytes (complex, pH) for deposition of other metals and alloys

## 8. Appendices

Establishment of Pourbaix diagram for  $\text{CoS}(\beta)$



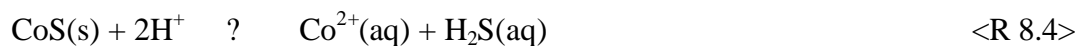
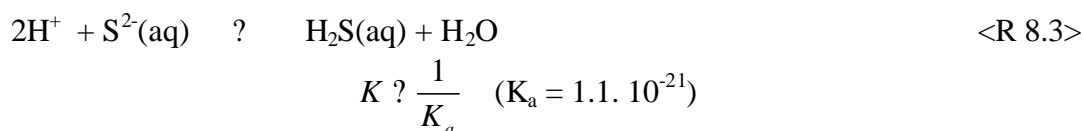
**Figure 8.1.** Establishment of Pourbaix diagram for  $\text{CoS}(\beta)$ .



Equation       $E_{\text{Co}/\text{Co}^{2+}} \approx 0.23\text{V}$

Line (2)      *Stability of  $\text{CoS}(\beta)$*

Dissolution reactions of  $\text{CoS}(\beta)$



$$K \approx \frac{[\text{Co}^{2+}][\text{H}_2\text{S}]}{[\text{H}^+]^2} \approx \frac{K_{sp}}{K_a} \approx \frac{10^{25}}{1.1 \cdot 10^{-21}} \approx 9 \cdot 10^{45}$$

The critical  $\text{H}^+$  concentration, at which  $\text{CoS}(\beta)$  is stable, is :

$$[\text{H}^+] \approx \frac{[\text{Co}^{2+}][\text{H}_2\text{S}]}{K} \approx \frac{\sqrt{K_{sp}}}{K} \approx 5.9 \cdot 10^{24} \quad \text{or} \quad \text{pH} = 3.2$$



Line (3)      *Reaction*       $\text{CoS(s)} + 2\text{e}^- + 2\text{H}^+ \rightleftharpoons \text{Co}^0(\text{aq}) + \text{H}_2\text{S}(\text{aq})$       <R 8.5>

$$E_{\text{Co}/\text{Co}^{2+}} \approx E_{\text{Co}/\text{Co}^{2+}}^{\circ} \approx \frac{0.059}{2} \ln \frac{a_{\text{Co}^{2+}}}{a_{\text{Co}}}$$

$$a_{\text{Co}^{2+}} \approx \frac{K_{sp}}{a_{\text{S}^{2-}}} \approx \frac{K_{sp}}{K_a} [\text{H}^+]^2$$

$$E_{\text{Co}/\text{Co}^{2+}} \approx 0.23 - \log(9.10^{-5}) * 0.059/2 - 0.059 * \text{pH} = 0.11 - 0.059 * \text{pH}$$

Equation       $E_{\text{Co}/\text{Co}^{2+}} \approx 0.11 - 0.059 * \text{pH}$

*List of symbols*

$a$	actual area of surface, $\mu\text{m}^2$
$a_{Me}$	activity of metal
$a_{Me^{z+}}$	activity of ion in the electrolyte
$A$	apparent area (geometrical area), $\mu\text{m}^2$
$A_i$	Area of XP peak of specie $i$
$d$	thickness of the deposited layer, $\mu\text{m}$
$d'$	thickness of the primary layer
$d''$	thickness of the secondary layer
$C_{Ni}$	Ni concentration, mol/l
$D_{Ni}$	density of Ni, $6.59 \text{ cm}^3/\text{mol}$
$E$	Deposited potential, V
$E_{drop}$	Potential drop on metal layer, V
$E_{crit}$	Critical potential for the induced metal deposition, V
$E_{Me/Me^{z+}}$	Nernst equilibrium potential, V
$E_{powder}$	Potential for the formation of metal powder
$E_{kin}$	kinetic energy of photoelectron, eV
$E_b$	binding energy of photoelectron, eV
$F$	Faraday's constant, $96500 \text{ C/mol}$
$i$	current density, $\text{mA/cm}^2$
$i_{ct}$	charge transfer current density, $\text{mA/cm}^2$
$I$	current, mA
$J$	Nucleation rate
$L$	length of primary layer, m
$p$	pressure, $\text{N/m}^2$
$q$	charge density, $\text{mC/cm}^2$
$r$	roughness factor
$r^{(o)}$	roughness factor of original surface
$r^{(e)}$	roughness factor of etched surface
$R_{rms}$	root mean square roughness, nm
$R$	ideal gas constant, $8.314 \text{ J/mol.K}$
$S_i$	sensitivity for XPS quantitative analysis
$R_D$	transfer resistance, ?

---

$R_S$	substrate resistance, ? ?
$R_{el}$	electrolyte resistance, ?
$R_{pol}$	Polarization resistance, ?
$t$	time, s
$T$	absolute temperature, K
$V_m$	molar volume of, mol/m <sup>3</sup>
$V_x$	propagation rate of the metal layer, cm/s
$V_x'$	propagation rate of the primary layer, cm/s
$V_x''$	propagation rate of the secondary layer, cm/s
$V_z$	normal growth rate, μm/s
$X_a$	Concentration of element a
?	contact angle
?'	apparent contact angle
?' <sup>(o)</sup>	contact angle of original polymer surface
?' <sup>(e)</sup>	contact angle of etched polymer surface
? <sub>a</sub>	anodic charge transfer coefficient
? <sub>c</sub>	cathodic charge transfer coefficient
?	surface tension, N/m
? <sub>lv</sub>	surface tension at liquid-vapour boundary, N/m
? <sub>sv</sub>	surface tension at solid-vapour boundary, N/m
? <sub>sl</sub>	surface tension at solid-liquid boundary, N/m
?	work function, eV
?' <sup>(o)</sup>	surface energy of original polymer surface, J/m <sup>2</sup>
?' <sup>(e)</sup>	surface energy of etched polymer surface, J/m <sup>2</sup>
? <sub>w</sub>	surface energy using water as liquid, J/m <sup>2</sup>
??	increase of surface energy, mJ/m <sup>2</sup>
?	overpotential, V
? <sub>cry</sub>	crystallization overpotential, V
? <sub>d</sub>	diffusion overpotential, V
? <sub>ct</sub>	charge transfer overpotential, V
?'	conductivity of the primary layer, S.cm
?''	conductivity of the secondary layer, S.cm
?	coverage of CoS(β)

List of equations

$$r_{crit} = \frac{2d \cdot \cos \alpha}{p} \quad (2.1)$$

$$\gamma_{lv} \cos \alpha = \gamma_{sv} - \gamma_{sl} \quad (2.2)$$

$$\cos \alpha = r \cos \alpha' \quad (2.3)$$

$$\gamma_{sl} = \frac{\gamma_w}{4} (1 + \cos \alpha_a)^2 \quad (2.4)$$

$$E_{Me/Me^{z+}} = E_{Me/Me^{z+}}^0 - \frac{RT}{zF} \ln \frac{a_{Me^{z+}}}{a_{Me}} \quad (2.5)$$

$$\tilde{\mu} = zF(E - E_{Me/Me^{z+}}) - zF\eta \quad (2.6)$$

$$\gamma_{crys} = \gamma_{ct} + \gamma_d + \gamma_{chem} \quad (2.7)$$

$$\gamma_{crys} = E - E_{Me/Me^{z+}} - \frac{RT}{zF} \ln \frac{a_{Me_{ads}}}{a_{0,Me_{ads}}} \quad (2.8)$$

$$N_{crit} = \frac{8BN_A V_m^2 S^3}{27(\tilde{\mu})^3} \quad (2.9)$$

$$\frac{d \ln J}{d \tilde{\mu}} = \frac{N_{crit}}{RT} \quad (2.10)$$

$$i = i_{ct} = i_o \exp \left( \frac{a_a F}{RT} \eta \right) - \frac{c_s}{c_b} \exp \left( \frac{a_c F}{RT} \eta \right) \quad (2.11)$$

$$s(x, t) = a s_a + b(x, t) s_b \quad (2.12)$$

$$a s(x, t) \frac{d^2 \eta}{dx^2} = i_o \exp \left( \frac{a_a F}{RT} \eta(x, t) \right) - \frac{c_s(x, t)}{c_b} \exp \left( \frac{a_c F}{RT} \eta(x, t) \right) \quad (2.13)$$

$$\eta = \begin{cases} \eta_0 \exp \left( \frac{a_a F}{RT} (x - L) \right) \cdot \frac{const}{a s_a} & \text{If } x < L \\ \eta_0 & \text{If } x > L \end{cases} \quad (2.14)$$

$$E_{kin} = h E_b + e \quad (3.1)$$

$$X_a = \frac{A_a / S_a}{A_i / S_i} \quad (3.2)$$

$$R_{rms} = \sqrt{\frac{1}{l} \int_0^l y^2 dx} \quad (4.1)$$

$$r = \frac{A}{A_0} \dots\dots\dots (4.2)$$

$$\dots\dots\dots (4.3)$$

$$\dots\dots\dots (4.4)$$

$$\cos \theta_r^{(e)} = \frac{r^{(e)}}{r^{(o)}} \cos \theta_r^{(o)} \dots\dots\dots (4.5)$$

$$\dots\dots\dots (4.6)$$

$$X = x/L \dots\dots\dots (5.1)$$

$$Z = z/L \dots\dots\dots (5.2)$$

$$V_m = \frac{f_m}{RT/nF} \dots\dots\dots (5.3)$$

$$H = \frac{\dots}{RT/nF} \dots\dots\dots (5.4)$$

$$I = \frac{i_m}{i_s} \dots\dots\dots (5.5)$$

$$B = \frac{b(x,t)s_b}{as_a} \dots\dots\dots (5.6)$$

$$\dots\dots\dots (5.7)$$

$$R_0 = \frac{1/as_a}{1/kL} = \frac{kL}{as_a} \dots\dots\dots (5.8)$$

$$R(x,t) = \frac{1/(as_a + b_{avg}(x,t)s_b)}{1/kL} = \frac{kL}{as_a + b_{avg}(x,t)s_b} \dots\dots\dots (5.9)$$

$$R(x,t) = \frac{R_0}{1 + \dots} \dots\dots\dots (5.10)$$

$$B(X,?) = \int_0^? Idt \dots\dots\dots (5.11)$$

$$I \approx \frac{2}{R} g(\eta) \quad (5.12)$$

$$I \approx \frac{2}{R} g(\eta) \quad (5.13)$$

$$I \approx (1 - e^{-\eta}) \frac{2}{R} g(\eta) \quad (5.14)$$

$$(1 - e^{-\eta}) \frac{2}{R} g(\eta) \quad (5.15)$$

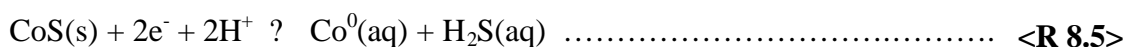
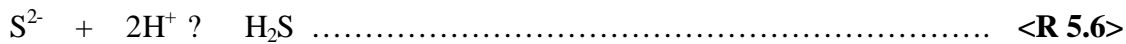
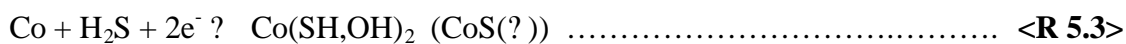
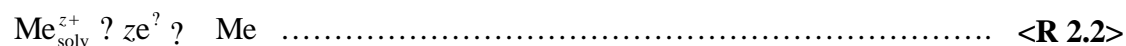
$$e^{-\eta} \frac{2}{R} g(\eta) \quad (5.16)$$

$$V_x \approx V_x^{\infty} \frac{L}{t} \quad (5.17)$$

$$V_x(E) \approx V_x(E_{\text{crit}}) \exp\left\{k \left| \frac{E - E_{\text{crit}}}{E_{\text{crit}}} \right| \right\} \quad (5.18)$$

$$V_z \approx \frac{d(d_{\text{Ni}})}{dt} \approx \frac{D}{F.A} \frac{dQ}{dt} \approx \frac{D}{F.A} \cdot I \quad (5.19)$$

### Reactions



## References

- [Ade97] H.Ade, A.P. Smith, H. Zhuang, J. Kirz, E. Rightor, A. Hitchcock, *J. Elec. Spec. Rel. Phen.* **84**(1997)53.
- [Alki73] R. Alkire, *J. Electrochem. Soc.* **118**(1973)1935.
- [And98] C. Andricacos, C. Uzoh, J. O. Dukovic, J. Horkans, and H. Deligianni, *IBM J. Res. Devl.* **42**(1998)567.
- [Bard80] A. J. Bard, *Encyclopedia of Electrochemistry of the Elements*, Marcel Dekker Incorporated, New York, 1980.
- [Beam92] G.Beamson and D.Briggs, *High resolution XPS of organic Polymers*, John Willy &Son, 1992.
- [Bert97] P.Bertrand, P.Lambert, Y. Travaly, *Nucl. Instr. And Meth. in Phys. Res. B* **131**(1997)71.
- [Bla90] US 4,919,768 (BLADON *et.al*), 24 April 1990.
- [Boon93] L. Boone, in: *15. Ulmer Gespräch-Kunststoffmetallisierung und leitende Polymere*, Eugen G. Leuze Verlag, 1993, p100.
- [Breh02] M. Brehmer, L. Conrad, L. Funk, A. Helfer, D. Allard, in: *Soft Litography on Block Copolymer Films*, in: *ACS Book*, New York, 2002.
- [Bren63] A. Brenner, *Electrodeposition of Alloys: Principle and Practice*, Academic Press, 1963.
- [Broc95] A. Brocherieux, O. Dessaux, P. Goumand, L. Gengembre, J. Grimblot, M. Brunel, R. Razzaroni, *App. Sur. Sci.* **90**(1995)47.
- [Bud96] E. Budevski, G. Staikov, W.J. Lorenz, in: *Electrochemical Phase Formation and Growth*, VCH, Weinheim 1996.
- [Burr93] US 5,238,550 (BURRES) 24 August 1993.
- [Chan92] C. Chan, *Polymer Surface Modification and Characterization*, Hanser Publishers,1992.
- [Char97] M. Charbonier, M. Alami, M. Romand, J.P Giardeau-Montaut, M. Afif, *App. Sur. Sci.* **109/110**(1997)206.
- [Comy96] J. Comyn, L. Mascia, G. Xiao, B.M. Parker, *Int. J. Adhesion and adhesives* **16**(1996)97.
- [Davi98] M.B. Davies, Cobalt 1995, *Co. Chem. Rev.* **169**(1998)237.
- [deLe94] D.W. de Leeuw, P.A. Kraakman, P.F.G. Bongaerts, C.M.J. Mutsaers, D.B.M. Kaasen, *Synt. Met.* **66**(1994)263.
- [DiBa00] G.A.DiBari, *Met. Finish.* **98**(2000)278.
- [Duca98] M. Duca, C. Plosceanu, T. Pop, *Pol. Degrad. and Stab.* **61**(1998)65.
- [Ekte00] A.M. Ektessabi, S. Hakamata, *Thin Solid Films* **377-378**(2000)621.
- [Fuhr00] A. Fuhrmann, *internal delivery*.
- [Fulg99] J.Fulghum, *J. Elec. Spec. Rel. Phenom* **100**(1999)331.
- [Galt99] A. Galtayries, J. Grimblot, *J. Elec. Spec. Rel. Phen.* **98-99**(1999)267.

- [Gome98] E. Gomez, J. Ramirez, E. Valles, *J. Appl. Electrochem.* **28**(1998)71.
- [Gome99] E. Gomez, E. Valles, *J. Appl. Electrochem.* **29**(1999)805.
- [Gott92] S. Gottesfeld, F.A. Uribe, S. Armes, *J. Electrochem. Soc.* **139**(1992)L14.
- [Gull89] US 4,810,333 (GULLA *et.al*), 07 March 1989 .
- [Ha97] S.W. Ha, R. Hauert, K.H. Ernst, E. Wintermantel, *Surf. Coat. Tech.* **96**(1997)293.
- [Harr92] J. A. Harrison and H. R. Thirsk, *Electroanal. Chem.* **5**(1992)67.
- [Hein99] R. Heinz, E. Klusmann, H. Meyer, R. Schulz, *Surf. Coat. Tech.* **116-119**(1999)886.
- [Henn98] C. Henneuse, B. Goret, Jmarchand-Brynaert, *Polymer* **39**(1998)835.
- [Hiro75] Hirokawa, *J. Elec. Spec. Rel. Phenom.* **6**(1975)333.
- [Hua90] W.S. Huang, M. Angelopoulos, J. R. White, J. M. Park, *Mol. Cryst. Liq. Cryst.* **227**(1990)189.
- [Hupe89] Hupe J, Kronenberg W (1989) Patent Application by Blasberg Oberflächentechnik, PCT No. PCT/EP89/00204.
- [Kling97] Klingenberg et al., *Surf. Sci.* **383**(1997)13.
- [Kron98] S. Krongelb, L.T. Romankiw, J. A. Tornello, *IBM J. Res. Dev.* **42**(1998)15.
- [Küp97] M. Küpper, J. W. Schultze, *Electrochim. Acta* **42**(1997)3033.
- [Kupf00] H. Kupfer, G.K. Wolf, *Nuc. Instr. Meth. Phys. Res. B* **166-167**(2000)722.
- [Kupf99] H.Kupfer, G. Hecht, R. Oswald, *Surf. Coat. Tech.* **112**(1999)379.
- [Land90] D. Landolt, in: N. Masuko, T. Osaka, Y. Ito, Kodansha (Eds.), *Electrochemical Technology: Innovation and new developments*, Gordon and Breach London, 1996, p215.
- [Laur00] L.Laurens, M. Bouali, F. Meducin, B. Sadras, *App. Sur. Sci.* **154-155**(2000) 211.
- [Laur98] P.Laurens, B. Sadras, F. Decobert, F. Arefi-Khonsari, J. Amouroux, *Int. J. Adhesion and adhesives* **18**(1998) 97.
- [Lehm02] V. Lehmann, *Electrochemistry of Silicon: Instrumentation, Science, Materials and Application*, Wiley-VCH, Weinheim, 2002.
- [LPW88] *Taschenbuch für Galvanotechnik*, Band 1.: Verfahrenstechnik, LPW-Chemie GmbH 1988.
- [Mai02] T.T. Mai, J.W.Schultze, G. Staikov, *Sol. Stat. Electrochem.*, in printing
- [Mai02] T.T. Mai, J.W.Schultze, G. Staikov, *Electrochim. Acta*, in printing
- [Mann93] D. Mann, in: *15. Ulmer Gespräch-Kunststoffmetallisierung und leitende Polymere*, Eugen G. Leuze Verlag, 1993.
- [Mat99] M. Matlosz, P.-H. Vallotton, A.C.West, D. Landolt, *J. Electrochem. Soc.* **146** (1999) 2886.
- [Mey93] H. Meyer, in: *15. Ulmer Gespräch-Kunststoffmetallisierung und leitende Polymere*, Eugen G. Leuze Verlag, 1993, p74.
- [Möb00a] A. Möbius, P. Pies, A. Königshofen, *Metalloberfläche* **54**(2000)3.
- [Möb00b] A. Mölbuis, *Journal für Oberflächetechnik* (2000)14.
- [Möb00c] A. Möbius *et.al* (2000), Patent Application by Enthone OMI, PCT No. PCT/US99/26066.



- [Nick68] G.Nickless, *Inorganic Sulphur Chemistry*, Elsevier, Amsterdam, 1968.
- [Okin90] Y. Okinaka, T. Osaka, in: *Advances in Electrochemical Science and Engineering (Vol. 3)* (Eds. C. Alkire, D.Kolb), Wiley-VCH, 1990, p55.
- [Ost93] R. Ostwald, in: *15. Ulmer Gespräch-Kunststoffmetallisierung und leitende Polymere*, Eugen G. Leuze Verlag, 1993, p89.
- [OSul90] E.O'Sullivan, in: *Advances in Electrochemical Science and Engineering (Volume 3)* (Eds. C. Alkire, D.Kolb), Wiley-VCH, 1990.
- [OSul98] O'Sullivan *et.al*, *IBM J. Res. Develop.* **42**(1998)127
- [Pase93] I.Paseka, *Electrochim. Acta* **38**(1993)2449.
- [Pase95] I.Paseka, *Electrochim. Acta* **40**(1995)1633.
- [Pase97] I. Paseka, J. Velicka, *Electrochim. Acta* **42**(1997)237.
- [Patn99] A. Patnaik, C.Li, *App. Sur. Sci.* **140**(1999) 197.
- [Petz76] G. Petzow, *Metallographisches Ätzen*, GebrüderBorntträger, Berlin-Stuttgart, 1976.
- [Pily97] S. Pilyte, G. Valiuliene, A. Zieliene, J. Vinkevicius, *J. Electroanal. Chem.* **436**(1997)127.
- [Poch97] K. Pochner, S. Beil, H. Horn, M. Blömer, *Surf. Coat. Tech.* **97**(1997)372.
- [Pour66] M.Pourbaix, in: *Atlas of electrochemical equilibria in aqueous solutions*, Pergamon,1966.
- [Rat95] Ratchev.B, Was. G , Booske., *J. Nuc. Instr. Meth. Phys. Res. B* **106**(1995)68.
- [Rue00] D.M. Rueck, *Nuc. Inst. Meth. Phys. Res. B* **166-167**(2000)602.
- [Sach90] E. Sacher, J.J. Pireaux, S. P. Kovalczyc, *Metallization of Polymers*, American Chemical Society, Wasington, 1990.
- [Sam96] C. Sambucetti, in: N. Masuko, T. Osaka, Y. Ito, Kodansha (Eds.), *Electrochemical Technology: Innovation and new developments*, Gordon and Beach London, 1996, p216.
- [Sasa00] K.Y. Sasaki, J. B. Talbot, *J. Electrochem. Soc.*, **147** (2000) 189.
- [Schat97] D. Schattka, S. Winkels, J.W. Schultze, *Metalloberfläche* **51**(1997)823.
- [Schö00] M.J. Schöning, A. Kurowski, M. Thust, P. Kordos, J. W. Schultze, H. Lüth, *Sens. Act. B* **64**(2000)59.
- [Schr95] D. Schroer, R.J. Nichols, H. Meyer, *Electrochim. Acta* **40**(1995)1487.
- [Schu01a] J.W.Schultze, A.Bressel, *Electrochim. Acta* **47**(2001)3.
- [Seid99] C. Seidel, H. Kopf, B. Gostmann, T. Vieth, ,H. Fuchs, K. Reih, *App. Sur. Sci.* **150**(1999)19.
- [Sher93] US 5,192,590 (SHERMAN) 09 March 1993.
- [Stai02] G. Staikov, in: J.W. Schultze, T. Osaka, M. Datta (Eds.) *Electrochemical Microsystem Technologies. In: New Trends in Electrochemical Technology Series*, Vol.2, Gordon and Breach, London, 2002, p156.
- [Syke69] A.G. Sykes, J.A. Weil, *Prog. Inorgan. Chem.* **13**(1969)1.
- [Taba00] I. Tabakovic, S. Riemer, V. Inturi, P.Jallen, A.Thayer, *J. Electrochem. Soc.* **147**(2000)219.
- [Tong95] H. M. Tong, *Mat. Chem. Phys.*, **40**(1995)147.

- [Urib93] F.A. Uribe, J. Valerio, S. Gottesfeld, *Synth. Met.* **55-57**(1993)3760.
- [Vaug97] D. J. Vaughan, U. Becker, K. Wright, *Int. J. Min. Proc.* **51**(1997)1.
- [Veer97] S. Veeramasuneni, J. Drelich, J.D.Miller, G. Yamauchi, *Prog. Org. Coat.* **31**(1997)265.
- [Vink98] J. Vinkevicius, I. Mozginskie, V. Jasulaitiene, *J. Electroanal. Chem.* **442**(1998)73.
- [Wagn78] C.D.Wagner, W.M. Riggs, L.E. Davis, J.F. Moulder, G.E. Muilenberg (Eds.): *Handbook of X-ray Photoelectron Spectroscopy*“, Perkin-Elmer Cooperation, Eden Prairie, Minnesota (1978).
- [Wash21] E.W. Washburn, *Phys. Rev.* **17**(1921)273.
- [Wei97] R. Weichenhain, D.A. Wesner, W. Pflöging, H. Horn, E.W.Kreutz, *Appl. Surf. Sci.* **109/110**(1997)264-269
- [Wolf93] G.D. Wolf, H.Giesecke, in: *15. Ulmer Gespräch-Kunststoffmetallisierung und leitende Polymere*, Eugen G. Leuze Verlag, 1993.
- [Wong98] K. K. H. Wong, S. Kaja, P. W. De Haven, *IBM J. Res. Dev.* **42**(1998).
- [Wu97] J. Wu, in: *“Introduction to percolation theory”*, <http://ist-socrates.berkeley.edu/~jqwu/paper1/>
- [Yan01] Y. Zhang, K.L.Tan, G.H.Yang, K.G. Neoh, *J. Electrochem. Soc.*, **148**(2001)C574.
- [Zech99] N. Zech, E.J. Podlaha, D. Landolt, *J. Electrochem. Soc.*, **146**(1999)2886.
- [Zha01] X.G. Zhang, *Electrochemistry of Silicon and Its Oxide*, Kluwer Academic, New York, 2001.